iScience

CellPress

Article

Dendron-Functionalized Surface: Efficient Strategy for Enhancing the Capture of Microvesicles

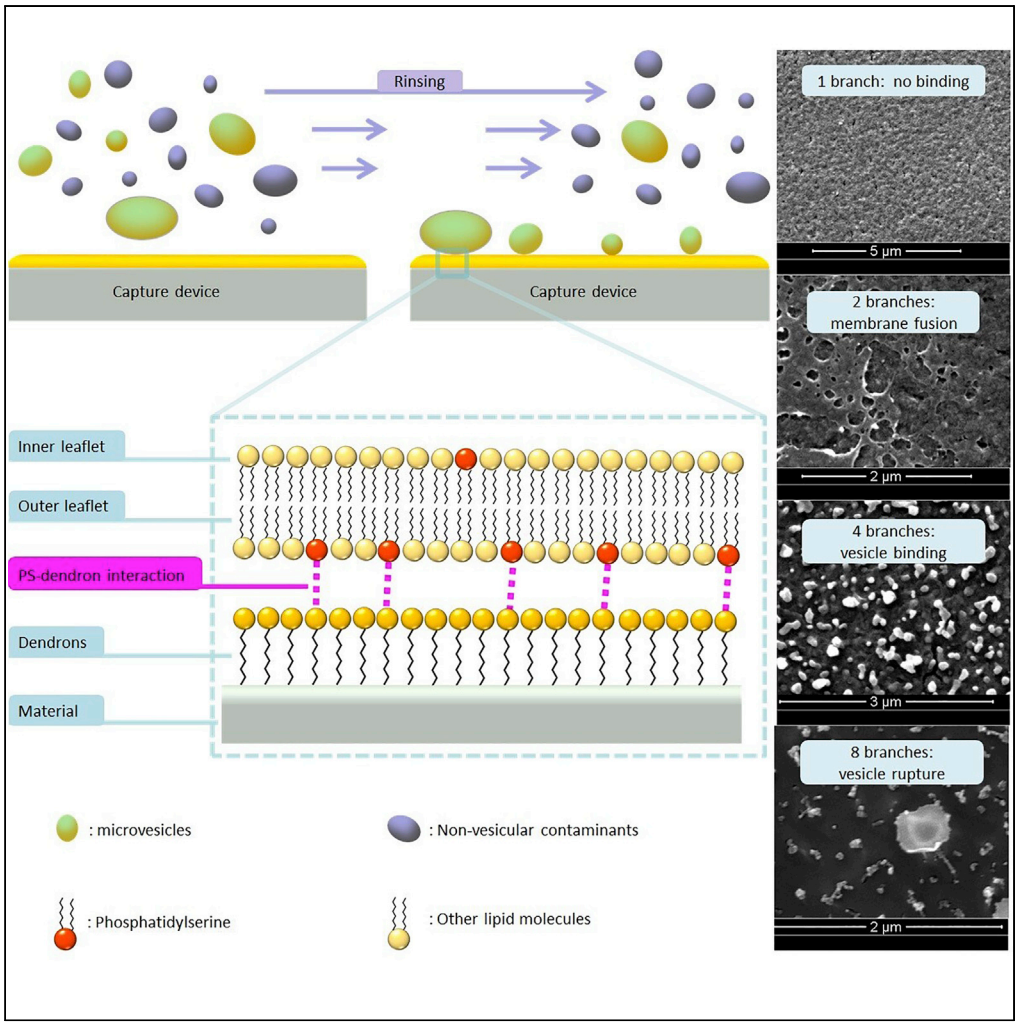

Jian-Qiao Jiang, Christel Chanseau, Isabel D. Alves, Sylvain Nlate, Marie-Christine Durrieu

s.nlate@iecb.u-bordeaux.fr (S.N.)
marie-christine.durrieu@inserm.fr (M.-C.D.)

HIGHLIGHTS

Phosphatidylserine-dendron interaction studies with NMR techniques

Lipid membrane binding enhancement using dendritic molecules

Dendron-grafted material for effective MV capture

Jiang et al., iScience *21*, 110–123
November 22, 2019
https://doi.org/10.1016/j.isci.2019.10.014

iScience

CellPress

Article

Dendron-Functionalized Surface: Efficient Strategy for Enhancing the Capture of Microvesicles

Jian-Qiao Jiang,[1,2,3] Christel Chanseau,[1,2,3] Isabel D. Alves,[1,2,3] Sylvain Nlate,[1,2,3,*] and Marie-Christine Durrieu[1,2,3,4,*]

SUMMARY

Microvesicles (MVs) are used by various types of cells in the human body for intercellular communication, making them biomarkers of great potential for the early and non-evasive diagnosis of a spectrum of diseases. An integrated analysis including morphological, quantitative, and compositional studies is most desirable for the clinical application of MV detection; however, such integration is limited by the currently available analysis techniques. In this context, exploiting the phosphatidylserine (PS) exposure of MVs, we synthesized a series of dendritic molecules with PS-binding sites at the periphery. PS-dendron binding was studied at the molecular level using NMR approaches, whereas PS-containing membrane-dendron interaction was investigated in an aqueous environment using plasmon waveguide resonance spectroscopy. As a proof of concept, polyethylene terephthalate surface was functionalized with the synthetic dendrons, forming devices that can capture MVs to facilitate their subsequent analyses.

INTRODUCTION

In the human body, microvesicles (MVs) like other kinds of extracellular vesicles play a pivotal role in both intercellular (adjacent or distant) communication and extracellular environment adaption (Henao Agudelo et al., 2017; Aupeix et al., 1997; Wang and Lu, 2017; Wyllie and Ramirez, 2017; Jeney, 2018; Paolicelli et al., 2019). The biogenesis of MVs is recognized as the budding of cytoplasmic membrane of eukaryotic cells upon activation (Tricarico, Clancy and D'Souza-Schorey, 2017). Widely adopted as carriers of biomolecules (proteins, mRNA, microRNA, lipids, etc.) from parent cells to even transkingdom recipients, they are omnipresent in all kinds of bodily fluids (Bruschi et al., 2019; Chavez et al., 2019; Clancy et al., 2015; Nievas et al., 2018; Owens and Mackman, 2011; Sampaio et al., 2017; Sun et al., 2018; Takahashi et al., 2017). In light of such knowledge, for novel diagnostic methods such as liquid biopsy, there are good reasons for MVs to become attractive subjects of study, namely, (1) MV release happens under cellular stress, preluding other symptoms of a same disease, therefore MVs of certain composition could act as an early biomarker (Jayachandran et al., 2008; La Marca and Fierabracci, 2017); (2) MV emission happens to a huge variety of cells from stem cells to parasites, making MV analysis useful for a spectrum of disease detection such as cancer, diabetes, viral infection, and cardio/cerebrovascular diseases (Aupeix et al., 1997; Owens and Mackman, 2011; Muralidharan-Chari, Clancy, Sedgwick and D'Souza-Schorey, 2010; Andrews et al., 2016; Bergen et al., 2018; Holliday et al., 2019; Meckes and Raab-Traub, 2011); and (3) MV membrane composition is dependent on the cytoplasmic membrane composition of its parent cell, making them easier to be traced to the origin even when samples are collected at a distance to the malfunctioning tissue, allowing non-evasive sampling while improving the accuracy of the diagnosis (Jayachandran et al., 2008; Andrews et al., 2016).

For the application of MV detection in disease diagnosis, the quantity, size distribution, and composition (lipid composition, proteins, RNAs, etc.) of the MVs in a certain sample are desired. Unfortunately, none of the currently available approaches are able to achieve both criteria: flow cytometry failed to detect 99%–99.9% of the vesicle population due to its optical limitations, whereas atomic force microscopy and electron microscopy cannot provide any compositional information (Obeid et al., 2017; Rautou and Mackman, 2013). Western blot and qPCR, on the other hand, are able to give information on protein and RNA composition, respectively; however, both methods fail to quantify the MVs within a sample (Henao Agudelo et al., 2017; Bruschi et al., 2019; Sun et al., 2018; Clancy et al., 2015; Svedman et al., 2018).

[1]Université de Bordeaux, Chimie et Biologie des Membranes et Nano-Objets (UMR5248 CBMN), Allée Geoffroy Saint Hilaire - Bât 14, Pessac 33600, France

[2]CNRS, CBMN UMR5248, Allée Geoffroy Saint Hilaire - Bât 14, Pessac 33600, France

[3]Bordeaux INP, CBMN UMR5248, Allée Geoffroy Saint Hilaire - Bât 14, Pessac 33600, France

[4]Lead Contact

*Correspondence: s.nlate@iecb.u-bordeaux.fr (S.N.), marie-christine.durrieu@inserm.fr (M.-C.D.)

https://doi.org/10.1016/j.isci.2019.10.014

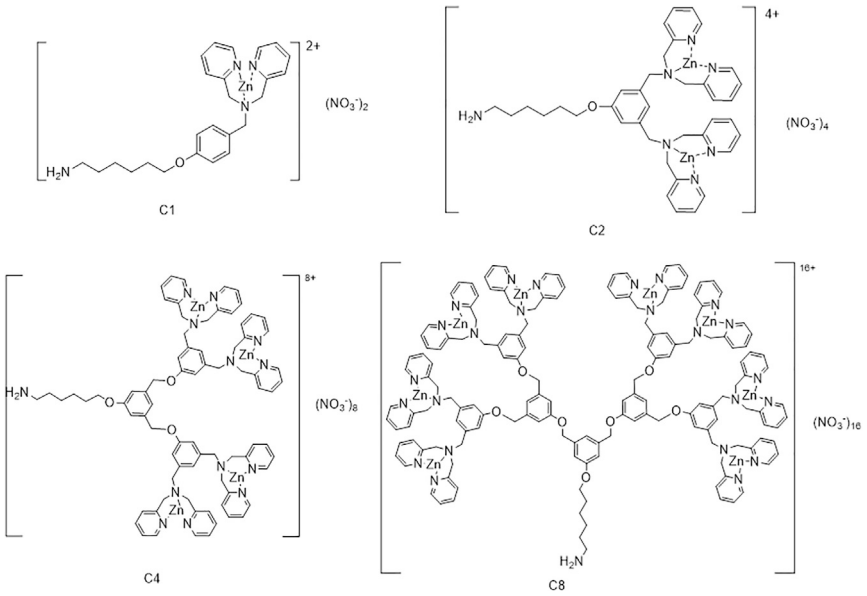

Scheme 1. DPA-Zn Molecules with Increased Dendricity

A proper characterization method for MVs is therefore a combination of the above-mentioned methods, where MVs in a sample are prepared in such a manner that electron microscopy, qPCR, and western blot can all be performed easily. For this purpose, we herein propose a device that allows MVs be captured to a device surface, allowing the future analysis.

Phosphatidylserine (PS) is the most abundant negatively charged phospholipid in human cellular membranes (Leventis and Grinstein, 2010). Despite being synthesized intracellularly, its distribution in healthy human cells is mostly limited to the plasma membrane, particularly the inner leaflet, by the function of flippases (Hankins et al., 2015; Segawa and Nagata, 2015). Its exposure to the extracellular leaflet is often considered as an early sign of programmed cell death, and its presence in MV outer membranes is also well documented (Owens and Mackman, 2011; Segawa and Nagata, 2015; Nagata et al., 2016; Iba and Ogura, 2018; van Engeland et al., 1998). MV capture devices using annexin V have been published since 1997 and have been improved over the years (Obeid et al., 2017; Gajos et al., 2017). However, this MV capture process depends on Ca^{2+} in the sample milieu by the concentration of millimoles (van Engeland et al., 1998). Such high concentration of Ca^{2+} would become problematic when MV capture is required before removal of cells within the sample: Ca^{2+} influx is a well-known stimulant for MV generation for a variety of cell types, causing the contamination of MV specimen captured onto the devices (Hugel et al., 2005; Taylor and Bebawy, 2019). An alternative approach for PS capture is the application of chemosensors, i.e., dipicolylamine-Zn^{2+} (DPA-Zn) complexes. First published as a sensor for phosphorylated peptides, DPA-Zn rapidly expanded into a family of chemosensors for the detection of negatively charged phospholipids (Ojida, Mito-oka, Inoue and Hamachi, 2002; Rice et al., 2016; Zwicker et al., 2019; Koulov et al., 2003). The synthetic chemosensors compared against annexin V have the obvious advantages of all chemosensors such as the ease of preparation in large quantity, relatively flexible transportation, and storage conditions. Most importantly, the binding of guest molecule to PS no longer requires the Ca^{2+}-rich environment. For applications in MV capture, DPA-Zn molecules should be able to covalently conjugate with a supporting material. A strong interaction between DPA-Zn and PS is, of course, expected for the molecule to bind to MVs.

Herein, we wish to report a series of four dendron-functionalized surfaces with increasing dendricity and their use for the capture of MVs. To build these nanomaterials, and to evaluate the dendritic effects on the capture of MVs, we have designed four complexes with one, two, four, and eight peripheral DPA-Zn units (Scheme 1). For this purpose, our synthetic strategy is based on the dendron core connected to an alkyl spacer with a primary amine for surface functionalization. Multivalent binding of peripheral dendrons to PS containing MVs can be achieved to maximize the binding strength. Besides, it is suggested that

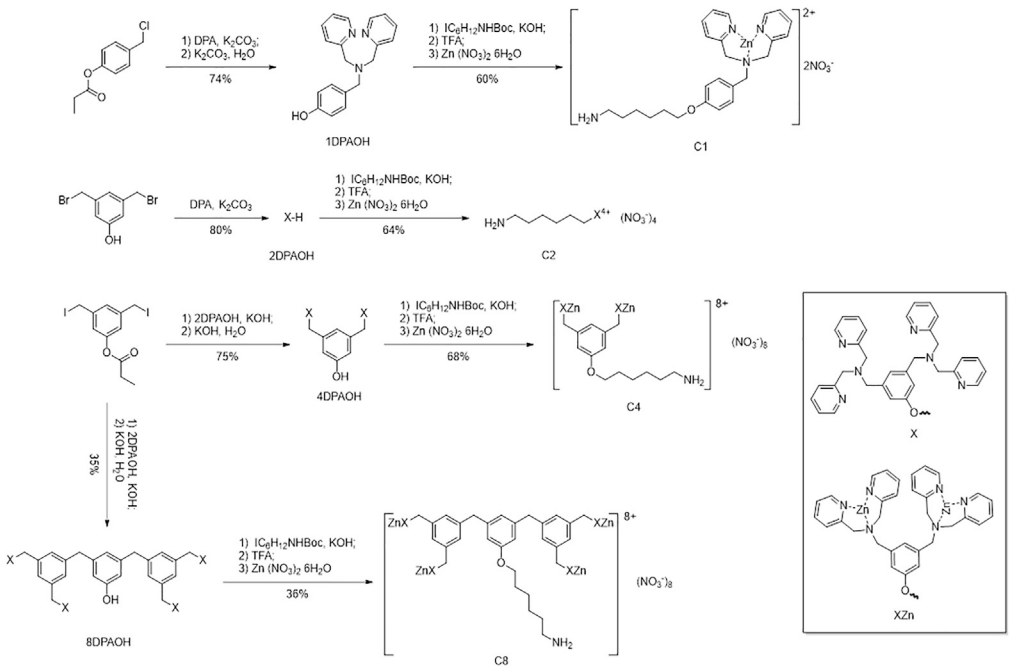

Scheme 2. Synthetic Routes of C1, C2, C4, and C8

For detailed synthesis protocols, please refer to "Transparent Methods in Supplemental Information, where corresponding NMR and mass spectra (Figures S4–S46) are also provided.

spatially close DPA-Zn units have synergetic effect during PS binding (Ojida et al., 2002; Koulov et al., 2003). Phenoxyl repeating units will provide a structure wherein DPA-Zn moieties can be kept closer to each other spatially, hopefully achieving such synergy.

RESULTS AND DISCUSSION

Dendron Synthesis

As illustrated in Scheme 2, 1DPAOH and 2DPAOH were synthesized by nucleophilic substitutions of dipicolylamine (DPA) with corresponding benzyl halide (chloride and bromide for 1DPAOH and 2DPAOH, respectively) alcohol. These reactions could proceed relatively easily in the presence of K_2CO_3. 4DPAOH and 8DPAOH, on the other hand, were synthesized using more strict reaction conditions: benzyl iodide was required for its higher reactivity during substitution reactions, whereas KOH was added to generate phenoxide before the addition of benzyl iodide. To facilitate higher yield in the synthesis of dendritic molecules, reactions were performed at low temperature (around −20°C), reducing the possible generation of side products. The convergent synthesis strategy facilitates the separation of starting material and the target compound, because the polarity of molecules increased significantly with the increase of the dendritic structure. This explained the high purity of complex 4. However, the convergent synthesis of **8DPAOH** from the phenol dendron **4DPAOH** led to modest yield, probably due to the great steric hindrance during the reaction and the high polarity of both compounds, which renders difficult the separation of compounds 4DPAOH and 8DPAOH by column chromatography. The steric hindrance can also be observed during the addition of the hexylamine spacers: for **1DPAOH** and **2DPAOH,** Boc-protected spacer can be easily attached with high yields and removed using trifluoroacetic acid also with high yields. In the case of **4DPAOH,** however, Boc protection cannot be removed. Thus, Teoc protection had to be used instead because its deprotection only required fluoride ion, a significantly smaller reagent, which can easily find its way into the desired reaction site. For **8DPAOH**, the attachment of a spacer is much more difficult because of the deeply buried phenol group within the dendritic structure, causing another significant drop in the final yield of C8 synthesis. The full characterization of all new compounds and the experimental procedures are given in Supplemental Information.

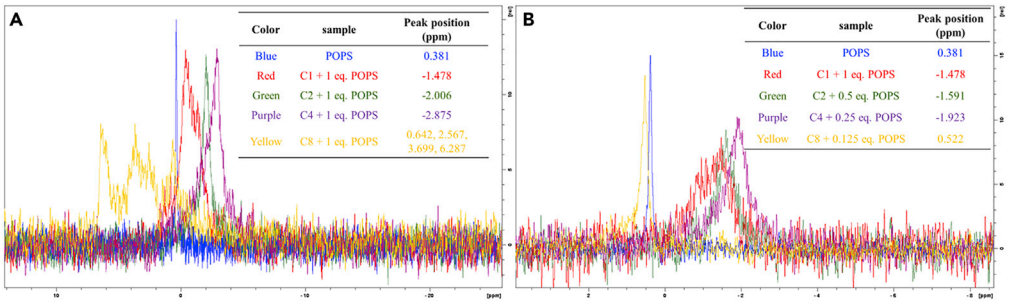

Figure 1. ^{31}P Spectra of Complex-POPS Mixture

(A) The mixture of complexes and POPS in 1:1 stoichiometry.

(B) The mixture of complexes and POPS with stoichiometry of 1 DPA-Zn unit to 1POPS.

Inset tables: mixture compositions.

NMR Investigation of DPA-Zn Complex-PS Interaction

After acquiring the DPA-Zn complexes of increased dendricity, the zinc complex-PS interactions were first studied in solution. Although proposed in many literatures that PS interacts with DPA-Zn through electrostatic affinity of phosphate anion and Zn^{2+} of the complexes, and published X-ray crystallography structures of DPA-Zn and phosphate complexes always show bonding between Zn^{2+} and phosphate, surprisingly there is no experimental proof for this assumption yet (Zwicker et al., 2019; Plaunt et al., 2014; Selmeczi et al., 2007; Ngo et al., 2012; O'Neil and Smith, 2006). To address this issue as well as to preliminarily evaluate the binding ability of the complexes to PS, we adopted NMR investigation so that the peak shapes and chemical shifts can be used as evaluation criteria (Selmeczi et al., 2007).

^{31}P NMR spectroscopy was used to examine the interaction between complexes and PS in solution, because the chemical environment of phosphorous atom in 1-palmitoyl-2-oleoyl-sn-glycero-3-phospho-L-serine (POPS) will be the most affected should the complexes bind to the phosphate of POPS. Considering the similarity of the binding events (DPA-Zn to POPS), the changes in chemical shift can also roughly represent the strength of such interactions (it is assumed that the observed chemical shift is the mole fraction-weighted average of the shifts of the free and DPA-Zn-bound POPS) (Fielding, 2000). As shown in Figure 1A, when 1 equiv. of different complexes is added into 1 equiv. of POPS in solution, the changes of the ^{31}P NMR chemical shifts varies significantly. C1, C2, and C4 make the signal shift to high field, whereas C8 makes the signal go to low field. From C1 to C4, with the increase of molecular dendricity, the change in chemical shift also increases, indicating a stronger binding ability with more binding sites. This can be easily interpreted as the result of the increase in DPA-Zn concentration in solution. For instance, even though the molarities of the complexes are the same, C4 brings 4 times the amount of DPA-Zn into the solution compared with C1, pushing the reaction equilibrium further to the formation of (DPA-Zn)-POPS complex. However, the difference between different DPA-Zn molecules is not only limited to the increase of DPA-Zn moiety numbers. With the increase in DPA-Zn numbers, one obvious difference is the dendritic scaffolds to which the DPA-Zns are attached. To investigate the effect of the molecular scaffolds, another experiment was performed where the molar ratio of DPA-Zn units to POPS was fixed at 1:1. The ^{31}P NMR spectra of the corresponding mixtures are summarized in Figure 1B. Again a similar trend in chemical shift can be observed: the changes in chemical shift increase with the increase in the number of DPA-Zn units within complexes, in the order of C1, C2, and C4. The differences in chemical shifts between C1 and C2 complexes bearing a single phenyl ring as a molecular scaffold are less significant, whereas C4, possessing a dendritic structure, shows more significant changes in the ^{31}P NMR chemical shift of POPS. Regardless of the molar ratios, C8 behaves quite differently than the other molecules. It is most likely due to the so-called negative dendritic effect, in which the dendritic structure acts as a shield of steric hindrance, reducing the binding ability of DPA-Zn. In all cases, the changes are in good agreement with the assumption that DPA-Zn complexes bind to the phosphate groups on POPS, whereas C4 has the strongest ability to bind to POPS.

Although the ^{31}P NMR can provide preliminary information about DPA-Zn complex-POPS interactions, such as the interaction site on POPS and the interaction strength, the involvement of other atoms during complex-POPS binding is yet to be determined. For this purpose, ^{1}H NMR is another useful technique. With the involvement of heteroatoms, nearby protons will experience change in the chemical environment,

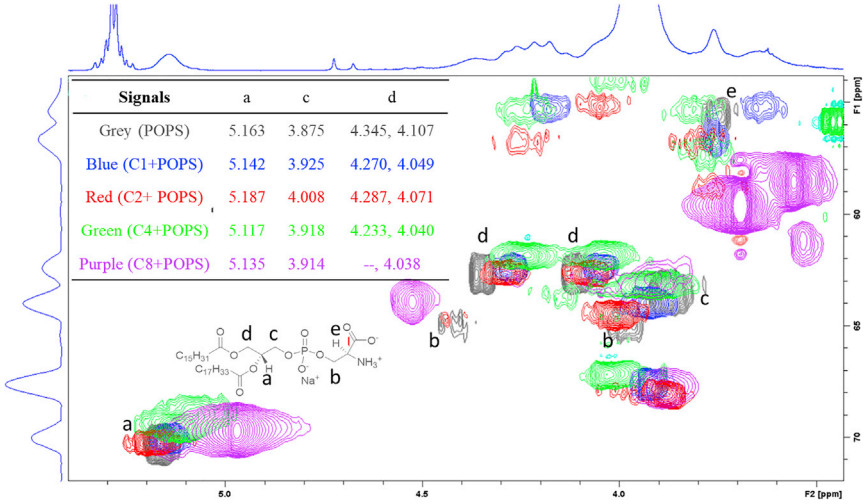

Figure 2. HSQC Spectrum of POPS Head Group

Pure POPS, gray; C1+POPS, blue; C2+POPS, red; C4+POPS, green; and C4+POPS, purple. Inset table: the chemical shifts of the glycerol proton signals.

causing the shift of ^{1}H NMR signals. However, the ^{1}H NMR of synthesized complexes has too many overlapping regions with POPS, causing the difficulty of spectra interpretation. Heteronuclear single quantum correlation (HSQC), on the other hand, is able to distinguish different proton signals of similar chemical shifts according to the carbon backbone. It was therefore used to investigate the interaction from the perspectives of both POPS and complexes.

To investigate DPA-Zn-binding site on POPS, 1 equiv. of different complexes was added into POPS solution and the HSQC spectra of corresponding mixtures were recorded. Figure 2 shows the part of POPS HSQC NMR spectrum interpretation related to the head group. Looking at the glycerol moiety of the molecule (protons at positions a, c, and d), there is an obvious trend that the change in chemical shifts as well as the broadenings also increase with dendricity (in the cases of C1, C2, and C4) for the proton signals. For C8-POPS mixture, there are also shifts in glycerol signals; however, these shifts are less prominent compared with C4, again highlighting the negative dendritic effect. Unsurprisingly, this is in good agreement with ^{31}P NMR spectra. Both ^{31}P and HSQC indicate that the strongest (DPA-Zn)-POPS interaction is achieved with C4. Unfortunately, signals of the serine moiety (signals b and e) cannot be observed clearly after the complexation; therefore, involvement of the serine moiety is still unclear. Considering the change in ^{31}P signal and the change in glycerol signals, the involvement of the phosphate group during complexation can now be confirmed.

To understand the difference in DPA-Zn-POPS interaction among the synthesized molecules, study of the complexes before and after POPS binding is also performed. As only synthesized complexes contain aromatic groups, ^{1}H NMR can be used directly for investigating the effect of POPS binding to the complexes without the interference of POPS signals. To compare the effect of PS binding on individual DPA-Zn moieties, 1, 0.5, 0.25, and 0.125 equiv. of C1, C2, C4, and C8 were added to POPS solution, respectively, to acquire the corresponding ^{1}H NMR spectra. For C1, C2, and C4, the pyridine proton signals (Figure 3, peaks a, b, c, and d in each spectrum) become broader and the spectrum details are also lost after the binding to POPS. In the three complexes, the change in chemical shifts are most prominent for the α protons, which locate closest to the Zn^{2+} ions. This result confirms that the synthesized molecules interact with POPS through the complexed Zn^{2+} ions. Most interestingly, the aromatic proton signals of benzyl ether backbone in each molecule (Figure 3, peaks e, f, and g) also change significantly after binding to POPS. Considering their electron neutrality, the benzyl ether backbones are unlikely to interact directly with POPS. The chemical shift changes could come from either the change of the electron environment of the backbone after DPA-Zn of each molecule binds to POPS or the conformational change of the entire molecule after POPS binding. Although the mechanism is not clear, the indirect involvement of the benzyl ether backbones in POPS binding is confirmed. The differences of the ^{31}P NMR spectra in Figure 1B for C1, C2, and C4 could be explained by the involvement of benzyl ether backbones in POPS binding, whereas C4

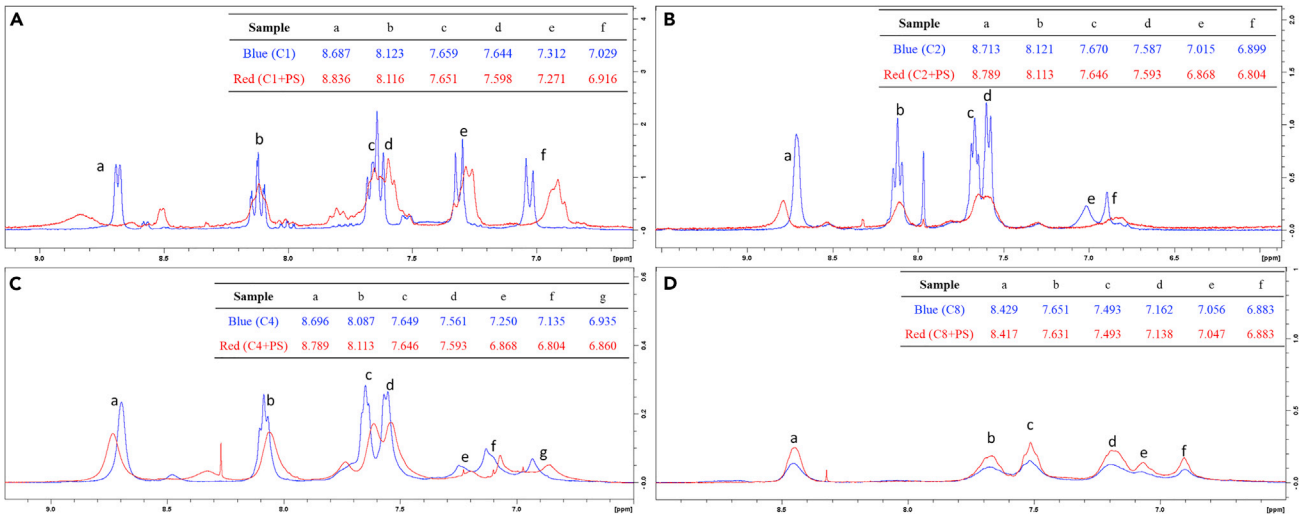

Figure 3. 1H Spectra of Complex Aromatic Groups

(A–D) C1 (A), C2 (B), C4 (C), and C8 (D). Inset table: the chemical shifts of proton signals.

with the dendritic structure has the strongest positive influence on the change of POPS ^{31}P chemical shift. Unlike the positive dendritic effect shown with C4, C8 with even higher dendricity showed little spectral change after the addition of POPS, again indicating a negative dendritic effect during POPS binding.

Plasmon Waveguide Resonance Study of DPA-Zn Complex-Model Membrane Interaction

Although solution NMR provides information on the molecular interactions between POPS and zinc complexes, PS in biological systems is not solubilized and can only be found on lipid membranes. The goal of the complex design is therefore the improved interaction strength of synthesized molecules to PS-containing biological membranes. To evaluate the interaction strength between POPS-containing membranes and synthesized DPA-Zn complexes, a homemade plasmon waveguide resonance (PWR) spectrometer was adopted. The detailed setup of PWR and lipid bilayer constitution used herein is described elsewhere (Calmet et al., 2016; Reimhult et al., 2003). A PWR spectrometer has a setup quite similar to that of an Surface plasmon resonance (SPR) spectrometer with one important difference: the plasmon-generating metallic thin film (~50 nm silver) is coated with another dielectric layer (~460 nm silica) as waveguide (Salamon et al., 1997a, 1997b). The metallic layer itself is only able to generate plasmon resonance upon the excitation of linearly polarized light that has oscillation direction perpendicular to the metallic surface (p-polarized light), whereas the waveguide layer can generate waveguide resonance with light of both perpendicular and parallel (s-polarized light) polarizations (Salamon et al., 1997a; Salamon and Tollin, 2004). Once adhered to the silica surface, the optical properties of lipid membrane can be probed at both perpendicular and parallel directions using p- and s-polarized light, respectively. When DPA-Zn complex is interacting with such lipid membrane, the changes in s- and p-polarization signals are able to yield information on the change of membrane mass as well as anisotropy (Salamon and Tollin, 2004; Alves and Lecomte, 2019). Using a titration experiment, the peak positions of s- and p-polarized light can be fitted to acquire the K_d values of such interactions (Harte et al., 2014). After the formation of POPC(1-palmitoyl-2-oleoyl-sn-glycero-3-phosphocholine):POPS = 5:1 (w/w) bilayer (PSPC membrane) on the prism surface, a titration experiment is performed for each complex. Briefly, each complex was dissolved in HEPES buffer and then titrated into the Teflon sample chamber. As equilibrium was reached in each addition, the complex concentration, the spectral shifts of s-polarized light (parallel to the membrane surface), and the spectral shifts of p-polarized light (perpendicular to the membrane surface) were recorded. The titration stopped when addition of complex solution did not induce further change in spectral positions. The complex concentration was then plotted against the resonance angle, and the plot was fitted using GraphPad Prism 5 (Figure 4). The acquired K_d values were recorded in Table 1.

In the PWR titration experiment, binding events can be monitored by following the changes in both p- and s-spectra for each incremental addition of the complex. As explained by Salamon and Tollin, the resonance angle change in either polarization linearly correlates with the mass density (mass per unit area) changes on

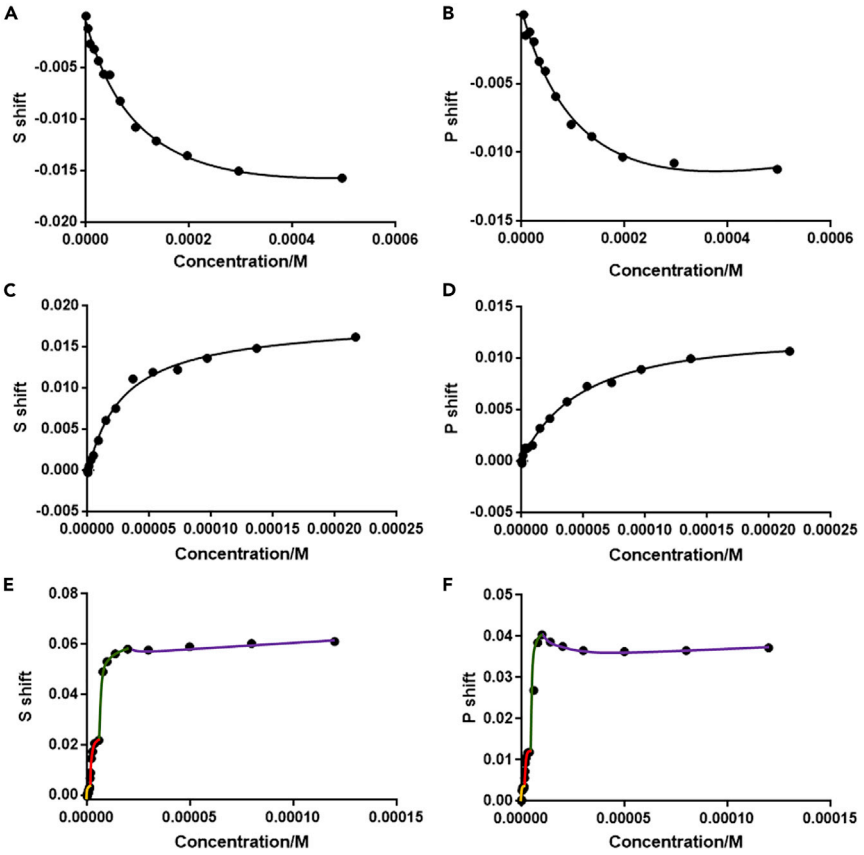

Figure 4. Fittings of Complex-PSPC Membrane Titrations

(A–F) (A and B) Fitting of C1-PSPC membrane titration in s- and p-polarizations, respectively; (C and D) fitting of C2-PSPC membrane titration in s- and p-polarizations, respectively; (E and F) fitting of C4-PSPC membrane titration in s- and p-polarizations, respectively.

the adsorbed lipid membrane (Salamon and Tollin, 2004). Two different scenarios can generally occur: (1) complex binding to the membrane leads to a hyperbolic increase in the resonance shift upon complex addition and (2) complex binding results in a shift decrease. The first scenario is the most common for molecules that bind and accumulate in the membrane surface without much change in the membrane organization. Therefore, increasing accumulation of the molecule at the membrane level leads to a hyperbolic response with saturation being reached. The data can be fitted to obtain a binding affinity. The second scenario can also be observed and reflects an impact of the interacting molecule on the lipid membrane organization. Indeed, such decrease in the resonance shifts can only be explained by mass removal from the system as a result of a "detergent"-type effect of the molecule on the membrane. A binding affinity can also be obtained in this case. It is to be noted that this is an apparent binding affinity that reflects both the binding of the molecule investigated and the accompanying lipid reorganization. The complexes show very different binding behaviors between each other. The resonance angles of both p- and s-polarized lights experienced continuous decreases upon the addition of C1, and the decreases stabilized at about 11 mdeg and 15 mdeg, respectively, for p- and s-polarizations. The final equilibrium was only reached when the concentration of C1 in the chamber reached submillimolar level, and the interaction K_ds determined by the fitting of the titration curves were at 10^{-4} M for both polarizations. When C2 was titrated to a membrane of same constitution until equilibrium, increasing spectral shifts of same scale happened for both polarizations. The K_d values were determined to be around 10^{-5} M, indicating a stronger complex-membrane interaction. In the case of C4, the titration curves indicated a four-stage reaction with the increase of complex concentration. The first three stages showed consecutive increases, with two K_d values as low as 10^{-7} M and the third at 10^{-6} M. The last stage showed decreasing resonance angles of both polarities with K_d values also at the 10^{-6} M level. The p- and s-polarized resonances stabilized at 60 and 37 mdeg, respectively, a shift more significant than either C1 or C2.

Complex		C1	C2	C4
K_d (M)	S	$1.25\times10^{-4}\pm3.163\times10^{-5}$	$2.092\times10^{-5}\pm9.509\times10^{-6}$	$1.771\times10^{-7}\pm9.617\times10^{-8}$
				$8.622\times10^{-7}\pm1.496\times10^{-7}$
				$9.346\times10^{-6}\pm2.565\times10^{-6}$
				$1.217\times10^{-6}\pm3.904\times10^{-7}$
	P	$1.498\times10^{-4}\pm5.054\times10^{-5}$	$7.232\times10^{-6}\pm2.178\times10^{-6}$	$1.42\times10^{-7}\pm2.811\times10^{-8}$
				$2.282\times10^{-7}\pm2.811\times10^{-8}$
				$3.489\times10^{-6}\pm1.849\times10^{-7}$
				$6.056\times10^{-6}\pm1.208\times10^{-6}$

Table 1. Complex-Membrane Interaction Dissociation Constants (K_ds) Acquired Using PWR
s, K_d values acquired using s-polarized light; p, K_d values acquired using p-polarized light.

Fabrication and Characterization of the MV Capture Devices

The MV capture devices were then prepared by functionalizing polyethylene terephthalate (PET) sheets using the synthesized DPA-Zn complexes. The purchased PET sheets were chemically treated using similar procedures reported previously with minor adaptions as shown in Figure 5 (Chollet et al., 2007; Chollet et al., 2009). Briefly, the PET sheets were hydrolyzed and then oxidized to produce abundant carboxyl groups onto the surfaces. The carboxyl groups were activated using EDC (N-(3-Dimethylaminopropyl)-N′-ethylcarbodiimide hydrochloride)/NHS (N-hydroxysuccinimide) thereafter to assist the amide bond formation so that the complexes with amine-ending spacers can be attached to the PET surfaces covalently. For each step of the surface functionalization, the carboxyl group surface density was monitored with toluidine blue O (TBO) test, whereas the atomic percentage of the material surface was followed by X-ray photoelectron spectroscopy (XPS).

As shown in Figure 6, the oxidized surface has the highest carboxyl group density. After the activation step, there is a drop of 43.06 pmol/mm^2 in COOH density, resulting from the substitution of hydrogen in COOH by NHS. A further drop in the COOH density can be observed after the grafting of the complexes onto the surface. This drop can result from two events: first, there is a reaction of amine and COOH in the presence of complexes, further eliminating the carboxyl groups on PET surface; second, when grafted on to PET surface, positively charged complexes repel the TBO^+ ions, preventing them from adsorbing onto PET.

The peak areas after fittings of the high-resolution XPS spectra were summarized in Table 2. The XPS results well correspond to each treatment of PET surface: After hydrolysis and oxidation steps, the ester bonds were hydrolyzed and then oxidized into carboxyl groups; therefore the highest value of COO signal among all the samples is observed. In the activation step, NHS molecules substituted the hydrogen of carboxyl groups. In the process, the number of surface carboxyl groups remains the same, whereas the NHS brings nitrogen onto the surface, leading to significant increases in the N1s and N-C=O signals without change in the –COO signal intensity. After the functionalization with complexes, multiple changes in the XPS spectra can be observed. First, the emergence of Zn indicates the successful attachment of complexes onto material surface. Second, the significant increase in (C1s N-C=O)/(C1s COO) and (N1s 399.9)/(O1s O=C) can be interpreted as the successful replacement of NHS by complexes, further confirming the covalent attachment of the complexes to PET surface. Third, as shown in Table 3, the molecular percentages (MPs) of the complexes (which is calculated by dividing the atomic percentage of an atom by the number of the same atom within a single molecule) calculated according to Zn2p3 and N1s all indicate an increasing difficulty for larger molecules attaching to the PET surface. The MP calculated with N1s is always higher than that calculated with Zn2p3, which could come from two facts: one is that there is NHS residue left on the surface because of incomplete substitution by the complexes, and the other is that during the intensive washing process, water behaved as a complexing agent and washed away the Zn^{2+} ion from the complex, whereas the ligands being covalently attached and insoluble in water, remained on the PET surface. This effect can become more prominent with the increase of dendricity, as shown in MP_{Zn}/MP_N in Table 3. Zn^{2+} cations are forced closer to each other in space with the increase of dendricity, experiencing more repelling force from each other, making them easier to come off.

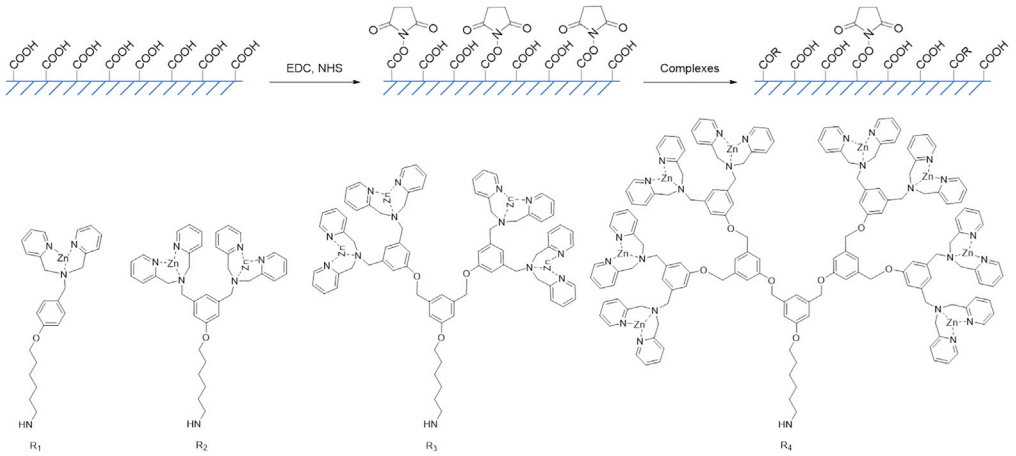

Figure 5. Surface Functionalization of PET Sheets Using Synthesized Complexes

Unfortunately, the exact molecular densities of all the complexes grafted to PET surface are yet to be determined. To the best of our knowledge, there is no technique available for such measurement. We tried to come up with an approximate value using the combination of the TBO measurement as a qualitative approach and the XPS as a semi-quantitative approach. TBO test indicated the carboxyl group densities. For the activation step, it was able to quantify the NHS groups fixed onto PET surface through the decrease of carboxyl group density; however, it failed to quantify the substitution of NHS by the complexes in the next substitution step. The further decreases in carboxyl group densities were suggestive for the substitution reaction, but they no longer serve as quantitative measurement for the reaction. The MP of a grafted complex calculated from the XPS results is quantitative; however, as it measures the total amount of atoms with a penetration about 10 nm into the bulk material, such percentage is still unable to transfer directly into molecular density at the surface of the material. Despite the above-mentioned disadvantages, TBO was able to suggest that all the synthesized complexes exhibit similar degree of carboxyl group "blocking" ability, whereas the XPS MPs of all complexes grafted onto PET surface suggest that different complexes bind to PET surface with the same order of magnitude.

For impurities appearing in the XPS spectra, Si most likely comes from the glass containers in which we processed all the PET sheets; S is from the manufacturing of the material as its concentration is relatively stable throughout the grafting procedures; last, Cl in oxidized and activated surface comes from the hydrochloric acid used in the surface washing of PET.

The Performances of the MV Capture Devices

The crucial parameters for vesicles being adsorbed on material surface in solution are the chemical composition of the substrate, temperature, and the osmotic pressure difference between the inside and the outside of the vesicles (Granqvist et al., 2014; Isono et al., 2007; Reimhult et al., 2003). In our case, to compare the complex-functionalized surfaces for their MV capture abilities, the most important parameter is the surface chemical environment. As the surface densities of complexes fixed onto PET are of the same magnitude for all four complexes, the MV capture abilities of functionalized surfaces can therefore be compared using the above-mentioned PET sheets. Cryo-scanning electron microscopy (SEM) and fluorescence (FL) micrograph of each surface after incubation with mesenchymal stem cell-generated MVs were used to visualize the comparison (for the FL imaging of MVs, CellMask Deep Red was used to stain the MVs beforehand).

Figures 7A and 7B show how the MVs responded to the C1-grafted surface. In the FL micrograph, only a small amount of donut-shaped red fluorescent spots can be observed. These structures were of sizes around 1 μm, much larger than the diameter of MVs. Considering the size distribution of the MVs acquired by nanoparticle tracking analysis (Figure S2), such phenomenon can only result from the aggregation of MVs. On the cryo-SEM image, the PET surface was blank and of a smooth morphology. No vesicle structure can be observed. MV capture using C2 functionalized PET is shown in Figures 7C and 7D. The whole material surface was covered with membrane structures, although inhomogeneity was observed throughout the surface. In the FL micrograph, although large areas of the surface were covered with fluorescent membranes, there were also bright dots

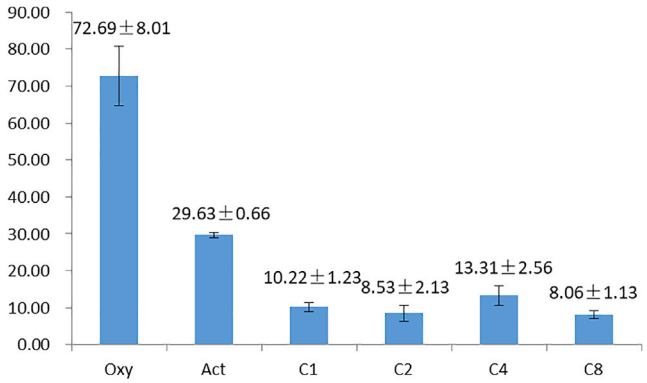

Figure 6. Carboxyl Group Density on Treated PET Surfaces

Oxy., oxidized PET; Act., NHS-activated PET; C1, C1 functionalized PET; C2, C2 functionalized PET; C4, C4 functionalized PET; C8, C8functionalized PET. Unit, pmol/mm2. See also Figure S1 and Table S1.

of MV size in the less-fluorescent regions. Very bright membrane aggregations with size over 1 μm and of irregular shapes can also be observed. Observation using cryo-SEM also reveals that the majority of the PET surface was covered by coalesced membrane structures, whereas at the boundaries of such aggregations, holes in the membrane and a small amount of vesicles attached to the PET surface can be observed as well. As shown in Figures 7E and 7F, both FL micrograph and cryo-SEM show that the MVs uniformly cover the whole surface functionalized with C4. MVs were found individually attached to the material surface. There are indeed some aggregations of MVs; however, such aggregation does not cause the fusion of MVs, leaving intact vesicles or vesicle aggregations captured onto the PET surface. FL micrograph and cryo-SEM in Figures 7G and 7H both show that particles uniformly cover the whole surface functionalized with C8. On the zoomed cryo-SEM image (Figure 7H), the particles were found to be of the same size as MVs; however, these structures resemble rough membrane flakes rather than smooth vesicles.

Micrographs indicate that the PET surfaces functionalized with C1 have very limited ability to capture MVs. This result correlates well with the PWR and NMR experiment results indicating that C1 has less ability to bind to PS. In comparison, C2, C4, and C8 functionalized surfaces were able to capture MVs due to the higher PS-binding abilities, although MVs behave differently when in contact with the three surfaces. When captured by C2 functionalized surface, vesicles are prone to rupture and then fuse with each other into membranes. Because of the destructed morphology of the MVs, their contents were suspected to be lost during the capture process, making C2 surfaces less favorable for the future applications for the examination of the vesicle contents. A similar conclusion can be drawn for C8 functionalized surface as it also caused the rupture of MVs. So far, C4 functionalized surface seems to be the best candidate for MV capture because vesicle morphology and their contents are well preserved. A possible explanation for such differences can be attributed to the dendritic backbones of the three molecules: the morphology of the membrane on C2 functionalized surface is highly reminiscent of the so-called supported lipid bilayers, where the vesicles (synthetic or naturally existing in biological systems) adhere to a hydrophilic substrate (such as silicon, glass, or silica) and form a bilayer via vesicle fusion (Granqvist et al., 2014; Isono et al., 2007). Such fusion is considered to be a process related to the chemical properties and most importantly the hydrophilicity of the surface in contact (van Weerd et al., 2015). C2 being the simplest of the three, its DPA-Zn moiety has the largest exposure to the aqueous environment with the highest density on PET surface yet with limited molecular flexibility. After C2 functionalization of PET, C2-PS interaction invites the vesicle adhesion to the PET surface, whereas the hydrophilic nature of C2 and the stiffness of PET substrate induce the vesicle to rupture, lie flat onto the surface, and fuse with each other into a larger membrane. Compared with C2, C4 is a relatively flexible molecule: as shown in Figure 3C, when binding to PS, the aromatic signals of the benzyl ether backbone also experience significant chemical shift, indicating the conformational change of C4 when binding to PS. Besides, C4 is a less hydrophilic molecule than C2, thus vesicle rupture is less likely to happen on the C4 functionalized surface. High-generation cationic dendrimers such as poly(amidoamine) (PAMAM) are known to cause membrane destruction. Mecke et al. found that PAMAM of generation 3 (G3) does not induce 1,2-dimyristoyl-sn-glycero-3-phosphocholine (DMPC) membrane destruction, whereas G5 and G7 PAMAMs are able to destroy lipid bilayer by removing lipid from membrane (Mecke et al., 2004; Mecke et al., 2005). Through computer simulation, Wang et al. discovered

Name	Oxy.	Act.	C1	C2	C4	C8
Si2p	0.33	0.38	0.53	0.39	0.49	0.63
S2p	0.33	0.33	0.27	0.23	0.23	0.29
Cl2p	0.15	0.11	0	0	0	0
C-C	32.20	26.62	34.18	28.02	31.97	28.25
C-CO	12.36	14.64	15.46	18.06	15.08	23.28
C-O	12.39	14.44	13.73	13.55	14.15	13.69
N-C=O	0.24	1.55	2.29	2.19	1.38	2.85
COO	12.09	11.65	7.33	9.40	8.38	5.32
291.6	1.77	1.34	0.80	0.96	1.31	1.02
N1s 398.0	0	0.27	0.13	0.09	0.23	0.01
N1s 399.9	0	1.77	3.05	2.85	3.42	5.30
N1s 401.9	0	1.05	0.28	0.29	0.28	0.40
O1s 530.7	0	0	1.32	0.33	1.22	0.75
O1s O=C	13.41	14.02	11.63	11.81	11.32	10.37
O1s O-C	14.72	11.84	8.49	11.32	10.06	7.56
Zn2p3	0	0	0.51	0.50	0.50	0.27

Table 2. XPS-Determined Atomic Percentages of PET Surfaces

Oxy., oxidized PET; Act., NHS-activated PET; C1, C1 functionalized PET; C2, C2 functionalized PET; C4, C4 functionalized PET; C8, C8 functionalized PET.

that PAMAMs of lower generations have more flexible structures (Wang et al., 2012). When in contact with DMPC membranes, the smaller PAMAMs are able to adjust their conformation and cause little disruption of DMPC bilayer. In contrast, the higher-generation dendrimers' conformations are limited by their inter-branch steric hindrance; thus at the dendrimer-lipid bilayer interface, DMPC membranes are forced to adopt the curvature of individual dendrimer molecules, causing possible membrane destruction. Similarly among our DPA-Zn complexes, C8 is the dendron of highest generation and thus has the highest conformation rigidity. When in contact with C8 functionalized surface, MVs are prone to destruction.

In conclusion, we have synthesized a series of multivalent DPA-Zn complexes with increasing dendricity. In ^{31}P NMR studies of complex-POPS interactions, dendritic C4 showed the strongest POPS binding ability. This result is in good agreement with the fittings of PWR titrations where the complex-membrane (POPS containing) interaction K_d values were determined. C1 being the complex with only one DPA-Zn unit has K_d values of 10^{-4} M; C2 of similar molecular scaffold but with two DPA-Zn units showed K_d values of 10^{-5} M. C4 on the other hand, with four DPA-Zn units attached to a dendritic scaffold, showed a four-stage binding process in the titration experiment, with K_d values as low as 10^{-7} M. Such improvement in binding strength is beyond the simple multivalent binding effect. To understand the exponential increase of complex-membrane interaction with the increase of

Surfaces	C1	C2	C4	C8
MP_{Zn}	0.51	0.25	0.13	0.034
MP_N	0.92	0.47	0.32	0.216
MP_{Zn}/MP_N	0.55	0.53	0.40	0.16

Table 3. XPS-Determined Molecular Percentages

MP = AP/n, where MP is molecular percentage, AP is atomic percentage, and n is the theoretical number of the corresponding atom per molecule.

C1, C1 functionalized PET; C2, C2 functionalized PET; C4, C4 functionalized PET; C8, C8 functionalized PET.

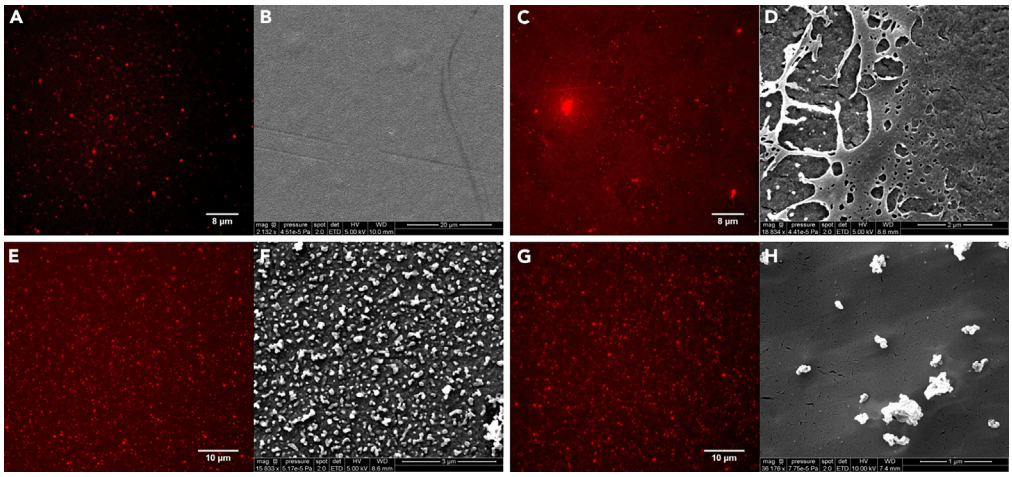

Figure 7. Micrographs of Functionalized Surfaces after 15 min of MV Incubation

(A) Fluorescence micrograph of C1 functionalized surface incubated with CellMask Deep Red-stained microvesicles; scale bar, 8 μm.

(B) Cryo-SEM image of C1 functionalized surface incubated with microvesicles; scale bar, 20 μm.

(C) Fluorescence micrograph of C2 functionalized surface incubated with CellMask Deep Red-stained microvesicles; scale bar, 8 μm.

(D) Cryo-SEM image of C2 functionalized surface incubated with microvesicles; scale bar, 2 μm.

(E) Fluorescence micrograph of C4 functionalized surface incubated with CellMask Deep Red-stained microvesicles; scale bar, 10 μm.

(F) Cryo-SEM image of C4 functionalized surface incubated with microvesicles; scale bar, 3 μm.

(G) Fluorescence micrograph of C8 functionalized surface incubated with CellMask Deep Red-stained microvesicles; scale bar, 10 μm.

(H) Cryo-SEM image of C8 functionalized surface incubated with microvesicles; scale bar, 1 μm

See also Figure S2 and S3.

DPA-Zn units, we performed HSQC and ^{1}H NMR experiments to investigate the interaction at the molecular level. The HSQC experiments indicated that the complexes bind to the phosphate group of POPS, whereas the ^{1}H NMR spectra reveal the DPA-Zn involvement in the POPS-binding process as hypothesized in many literatures. The ^{1}H chemical shifts of the benzyl ether scaffold where DPA-Zn units are attached also showed significant changes after POPS binding, indicating the scaffolds are also involved in the binding processes. In the case of C2, the two DPA-Zn units showed synergetic binding to the POPS molecules, and C4 with a dendritic structure further enhanced such effect by conformational change upon PS binding. Unfortunately, the enhancement effect cannot be applied to molecules of higher dendricity of the same repeating units. C8 of eight DPA-Zn units has been proved to be difficult to synthesize, while its PS-binding performance is no better than any smaller DPA-Zn complex according to ^{31}P NMR. All the synthesized DPA-Zn complexes were able to be attached to the model PET surface covalently with an amino hexane spacer to form a device for MV capture, while the binding molecular densities on PET surfaces were semi-quantitatively determined with TBO and XPS experiments. The MPs were found to be at the same order of magnitude for all complexes, although a decreasing trend can be found with the increase in dendricity. The MV capture performance for each device was then evaluated with FL microscopy and cryo-SEM. Dendron C4 functionalized surface appears to be the best candidate for MV capture, as it not only successfully captured MVs onto the surface but also has maintained the morphology of the MVs. Such surface could be useful for future diagnostic applications because the device can capture biochemical information of both MV membrane and the inner content for analysis purpose. This interfacial engineering technique should be substrate independent, a high added value being that the same reactive platform can be applied across a spectrum of substrate materials used in medical analytical and testing laboratories.

Limitations of the Study

The dendron enhancement of MV capture onto material surface is discussed in this article as a proof of concept. Besides molecule dendricity, other parameters such as material substrate, spacer length, and dendron scaffolds other than the polybenzyl ethers we proposed herein may also affect the performance of the capture devices.

METHODS

All methods can be found in the accompanying Transparent Methods supplemental file.

SUPPLEMENTAL INFORMATION

Supplemental Information can be found online at https://doi.org/10.1016/j.isci.2019.10.014.

ACKNOWLEDGMENTS

We thank Estelle Morvan for her help in NMR experiments, Christine Labrugere for her help in XPS experiments, and Bruno Payre for his help in cryo-SEM imaging. J.-Q.J. acknowledges financial support from China Scholarship Council. M.-C.D. acknowledges financial support from Association France Parkinson.

AUTHOR CONTRIBUTIONS

M.-C.D. and S.N. contributed equally by designing the capture device and dendrons used therein; J.-Q.J. conducted all the experiments and analyzed all the data acquired; C.C. and I.D.A. helped to establish the methodology used in material characterization. All the authors participated in the manuscript preparation.

DECLARATION OF INTERESTS

M.-C.D., S.N., J.-Q.J., and C.C. have published one patent in July 2019 entitled "Ligands for capturing microvesicles and uses thereof."

Received: July 19, 2019
Revised: September 23, 2019
Accepted: October 2, 2019
Published: November 22, 2019

REFERENCES

Alves, I.D., and Lecomte, S. (2019). Study of G-protein coupled receptor signaling in membrane environment by plasmon waveguide resonance. Acc. Chem. Res. *52*, 1059–1067.

Andrews, A.M., Lutton, E.M., Merkel, S.F., Razmpour, R., and Ramirez, S.H. (2016). Mechanical injury induces brain endothelial-derived microvesicle release: implications for cerebral vascular injury during traumatic brain injury. Front Cell Neurosci *10*, 43.

Aupeix, K., Hugel, B., Martin, T., Bischoff, P., Lill, H., Pasquali, J.L., and Freyssinet, J.M. (1997). The significance of shed membrane particles during programmed cell death in vitro, and in vivo, in HIV-1 infection. J. Clin. Invest. *99*, 1546–1554.

Bergen, K., Mobarrez, F., Jorneskog, G., Wallen, H., and Tehrani, S. (2018). Phosphatidylserine expressing microvesicles in relation to microvascular complications in type 1 diabetes. Thromb. Res. *172*, 158–164.

Bruschi, M., Granata, S., Santucci, L., Candiano, G., Fabris, A., Antonucci, N., Petretto, A., Bartolucci, M., Del Zotto, G., Antonini, F., et al. (2019). Proteomic analysis of urinary microvesicles and exosomes in medullary sponge kidney disease and autosomal dominant polycystic kidney disease. Clin. J. Am. Soc. Nephrol. *14*, 834–843.

Calmet, P., De Maria, M., Harte, E., Lamb, D., Serrano-Vega, M., Jazayeri, A., Tschammer, N., and Alves, I.D. (2016). Real time monitoring of membrane GPCR reconstitution by plasmon waveguide resonance: on the role of lipids. Sci. Rep. *6*, 36181.

Chavez, A.S.O., O'Neal, A.J., Santambrogio, L., Kotsyfakis, M., and Pedra, J.H.F. (2019). Message in a vesicle - trans-kingdom intercommunication at the vector-host interface. J. Cell Sci. *132*, jcs224212, https://doi.org/10.1242/jcs.224212.

Chollet, C., Chanseau, C., Brouillaud, B., and Durrieu, M.C. (2007). RGD peptides grafting onto poly(ethylene terephthalate) with well controlled densities. Biomol. Eng. *24*, 477–482.

Chollet, C., Chanseau, C., Remy, M., Guignandon, A., Bareille, R., Labrugere, C., Bordenave, L., and Durrieu, M.C. (2009). The effect of RGD density on osteoblast and endothelial cell behavior on RGD-grafted polyethylene terephthalate surfaces. Biomaterials *30*, 711–720.

Clancy, J.W., Sedgwick, A., Rosse, C., Muralidharan-Chari, V., Raposo, G., Method, M., Chavrier, P., and D'Souza-Schorey, C. (2015). Regulated delivery of molecular cargo to invasive tumour-derived microvesicles. Nat. Commun. *6*, 6919.

van Engeland, M., Nieland, L.J.W., Ramaekers, F.C.S., Schutte, B., and Reutelingsperger, C.P.M. (1998). Annexin V-Affinity assay: a review on an apoptosis detection system based on phosphatidylserine exposure. Cytometry *31*, 1–9.

Fielding, L. (2000). Determination of association constants (Ka) from solution NMR data. Tetrahedron *56*, 6151–6170.

Gajos, K., Kaminska, A., Awsiuk, K., Bajor, A., Gruszczynski, K., Pawlak, A., Zadlo, A., Kowalik, A., Budkowski, A., and Stepien, E. (2017). Immobilization and detection of platelet-derived extracellular vesicles on functionalized silicon substrate: cytometric and spectrometric approach. Anal. Bioanal. Chem. *409*, 1109–1119.

Granqvist, N., Yliperttula, M., Valimaki, S., Pulkkinen, P., Tenhu, H., and Viitala, T. (2014). Control of the morphology of lipid layers by substrate surface chemistry. Langmuir *30*, 2799–2809.

Hankins, H.M., Baldridge, R.D., Xu, P., and Graham, T.R. (2015). Role of flippases, scramblases and transfer proteins in phosphatidylserine subcellular distribution. Traffic *16*, 35–47.

Harte, E., Maalouli, N., Shalabney, A., Texier, E., Berthelot, K., Lecomte, S., and Alves, I.D. (2014). Probing the kinetics of lipid membrane formation and the interaction of a nontoxic and a toxic amyloid with plasmon waveguide resonance. Chem. Commun. (Camb.) *50*, 4168–4171.

Henao Agudelo, J.S., Braga, T.T., Amano, M.T., Cenedeze, M.A., Cavinato, R.A., Peixoto-Santos, A.R., Muscara, M.N., Teixeira, S.A., Cruz, M.C., Castoldi, A., et al. (2017). Mesenchymal stromal cell-derived microvesicles regulate an internal pro-inflammatory program in activated macrophages. Front Immunol. *8*, 881.

Holliday, L.S., Truzman, E., Zuo, J., Han, G., Torres-Medina, R., and Rody, W.J., Jr. (2019). Extracellular vesicle identification in tooth movement models. Orthod. Craniofac. Res. *22* (*Suppl 1*), 101–106.

Hugel, B., Martinez, M.C., Kunzelmann, C., and Freyssinet, J.M. (2005). Membrane microparticles: two sides of the coin. Physiology (Bethesda) *20*, 22–27.

Iba, T., and Ogura, H. (2018). Role of extracellular vesicles in the development of sepsis-induced coagulopathy. J. Intensive Care *6*, 68.

Isono, T., Tanaka, H., and Ogino, T. (2007). Effect of chemical modification of the substrate surface on supported lipid bilayer formation. e-Journal of Surface Science and Nanotechnology *5*, 99–102.

Jayachandran, M., Litwiller, R.D., Owen, W.G., Heit, J.A., Behrenbeck, T., Mulvagh, S.L., Araoz, P.A., Budoff, M.J., Harman, S.M., and Miller, V.M. (2008). Characterization of blood borne microparticles as markers of premature coronary calcification in newly menopausal women. Am. J. Physiol. Heart Circ. Physiol. *295*, H931–H938.

Jeney, V. (2018). Pro-inflammatory actions of red blood cell-derived DAMPs. Exp. Suppl. *108*, 211–233.

Koulov, A.V., Stucker, K.A., Lakshmi, C., Robinson, J.P., and Smith, B.D. (2003). Detection of apoptotic cells using a synthetic fluorescent sensor for membrane surfaces that contain phosphatidylserine. Cell Death Differ *10*, 1357–1359.

Leventis, P.A., and Grinstein, S. (2010). The distribution and function of phosphatidylserine in cellular membranes. Annu. Rev. Biophys. *39*, 407–427.

La Marca, V., and Fierabracci, A. (2017). Insights into the diagnostic potential of extracellular vesicles and their miRNA signature from liquid biopsy as early biomarkers of diabetic micro/macrovascular complications. Int. J. Mol. Sci. *18*, 1974, https://doi.org/10.3390/ijms18091974.

Mecke, A., Uppuluri, S., Sassanella, T.M., Lee, D.K., Ramamoorthy, A., Baker, J.R., Jr., Orr, B.G., and Banaszak Holl, M.M. (2004). Direct observation of lipid bilayer disruption by poly(amidoamine) dendrimers. Chem. Phys. Lipids *132*, 3–14.

Mecke, A., Majoros, I.J., Patri, A.K., Baker, J.R., Jr., Holl, M.M., and Orr, B.G. (2005). Lipid bilayer disruption by polycationic polymers: the roles of size and chemical functional group. Langmuir *21*, 10348–10354.

Meckes, D.G., Jr., and Raab-Traub, N. (2011). Microvesicles and viral infection. J. Virol. *85*, 12844–12854.

Muralidharan-Chari, V., Clancy, J.W., Sedgwick, A., and D'Souza-Schorey, C. (2010). Microvesicles: mediators of extracellular communication during cancer progression. J. Cell Sci. *123*, 1603–1611.

Nagata, S., Suzuki, J., Segawa, K., and Fujii, T. (2016). Exposure of phosphatidylserine on the cell surface. Cell Death Differ *23*, 952–961.

Ngo, H.T., Liu, X., and Jolliffe, K.A. (2012). Anion recognition and sensing with Zn(II)-dipicolylamine complexes. Chem. Soc. Rev. *41*, 4928–4965.

Nievas, Y.R., Coceres, V.M., Midlej, V., de Souza, W., Benchimol, M., Pereira-Neves, A., Vashisht, A.A., Wohlschlegel, J.A., Johnson, P.J., and de Miguel, N. (2018). Membrane-shed vesicles from the parasite Trichomonas vaginalis: characterization and their association with cell interaction. Cell. Mol. Life Sci. *75*, 2211–2226.

Obeid, S., Ceroi, A., Mourey, G., Saas, P., Elie-Caille, C., and Boireau, W. (2017). Development of a NanoBioAnalytical platform for "on-chip" qualification and quantification of platelet-derived microparticles. Biosens. Bioelectron. *93*, 250–259.

Ojida, A., Mito-oka, Y., Inoue, M.-a., and Hamachi, I. (2002). First artificial receptors and chemosensors toward phosphorylated peptide in aqueous solution. J. Am. Chem. Soc. *124*, 6256–6258.

Owens, A.P., 3rd, and Mackman, N. (2011). Microparticles in hemostasis and thrombosis. Circ. Res. *108*, 1284–1297.

O'Neil, E.J., and Smith, B.D. (2006). Anion recognition using dimetallic coordination complexes. Coord. Chem. Rev. *250*, 3068–3080.

Paolicelli, R.C., Bergamini, G., and Rajendran, L. (2019). Cell-to-cell communication by extracellular vesicles: focus on microglia. Neuroscience *405*, 148–157.

Plaunt, A.J., Harmatys, K.M., Wolter, W.R., Suckow, M.A., and Smith, B.D. (2014). Library synthesis, screening, and discovery of modified Zinc(II)-Bis(dipicolylamine) probe for enhanced molecular imaging of cell death. Bioconjug. Chem. *25*, 724–737.

Rautou, P.E., and Mackman, N. (2013). Microvesicles as risk markers for venous thrombosis. Expert Rev. Hematol. *6*, 91–101.

Reimhult, E., Höök, F., and Kasemo, B. (2003). Intact vesicle adsorption and supported biomembrane formation from vesicles in solution: influence of surface chemistry, vesicle size, temperature, and osmotic pressure. Langmuir *19*, 1681–1691.

Rice, D.R., Clear, K.J., and Smith, B.D. (2016). Imaging and therapeutic applications of zinc(ii)-dipicolylamine molecular probes for anionic biomembranes. Chem. Commun. (Camb.) *52*, 8787–8801.

Salamon, Z., and Tollin, G. (2004). Graphical analysis of mass and anisotropy changes observed by plasmon-waveguide resonance spectroscopy can provide useful insights into membrane protein function. Biophys J *86*, 2508–2516.

Salamon, Z., Macleod, H.A., and Tollin, G. (1997a). Coupled plasmon-waveguide resonators: a new spectroscopic tool for probing proteolipid film structure and properties. Biophysical J. *73*, 2791–2797.

Salamon, Z., Macleod, H.A., and Tollin, G. (1997b). Surface plasmon resonance spectroscopy as a tool for investigating the biochemical and biophysical properties of membrane protein systems. I: theoretical principles. Biochim. Biophys. Acta *1331*, 117–129.

Sampaio, N.G., Cheng, L., and Eriksson, E.M. (2017). The role of extracellular vesicles in malaria biology and pathogenesis. Malar. J. *16*, 245.

Segawa, K., and Nagata, S. (2015). An apoptotic 'Eat Me' signal: phosphatidylserine exposure. Trends Cell Biol. *25*, 639–650.

Selmeczi, K., Michel, C., Milet, A., Gautier-Luneau, I., Philouze, C., Pierre, J.L., Schnieders, D., Rompel, A., and Belle, C. (2007). Structural, kinetic, and theoretical studies on models of the zinc-containing phosphodiesterase active center: medium-dependent reaction mechanisms. Chemistry *13*, 9093–9106.

Sun, Y., Huo, C., Qiao, Z., Shang, Z., Uzzaman, A., Liu, S., Jiang, X., Fan, L.Y., Ji, L., Guan, X., et al. (2018). Comparative proteomic analysis of exosomes and microvesicles in human saliva for lung cancer. J. Proteome Res. *17*, 1101–1107.

Svedman, F.C., Lohcharoenkal, W., Bottai, M., Brage, S.E., Sonkoly, E., Hansson, J., Pivarcsi, A., and Eriksson, H. (2018). Extracellular microvesicle microRNAs as predictive biomarkers for targeted therapy in metastastic cutaneous malignant melanoma. PLoS One *13*, e0206942.

Takahashi, T., Kato, A., Berdnikovs, S., Stevens, W.W., Suh, L.A., Norton, J.E., Carter, R.G., Harris, K.E., Peters, A.T., Hulse, K.E., et al. (2017). Microparticles in nasal lavage fluids in chronic rhinosinusitis: potential biomarkers for diagnosis of aspirin-exacerbated respiratory disease. J. Allergy Clin. Immunol. *140*, 720–729.

Taylor, J., and Bebawy, M. (2019). Proteins regulating microvesicle biogenesis and multidrug resistance in cancer. Proteomics *19*, e1800165.

Tricarico, C., Clancy, J., and D'Souza-Schorey, C. (2017). Biology and biogenesis of shed microvesicles. Small GTPases *8*, 220–232.

Wang, Q., and Lu, Q. (2017). Plasma membrane-derived extracellular microvesicles mediate non-canonical intercellular NOTCH signaling. Nat. Commun. *8*, 709.

Wang, Y.L., Lu, Z.Y., and Laaksonen, A. (2012). Specific binding structures of dendrimers on lipid bilayer membranes. Phys. Chem. Chem. Phys. *14*, 8348–8359.

van Weerd, J., Karperien, M., and Jonkheijm, P. (2015). Supported lipid bilayers for the generation of dynamic cell-material interfaces. Adv. Healthc. Mater. *4*, 2743–2779.

Wyllie, M.P., and Ramirez, M.I. (2017). Microvesicles released during the interaction between Trypanosoma cruzi TcI and TcII strains and host blood cells inhibit complement system and increase the infectivity of metacyclic forms of host cells in a strain-independent process. Pathog. Dis. *75*, ftx077, https://doi.org/10.1093/femspd/ftx077.

Zwicker, V.E., Oliveira, B.L., Yeo, J.H., Fraser, S.T., Bernardes, G.J.L., New, E.J., and Jolliffe, K.A. (2019). A fluorogenic probe for cell surface phosphatidylserine using an intramolecular indicator displacement sensing mechanism. Angew. Chem. Int. Ed. *58*, 3087–3091.

ISCI, Volume *21*

Supplemental Information

Dendron-Functionalized Surface: Efficient Strategy for Enhancing the Capture of Microvesicles

Jian-Qiao Jiang, Christel Chanseau, Isabel D. Alves, Sylvain Nlate, and Marie-Christine Durrieu

Supplemental Information

Transparent methods

Synthesis

1) Tert-butyl (6-hydroxyhexyl)carbamate

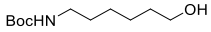

The product is synthesized following the reported procedure.(Xiang, Moulin, Buhler, Maaloum, Fuks and Giuseppone, 2015) 3.72 g of Di-tert-butyl-dicarbonate was added into a solution of 2 g 6-amino-1-hexanol in 40 mL tetrahydrofuran at 0 ℃ under stirring. The reacting mixture was allowed to slowly warm up to room temperature. After 24 h, the solvent was evaporated. The residue was dissolved in dichloromethane 50 mL and was washed with 50 mL of water for 3 times. The organic phase was gathered and dried over sodium sulfate, and then the solvent was removed with a rotary evaporator. The product is colorless oil, and the yield was 91 %. ^{1}H NMR ($CDCl_3$, 300 MHz, 25°C): δ(ppm) 3.60 (t, 2H), 3.08 (t, 2H), 1.59-1.28 (m, 17H);

2) Tert-butyl (6-bromohexyl)carbamate

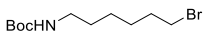

The product is synthesized following the reported procedure.(Segretti, Vallerini, Brochier, Langley, Wang, Hancock and Kozikowski, 2015) To a solution of 1 g tert-butyl (6-hydroxyhexyl)carbamate and 2.1 g triphenylphosphine in 12 mL tetrahydrofuran, a solution of 2.7 g tetrabromomethane in 8 mL tetrahydrofuran was added dropwise at 0 ℃ under stirring. The reacting mixture was allowed to slowly warm up to room temperature. After 24 h of reaction, the solvent was removed. The residue was added into a solvent mixture of 50 mL petroleum ether and 10 mL ethyl acetate. Precipitation formed instantly and then was filtered off while the filtrate was collected and evaporated to leave colorless oil behind. The oil went through a flash column of silica using an eluent of petroleum ether: ethyl acetate= 10:1. The solvent was removed with a rotary evaporator. The product is colorless oil, and the yield was 93 %. ^{1}H NMR ($CDCl_3$, 300 MHz, 25°C): δ(ppm) 3.44 (t, 2H), 3.14 (t, 2H), 1.91-1.86 (m, 2H), 1.52-1.33 (m, 15H);

3) Tert-butyl (6-iodohexyl)carbamate

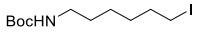

1.5 g tert-butyl (6-bromohexyl)carbamate was dissolved in 15 mL acetonitrile. 4.02 g of sodium iodide was added into the solution. The mixture was stirred under room temperature and kept in darkness for 48 h. The solvent was removed under vacuum, and the residue was extracted between 50 mL of dichloromethane and 50 mL water. The organic phase was washed with a saturated solution of sodium thiosulfate and then dried over sodium sulfate. The solvent was removed with rotary evaporator. The product is colorless oil, and the yield was 96 %. ^{1}H NMR ($CDCl_3$, 300 MHz, 25°C): δ(ppm) 3.21 (t, 2H), 1.90-1.80(m, 2H), 1.56-1.30 (m, 15H);

4) 4-(chloromethyl)phenyl propionate

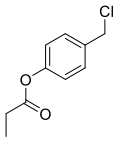

The product is synthesized following the reported procedure.(Johansson, Abrahamsson, Magnuson, Huang, Martensson, Styring, Hammarstrom, Sun and Akermark, 2003) Under stirring, 30 mL propionyl chloride was cooled to 0 ℃. 5.1 g 4-(hydroxymethyl)phenol was added slowly into the flask so as to control the generation of hydrogen chloride at a moderate rate. After the addition, the mixture was allowed to slowly warm up to room temperature. After 12h, the mixture was poured into 500 mL ice-cold water, and then neutralized with sodium bicarbonate. The mixture was then extracted with 50 mL diethyl ether for 3 times. The organic phase was combined and washed with 30 mL water for 3 times. The solution was then dried over sodium sulfate, and the solvent was removed using a rotary evaporator. The product is pale yellow oil, and the yield was 97%. ^{1}H NMR ($CDCl_3$, 300 MHz, 25°C): δ(ppm) 7.42 (d, 2H), 7.12 (d, 2H), 4.60 (s, 2H), 2.62 (q, 2H), 1.30 (t, 3H);

5) 1DPAOH

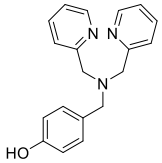

199 mg 4-(chloromethyl)phenyl propionate and 199 mg di-(2-picolyl)amine was dissolved in 10 mL dimethyl sulfoxide under stirring. After adding 414.6 mg potassium carbonate, the mixture was then heated to 60 ℃. 24 h later, the reaction was cooled to room temperature, and then a solution of 0.6 g potassium carbonate in 3 mL water was then added under room temperature. Another 24 h later, the reaction mixture was dissolved in 30 mL dichloromethane, then washed with water (30 mL, 3 times), dried over sodium sulfate. The solvent was removed using a rotary evaporator to give the product as white crystals. The yield was 74%. ^{1}H NMR (DMSO, 300 MHz, 25°C): δ(ppm) 9.31 (s, 1H), 8.51-8.49 (m, 2H), 7.83-7.77 (m, 2H), 7.58 (d, 2H), 7.28-7.24 (m, 2H), 7.20 (d, 2H), 6.73 (d, 2H), 3.68 (s, 4H), 3.51 (s, 2H); ^{13}C NMR (DMSO, 75MHz, 25℃): δ(ppm) 159.80, 156.87, 149.26, 137.08, 130.38, 128.98, 122.87, 122.59, 115.48, 59.33, 57.35;

6) Ligand 1-Boc

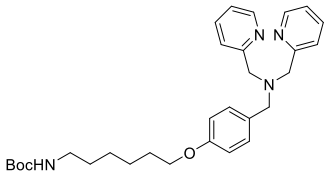

305 mg ligand 1-OH was dissolved in 4 mL dimethylformamide under stirring. 112 mg potassium hydroxide was added to the solution at room temperature. 1 h later, the mixture was cooled to -20 ℃, then 392 mg tert-butyl (6-iodohexyl)carbamate was added into the mixture. The reaction was allowed to slowly warm up to room temperature. 3 h later, the reaction was quenched with water. The mixture was extracted with 20 mL dichloromethane for three times, then the combined

organic phase was washed with 20 mL brine twice, and dried with sodium sulfate. The solvent was removed with rotary evaporator to afford brown oil. The crude product was then purified by silica column chromatography with an eluent of ethyl acetate: acetonitrile= 5:1. The product is pale yellow solid. The yield was 75%.^{1}H NMR (MeOD, 300 MHz, 25°C): δ(ppm) 8.43 (m, 2H), 7.86-7.71 (m, 2H), 7.70 (d, 2H), 7.32-7.28 (m, 4H), 6.89 (d, 2H), 3.99 (t, 2H), 3.77 (s, 4H), 3.61 (s, 2H), 3.06 (t, 2H), 1.81-1.76 (m, 2H), 1.54-1.44 (m, 15H); ^{13}C NMR (MeOD, 75MHz, 25℃): δ(ppm) 159.34, 154.18, 147.94, 137.34, 129.86, 123.88, 123.32, 122.39, 113.99, 67.45, 66.43, 59.12, 57.81, 28.94, 27.39, 25.48;

7) Ligand 1-NH_2

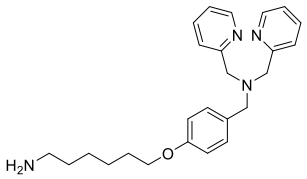

802.2 mg ligand 1-Boc was dissolved in 15 mL tetrahydrofuran. Trifluoroacetic acid was then added into the solution slowly at room temperature. 5 min after the addition of trifluoroacetic acid, the solution was heated to 60 ℃. 30 h later, the solution was cooled to room temperature and then poured into an ice-cold sodium bicarbonate solution. The product was extracted with dichloromethane (30 mL, 3 times). The organic phase was then dried over sodium sulfate and the solvent was removed using rotary evaporator. The yield was 85%. ^{1}H NMR (MeOD, 300 MHz, 25°C): δ(ppm) 8.54 (d, 2H), 7.71-7.66 (m, 2H), 7.60 (d, 2H), 7.19-7.14 (m, 2H), 6.87 (d, 2H), 3.96 (t, 2H), 3.82 (s, 4H), 3.64 (s, 2H), 2.73 (t, 2H), 1.83-1.77 (m, 2H), 1.53-1.41 (m, 6H); ^{13}C NMR (MeOD, 75MHz, 25℃): δ(ppm) 159.94, 158.25, 148.96, 136.44, 130.69, 130.06, 122.81, 121.94, 114.31, 67.86, 59.84, 57.88, 41.88, 33.24, 29.27, 26.66, 25.94;

8) C1

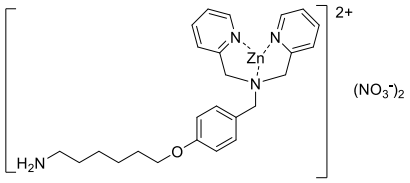

108 mg ligand 1-NH_2 was dissolved in 10 mL methanol at room temperature under stirring. 79.4 mg zinc nitrate hexahydrate was dissolved in 5 mL methanol and was added in to the solution of ligand dropwise. 12 h later, the solvent in the mixture was removed under vacuum to give the final product as pale yellow powder (yield 100%). ^{1}H NMR (DMSO, 300 MHz, 25°C): δ(ppm) 8.69 (d, 2H), 8.12 (t, 2H), 7.66 (m, 4H), 7.30 (d, 2H), 7.02 (d, 2H), 4.25 (d, 2H), 4.02 (t, 2H), 3.71 (t, 4H), 2.80 (t, 2H), 1.78-1.73 (m, 2H), 1.60-1.56 (m, 2H), 1.48-1.39 (m, 6H); ^{13}C NMR (MeOD, 75MHz, 25℃): δ(ppm) 159.34, 154.81, 148.40, 141.26, 133.32, 125.33, 125.19, 123.98, 114.90, 67.88, 56.40, 55.68, 29.22, 29.01, 28.09, 26.10;

9) (5-hydroxy-1,3-phenylene)dimethanol

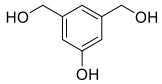

The product is synthesized following the reported procedure.(Turkyilmaz, Rice, Palumbo and Smith, 2014,Jain, Reddy, Paul, K and Bhattacharya, 2009) To a dispersion of 1.3g lithium aluminum hydride in 40 mL anhydrous tetrahydrofuran at 0 ℃, a solution of 3 g dimethyl 5-hydroxyisophthalate in 60 mL anhydrous tetrahydrofuran was added dropwise. The reaction was allowed to warm up to room temperature during 3 hours. After 12 h, the mixture was cooled to 0 ℃ again and quenched with 10% hydrochloric acid. The solvent was removed under reduced pressure. The residue was diluted in 50 mL brine and ethyl acetate was used to extract the product from the aqueous solution (50 mL each time, 6 times in total). The organic layers were combined, dried over sodium sulfate and the solvent was removed using a rotary evaporator. The product is white crystal and the yield was 94%. ^{1}H NMR ($CDCl_3$, 300 MHz, 25°C): δ(ppm) 6.69 (s, 1H), 6.61 (s, 2H), 4.41 (s, 4H);

10) 3,5-bis(bromomethyl)phenol

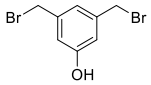

The product is synthesized following the reported procedure. 8.2 mL of 33% hydrogen bromide solution was added dropwise at 0℃ to a solution of 2 g of (5-hydroxy-1,3-phenylene)dimethanol in 20 mL acetic acid. The mixture was stirred 24 h at room temperature. 80 mL of distilled water was then added for an additional 10 min. The mixture was extracted with 70 mL dichloromethane for three times. The combined organic phases were washed with 100 mL water twice, then 100 mL saturated sodium bicarbonate solution twice and again 100 mL water. The organic phase was dried with sodium sulfate, filtered and concentrated. The crude product was purified with a flash column (silica, petroleum ether: ethyl acetate= 9:1) to afford white crystals (yield 90%). ^{1}H NMR ($CDCl_3$, 300 MHz, 25°C): δ(ppm) 3.21 (t, 2H), 1.90-1.80(m, 2H), 1.56-1.30 (m, 15H);

11) 2DPAOH

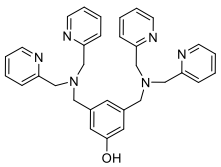

672 mg 3,5-bis(bromomethyl)phenol, 1196 mg N,N-dipycolylamine and 398 mg potassium carbonate was added into 10 mL dimethylformamide under nitrogen protection. The mixture was stirred under room temperature. After 3 hours, 50 mL water was added into the mixture, and was extracted with 50 mL dichloromethane twice. The organic layers were combined and washed with 50 mL water twice, dried over sodium sulfate, filtered and the solvent was evaporated using rotary evaporator. The remainder was purified using silica column chromatography to give the final product as white crystals (yield 80%).^{1}H NMR ($CDCl_3$, 300 MHz, 25°C): δ(ppm) 8.48-8.46 (m, 4H), 7.60-7.58 (m, 8H), 7.11 (q, 4H), 6.96 (s, 1H), 6.86 (s, 2H), 3.79 (s, 8H), 3.57 (s, 4H);

12) Ligand 2-Boc

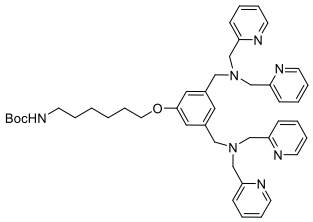

520 mg ligand 2-OH was dissolved in 4 mL dimethylformamide under stirring. 120 mg potassium hydroxide was added to the solution at room temperature. 1 h later, the mixture was cooled to -20 ℃, then 400 mg tert-butyl (6-iodohexyl)carbamate was added into the mixture. The reaction was allowed to slowly warmup to room temperature. 3 h later, the reaction was quenched with water. The mixture was extracted with 20 mL dichloromethane for three times, then the combined organic phase was washed with 20 mL brine twice, and dried with sodium sulfate. The solvent was removed with rotary evaporator to afford brown oil. The crude product was then purified by silica column chromatography with an eluent of ethyl acetate: acetonitrile= 5:1. The product is pale yellow solid. The yield was 75%. ^{1}H NMR (DMSO, 300 MHz, 25°C): δ(ppm) 8.43 (d, 4H), 7.79 (ddd, 4H), 7.28 (tt, 4H), 7.04 (s, 1H), 3.97 (t, 2H), 3.80 (s, 8H), 3.65 (s, 4H), 3.07 (t, 2H), 1.79 (t, 2H), 1.58-1.48 (m, 15H);

13) Ligand 2-NH_2

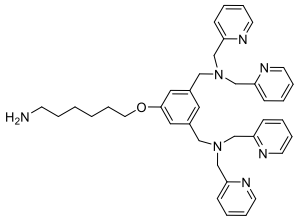

1350 mg ligand 2-Boc was dissolved in 15 mL tetrahydrofuran. 7.2 mL trifluoroacetic acid was then added into the solution slowly at room temperature. 5 min after the addition of trifluoroacetic acid, the solution was heated to 60 ℃. 30 h later, the solution was cooled to room temperature and then poured into an ice-cold sodium bicarbonate solution. The product was extracted with dichloromethane (30 mL, 3 times). The organic phase was then dried over sodium sulfate and the solvent was removed using rotary evaporator. The yield was 85%. ^{1}H NMR (DMSO, 300 MHz, 25°C): δ(ppm) 8.49 (d, 4H), 7.74 (ddd, 4H), 7.57 (d, 4H), 7.25 (dd, 4H), 7.07 (s, 1H), 6.82 (s, 2H), 3.93 (t, 2H), 3.71 (s, 8H), 3.60 (s, 4H), 3.32 (b, 4H), 1.69 (t, 2H), 1.42-1.34 (m, 6H); ^{13}C NMR (MeOD, 75MHz, 25℃): δ(ppm) 159.79, 159.20, 148.97, 140.49, 136.42, 122.76, 121.95, 121.48, 113.56, 67.85, 60.09, 58.63, 41.31, 29.07, 26.81, 26.58, 26.13.

14) C2

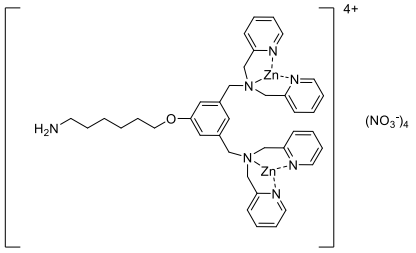

1110 mg ligand 2-NH_2 was dissolved in 10 mL methanol at room temperature under stirring. 1072 mg zinc nitrate hexahydrate was dissolved in 5 mL methanol and was added in to the solution of ligand dropwise. 12 h later, the solvent in the mixture was removed under vacuum to give the final product as pale yellow powder (yield 100%). ^{1}H NMR (DMSO, 300 MHz, 25°C): δ(ppm) 8.71 (b, 4H), 8.11 (t, 4H), 7.67 (t, 4H), 7.60 (d, 4H), 7.01 (b, 2H), 6.89 (s, 1H), 4.35 (d, 2H), 4.07 (b, 2H), 3.81 (d, 8H), 2.84 (t, 2H), 1.79 (b, 2H), 1.65-1.46 (m, 6H); ^{13}C NMR (MeOD, 75MHz, 25°C): δ(ppm) 162.85, 159.27, 155.04, 148.50, 141.37, 134.32, 127.12, 125.32, 117.96, 68.03, 57.51, 56.15, 39.86, 36.26, 31.24, 29.05, 27.79, 26.11, 25.62.

15) 2-(trimethylsilyl)ethyl (6-hydroxyhexyl)carbamate

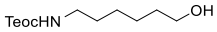

352 mg of 6-amino-1-hexanol was dissolved in 5 mL dichloromethane. 0.9 mL triethylamine was added into the solution and then 850 mg of 4-Nitrophenyl 2-(trimethylsilyl)ethyl carbonate in 1.4 mL dichloromethane was also added into the mixture at room temperature under stirring. After 24 h, the solvent was evaporated. The residue was dissolved in dichloromethane 50 mL and was washed with 50 mL of saturated $NaHCO_3$ solution for 3 times and then 50 mL of 2 M NAOH solution for 3 times. The organic phase was gathered and dried over sodium sulfate, and then the solvent was removed with a rotary evaporator. The product is colorless oil, and the yield was 98 %. ^{1}H NMR ($CDCl_3$, 300 MHz, 25°C): δ(ppm) 4.64 (b, 1H), 4.17 (t, 2H), 3.67 (t, 2H), 3.20 (q, 2H), 1.68-1.34 (m, 8H), 1.00 (t, 2H), 0.07 (s, 9H);

16) 2-(trimethylsilyl)ethyl (6-bromohexyl)carbamate

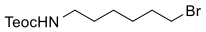

To a solution of 748 mg 2-(trimethylsilyl)ethyl (6-hydroxyhexyl)carbamate and 1311 mg triphenylphosphine in 12 mL tetrahydrofuran, a solution of 1.66 g tetrabromomethane in 8 mL tetrahydrofuran was added dropwise at 0 °C under stirring. The reacting mixture was allowed to slowly warm up to room temperature. After 24 h of reaction, the solvent was removed. The residue was added into a solvent mixture of 50 mL petroleum ether and 10 mL ethyl acetate. Precipitation formed instantly and then was filtered off while the filtrate was collected and evaporated to leave colorless oil behind. The oil went through a flash column of silica using an eluent of petroleum ether: ethyl acetate= 10:1. The solvent was removed with a rotary evaporator. The product is colorless oil, and the yield was 84 %. ^{1}H NMR ($CDCl_3$, 300 MHz, 25°C): δ(ppm) 4.61 (b, 1H), 4.18 (t, 2H), 3.43 (t, 2H), 3.19 (q, 2H), 1.94-1.84 (m, 2H), 1.62-1.34 (m, 6H), 1.00 (t, 2H), 0.07 (s, 9H);

17) 2-(trimethylsilyl)ethyl (6-iodohexyl)carbamate

846 mg 2-(trimethylsilyl)ethyl (6-bromohexyl)carbamate was dissolved in 15 mL acetonitrile. 2 g sodium iodide was added into the solution. The mixture was stirred under room temperature and kept in darkness for 48 h. The solvent was removed under vacuum, and the residue was extracted between 50 mL of dichloromethane and 50 mL water. The organic phase was washed with a saturated solution of sodium thiosulfate and then dried over sodium sulfate. The solvent was removed with rotary evaporator. The product is colorless oil, and the yield was 96 %. ^{1}H NMR ($CDCl_3$, 300 MHz, 25°C): δ(ppm) 4.61 (b, 1H), 4.18 (t, 2H), 3.24-3.16 (m, 4H), 1.89-1.80 (m, 2H), 1.58-1.33 (m, 6H), 1.00 (t, 2H), 0.07 (s, 9H);

18) 3,5-bis(iodomethyl)phenyl propionate

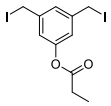

1.15 mL propionyl chloride was dissolved in 30 mL of dichloromethane. At 0℃, 2.8 g 3,5-bis(bromomethyl)phenol dissolved in 10 mL dichloromethane was added into the solution under stirring. 5 min later, 3 mL triethylamine in 10 mL dichloromethane was also added into the solution and the cold bath was removed. 2h after the addition of triethylamine, the reaction was quenched with 10 mL water. The mixture was extracted with 50 mL dichloromethane twice, and the organic phase was combined and washed first with 15 mL saturated sodium bicarbonate solution, then with 15 mL brine. The organic phase was dried with sodium sulfate before the solvent was removed under vacuum.

The product of the above reaction was dissolved in 15 mL acetonitrile. 7.5 g sodium iodide was added into the solution. The mixture was stirred under room temperature and kept in darkness for 48 h. The solvent was removed under vacuum, and the residue was extracted between 50 mL of dichloromethane and 50 mL water. The organic phase was washed with a saturated solution of sodium thiosulfate before the organic phase was collected and dried over sodium sulfate. The solvent was removed with a rotary evaporator. The product is colorless crystal, and the yield was 96 %. ^{1}H NMR ($CDCl_3$, 300 MHz, 25°C): δ(ppm) 7.27 (t, 1H), 7.04 (d, 2H), 4.41 (s, 4H), 2.62 (q, 2H), 1.30 (t, 3H);

19) 4DPAOH

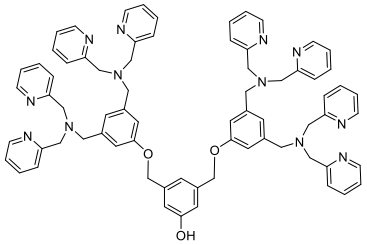

1284 mg ligand 2-OH was dissolved in 4 mL dimethylformamide under stirring. 126 mg potassium hydroxide was added to the solution at room temperature. 1 h later, the mixture was cooled to -20 ℃, then 520 mg 3,5-bis(iodomethyl)phenyl propionate was added into the mixture. The reaction was allowed to slowly warm up to room temperature. 3 h later, the reaction was quenched with water. The mixture was extracted with 20 mL dichloromethane for three times, then

the combined organic phase was washed with 20 mL brine twice, and dried with sodium sulfate. The solvent was removed with rotary evaporator to afford brown oil. The crude product was then purified by silica column chromatography with an eluent of ethyl acetate: acetonitrile= 5:1. The product is pale yellow solid. The yield was 75%. ^{1}H NMR (DMSO, 300 MHz, 25°C): δ(ppm) 8.47 (tt, 8H), 7.71 (ddd, 8H), 7.54-7.51 (m, 8H), 7.20 (qq, 8H), 7.06 (s, 2H), 6.96 (s, 1H), 6.90 (s, 4H), 6.83 (s, 2H), 5.01(s, 4H), 3.70 (s, 16H), 3.57 (s, 8H); ^{13}C NMR ($CDCl_3$, 75MHz, 25°C): δ(ppm) 159.68, 158.63, 157.79, 148.87, 140.61, 139.88, 138.99, 136.64, 122.84, 122.49, 122.05, 117.89, 114.94, 115.18, 69.96, 59.87, 58.33.

20) Ligand 4-Teoc

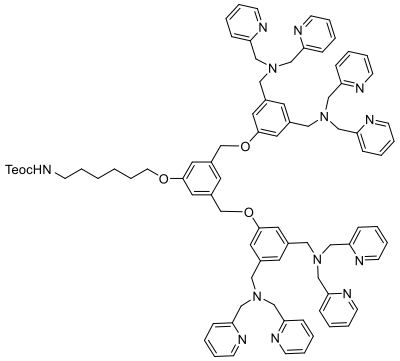

930 mg ligand 4-OH was dissolved in 10 mL dimethylformamide under stirring. 90.5 mg potassium hydroxide was added to the solution at room temperature. 1 h later, the mixture was cooled to -20 ℃, then 360 mg 2-(trimethylsilyl)ethyl (6-iodohexyl)carbamate was added into the mixture. The reaction was allowed to slowly warm up to room temperature. 3 h later, the reaction was quenched with water. The mixture was extracted with 20 mL dichloromethane for three times, then the combined organic phase was washed with 20 mL brine twice, and dried with sodium sulfate. The solvent was removed with rotary evaporator to afford brown oil. The crude product was then purified by silica column chromatography with an eluent of ethyl acetate: acetonitrile= 5:1. The product is pale yellow solid. The yield was 75%. ^{1}H NMR ($CDCl_3$, 300 MHz, 25 ℃): δ(ppm) 8.54-8.51 (m, 8H), 7.65-7.55 (m, 16H), 7.16-7.11 (m, 11H), 7.00-6.98 (m, 6H), 5.05 (s, 4H), 4.17 (t, 2H), 3.97 (t, 2H), 3.82 (s, 16H), 3.68(s, 8H), 3.18 (q, 2H), 1.83-1.72 (m, 2H), 1.54-1.34 (m, 6H), 0.99 (t, 2H), 0.06 (s, 9H); ^{13}C NMR ($CDCl_3$, 75MHz, 25°C): δ(ppm) 162.55, 159.75, 159.67, 159.02, 148.99, 140.73, 139.09, 136.42, 122.73, 121.96, 121.88, 118.52, 113.82, 113.11, 69.91, 67.92, 60.10, 58.57, 40.86, 36.49, 30.94, 30.05, 29.19, 26.54, 25.79, 17.80, -1.44;

21) Ligand 4-NH_2

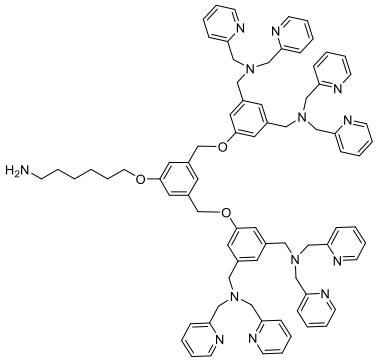

900 mg ligand 4-Teoc was dissolved in 10 mL tetrahydrofuran under stirring. 6.5 mL of 1 M tetrabutylammonium fluoride solution was then added at room temperature. The reaction mixture was then kept at 60 ℃ overnight. After cooled to room temperature, the solvent was removed in vacuo. The residue was dissolved in dichloromethane, and then washed with 50 mL 0.5 M NaOH solution once and 50 mL saturated $NaHCO_3$ solution twice. The organic phase was dried with sodium sulfate. The solvent was removed with rotary evaporator to afford brown solid. The yield was 90%. ^{1}H NMR (DMSO, 300 MHz, 25°C): δ(ppm) 8.48-8.45 (t, 8H), 7.70 (ddd, 8H), 7.51 (d, 8H), 7.22 (ddd, 8H), 7.11 (s, 1H), 7.06 (s, 2H), 6.97 (s, 2H), 6.92 (s, 4H), 5.07 (s, 4H), 3.89 (t, 2H), 3.69 (s, 16H), 3.57 (s, 8H), 1.61 (t, 2H), 1.37-1.19 (m, 6H); ^{13}C NMR (DMSO, 75MHz, 25℃): δ(ppm) 159.61, 159.29, 158.79, 149.79, 149.26, 140.72, 139.49, 136.95, 122.81, 122.57, 121.69, 114.10, 113.30, 69.48, 59.66, 57.94, 55.39, 41.52, 32.60, 29.05, 26.48, 25.80; ESI-MS: m/z: 1250.68 [M-H$^+$] (calcd 1250.68).

22) C4

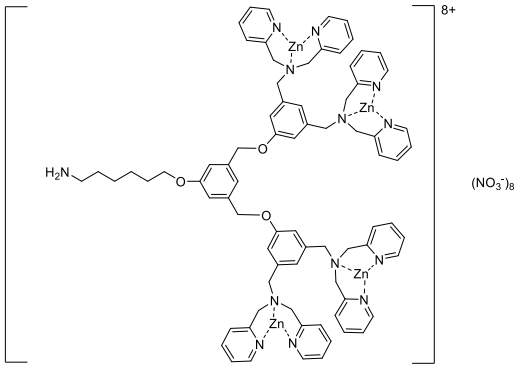

125 mg ligand 4-NH_2 was dissolved in 10 mL methanol at room temperature under stirring. 119 mg zinc nitrate hexahydrate was dissolved in 5 mL methanol and was added in to the solution of ligand dropwise. 12 h later, the solvent in the mixture was removed under vacuum to give the final product as brown powder (yield 100%). ^{1}H NMR (DMSO, 300 MHz, 25°C): δ(ppm) 8.70 (d, 8H), 8.10 (t, 8H), 7.67 (t, 8H), 7.58 (d, 8H), 7.27 (s, 1H), 7.17 (s, 4H), 7.06 (s, 1H), 6.96 (s, 2H), 5.27 (s, 4H), 4.38 (d, 8H), 4.10 (q, 2H), 3.83 (t, 16H), 2.81 (t, 2H), 2.22 (t, 2H), 1.55 (t, 2H), 1.44-1.32 (m, 4H); ^{13}C NMR (DMSO, 75MHz, 25℃): δ(ppm) 159.44, 159.08, 154.85, 148.45, 141.27, 139.20, 134.29, 127.73, 125.32, 125.13, 118.35, 114.09, 69.86, 68.05, 57.42, 56.14, 49.09, 29.27, 26.05, 25.55, 20.34, 19.72;

23) 8DPAOH

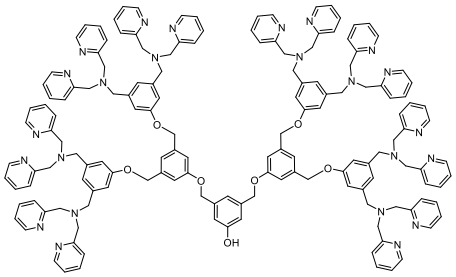

1151 mg (1 mmol) ligand 4-OH was dissolved in 4 mL dimethylformamide under stirring. 126 mg (2.25 mmol) potassium hydroxide was added to the solution at room temperature. 1 h later, the mixture was cooled to -20 ℃, then 220 mg (0.51 mmol) 3,5-bis(iodomethyl)phenyl propionate

was added into the mixture. The reaction was allowed to slowly warm up to room temperature. 3 h later, the reaction was quenched with water. The mixture was extracted with 20 mL dichloromethane for three times, then the combined organic phase was washed with 20 mL brine twice, and dried with sodium sulfate. The solvent was removed with rotary evaporator to afford brown oil. The crude product was then purified by silica column chromatography with an eluent of ethyl acetate: acetonitrile= 5:1. The product is pale yellow solid. The yield was 75%. ^{1}H NMR (DMSO, 300 MHz, 25°C): δ(ppm) 8.48-8.44 (m, 16H), 7.74-7.64 (m, 16H), 7.54-7.51 (m, 16H), 7.22-7.14 (m, 16H), 7.07 (d, 6H), 6.96 (s, 1H), 6.90 (d, 8H), 6.83 (s, 2H), 6.79 (s, 1H), 6.75 (s, 1H), 6.71 (s, 1H), 6.66 (s, 1H), 5.05-4.97(m, 12H), 3.69 (d, 32H), 3.57 (d, 16H); ^{13}C NMR ($CDCl_3$, 75MHz, 25℃): δ(ppm) 159.68, 158.63, 157.79, 148.87, 140.61, 139.88, 138.99, 136.64, 122.84, 122.49, 122.05, 117.89, 114.94, 115.18, 69.96, 59.87, 58.33.

24) Ligand 8-Teoc

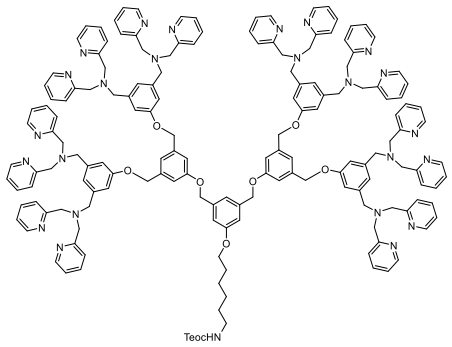

605 mg (0.25 mmol) ligand 8-OH was dissolved in 10 mL dimethylformamide under stirring. 30 mg (0.54 mmol) potassium hydroxide was added to the solution at room temperature. 1 h later, the mixture was cooled to -20 ℃, then 95 mg (0.256 mmol) 2-(trimethylsilyl)ethyl (6-iodohexyl)carbamate was added into the mixture. The reaction was allowed to slowly warm up to room temperature. 3 h later, the reaction was quenched with water. The mixture was extracted with 20 mL dichloromethane for three times, then the combined organic phase was washed with 20 mL brine twice, and dried with sodium sulfate. The solvent was removed with rotary evaporator to afford brown oil. The crude product was then purified by silica column chromatography with an eluent of ethyl acetate: acetonitrile= 5:1. The product is pale yellow solid. The yield was 73%. ^{1}H NMR (DMSO, 300 MHz, 25°C): δ(ppm) 8.47-8.43 (m, 16H), 7.72-7.63 (m, 16H), 7.53-7.47 (m, 16H), 7.23-7.13 (m, 16H), 7.00 (b, 2H), 6.93-6.88 (m, 9H), 6.81 (s, 1H), 6.78 (s, 1H), 5.13-4.99 (m, 12H), 4.05-3.98 (m, 2H), 3.67 (d, 32H), 3.55 (d, 16H), 1.71-1.58 (m, 2H), 1.43-1.20 (m, 8H), 0.94-0.84 (m, 2H), 0.00(s, 9H); ^{13}C NMR ($CDCl_3$, 75MHz, 25℃): δ(ppm) 162.55, 159.75, 159.67, 159.02, 148.99, 140.73, 139.09, 136.42, 122.73, 121.96, 121.88, 118.52, 113.82, 113.11, 69.91, 67.92, 60.10, 58.57, 40.86, 36.49, 30.94, 30.05, 29.19, 26.54, 25.79, 17.80, -1.44;

25) Ligand 8-NH_2

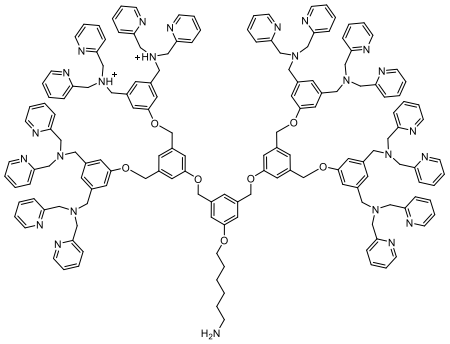

400 mg (0.15 mmol) ligand 8-Teoc was dissolved in 10 mL tetrahydrofuran under stirring. 1.5 mL of 1 M tetrabutylammonium fluoride solution was then added at room temperature. The reaction mixture was then kept at 60 ℃ overnight. After cooled to room temperature, the solvent was removed in vacuo. The residue was dissolved in dichloromethane, and then washed with 50 mL 0.5 M NaOH solution once and 50 mL saturated $NaHCO_3$ solution twice. The organic phase was dried with sodium sulfate. The solvent was removed with rotary evaporator to afford brown solid. The yield was 90%. ^{1}H NMR (DMSO, 300 MHz, 25°C): δ(ppm) 8.45-8.43 (m, 16H), 7.73-7.58 (m, 16H), 7.56-7.45 (m, 16H), 7.24-7.11 (m, 18H), 7.10-6.97 (m, 10H), 6.93-6.88 (m, 9H), 5.05-4.99 (m, 12H), 3.91-3.84 (m, 2H), 3.67 (b, 32H), 3.55 (b, 16H), 1.64-1.56 (m, 2H), 1.37-1.23 (m, 8H); ^{13}C NMR (DMSO, 75MHz, 25°C): δ(ppm) 159.61, 159.29, 158.79, 149.79, 149.26, 140.72, 139.49, 136.95, 122.81, 122.57, 121.69, 114.10, 113.30, 69.48, 59.66, 57.94, 55.39, 41.52, 32.60, 29.05, 26.48, 25.80; ESI-MS: m/z: 2520.30 [M-H^+] (calcd 2520.30), 1260.66 [M-2H^+] (calcd 1260.65).

26) Complex 8-NH_2

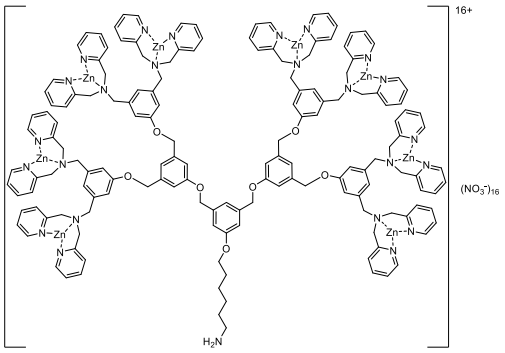

250 mg (0.1 mmol) ligand 8-NH_2 was dissolved in 10 mL methanol at room temperature under stirring. 30 mg (1 mmol) zinc nitrate hexahydrate was dissolved in 5 mL methanol and was added in to the solution of ligand dropwise. 12 h later, the solvent in the mixture was removed under vacuum to give the final product as brown powder (yield 100%). ^{1}H NMR (DMSO, 300 MHz, 25°C): δ(ppm) 8.45 (b, 16H), 7.67 (b, 16H), 7.51 (b, 16H), 7.20 (b, 18H), 7.07 (b, 9H), 6.90 (b, 10H), 5.05 (b, 12H), 3.90 (b, 2H), 3.67 (b, 32H), 3.56 (b, 16H), 1.58 (b, 2H), 1.25 (b, 8H); ^{13}C NMR (DMSO, 75MHz, 25°C): δ(ppm) 159.44, 159.08, 154.85, 148.45, 141.27, 139.20, 134.29, 127.73, 125.32, 125.13, 118.35, 114.09, 69.86, 68.05, 57.42, 56.14, 49.09, 29.27, 26.05, 25.55, 20.34, 19.72;

The functionalization of PET films with complexes:

10 cm^2 PET films were first cleaned with ethanol, and then immersed in a hydrolysis solution (20 mL water, 20 mL acetonitrile and 0.2 g NaOH). The hydrolysis was kept at 60 ℃ for 18 h. The films were cleaned with water, and then immersed in an oxidation solution (38.4 ml fresh milliQ water, 1.6 ml H_2SO_4, 2 g $KMnO_4$). The oxidation was kept at 60 ℃ for 1 h. The oxidized film was washed first with 50% HCl once and then water 3 times. The oxidized films were immersed in the activation solution (MES hydrate 390.5 mg/2 mmol, ethylcarbodiimide hydrochloride(EDC) 766.8 mg/4 mmol, N-hydroxysuccinimide(NHS) 230.18 mg/2 mmol), then kept at room temperature for 1h. The films were washed with water. The activated films were subsequently immersed in 20 mL 1 mM solution of complexes in DMSO under room temperature. 24 h later, the films were removed from the solution and washed intensively with water.

The TBO characterization:

First, a linear correlation between TBO concentration in 50% AcOH and the solution's absorbance @ 633nm (200 μL solution in each well of a transparent 96 well plate) was established using a series of TBO solutions shown in Table S1. In future TBO tests, 5 mL 50% acetic acid would be used to remove the TBO dye adsorbed on 1 cm^2 squares, and 200 μL of each solution would also be added into each individual well of a transparent 96 well plate for absorbance test. Thus TBO concentrations in Table S1 can then be further converted into molecule density on PET surface. The plot was then linearly fitted, as shown in Figure S1.

Table S1. TBO solutions used in absorbance calibration, Related to Figure 6.

Desired TBO concentration (mM)	TBO solution used for dilution	50% (V/V) acetic acid (μL)	Total amount
0.5	100 μL of TBO 5mM	900	1mL
0.1	200 μL of TBO 5mM	800	1mL
0.05	100 μL of TBO 0.5mM	900	1mL
0.01	200 μL of TBO 0.5mM	800	1mL
0.005	100 μL of TBO 0.05mM	900	1mL
0.001	200 μL of TBO 0.05mM	800	1mL
0.0005	100 μL of TBO 0.005mM	900	1mL
0.0001	200 μL of TBO 0.005mM	800	1mL
0.00005	100 μL of TBO 0.0005mM	900	1mL
0.00001	200 μL of TBO 0.0005mM	800	1mL

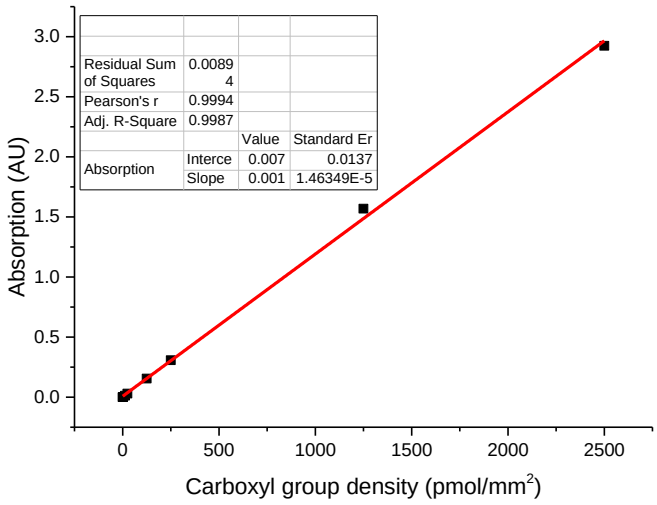

Figure S1. Calibration curve of carboxyl group density plotted against absorbance @ 633 nm, Related to Figure 6.

After acquiring the calibration curve, the TBO test was performed: A $5x10^{-4}$ M solution of toluidine blue-o solution was prepared by first dissolving NaOH into milli-Q water until pH 10, then dissolving toluidine blue-o to reach desired concentration. 1 cm by 1 cm PET squares were

immersed in 10 mL of the TBO solution and then were kept under shaking in darkness at room temperature. 6 hours later, the supernatant was removed from tube and the stained PET surface was washed with 10 mL NaOH solution (pH 10) once and 10 mL pure water twice. The stained films were then immersed in 5 mL 50% acetic acid to remove the adsorbed TBO dye during 10 min. 200 μL of the washed solution from each sample was loaded into 96 well plate and the absorption at 633 nm is measured with a 96 well plate reader. The absorbance was then translated to the surface density of carboxyl groups and summarized in Figure 6 using the calibration curve shown in Figure S1.

X-ray photoelectron spectroscopy (XPS)

A VG Scientific ESCALAB photoelectron spectrometer was used for the surface analysis with a non-monochromatized MgK 1253.6 eV source of 100 W. The area of the analytical X-ray spot on the sample surface is about 250 microns. We used a 45 degree insert angle that corresponds to 3-5 nm of analyzed depth. A flood gun was used for charge compensation. Acquisition of high resolution spectra was done at constant pass energy of 20 eV. Fitting was then realized with software provided by VG Scientific, each spectrum being referenced to carbon pollution at 284.8 eV. Binding energies values are given with a precision of ±0.2 eV.

Microvesicle preparation

Microvesicles were collected from mesenchymal stem cells. After 6 passages, TNFα was introduced into the incubation medium at a concentration of 100 ng/ml. After 36 h, the supernatant was collected, and then purified in 3 steps: 1) Removal of cellular debris: Centrifuge the incubation supernatant at 4 ℃ 1500 g for 15 min, take the supernatant and centrifuge at 4 ℃ 13000 g for another 2 min. 2) Concentrating microvesicles: Take the supernatant again, centrifuge at 4 ℃ 20000 g for 90 min and then take the pellet. 3) Wash the microvesicles: Re-disperse the pellet in 500 μL 1x PBS of 4 ℃, centrifuge at 4 ℃ 20000 g for 90 min. Remove 400 μL of the supernatant without disturbing the pellet, then add another 400 μL fresh 1x PBS of 4 ℃, re-disperse again, and centrifuge at 4 ℃ 20000 g for 90 min. Remove 450 μL of the supernatant without disturbing the pellet, then add 50 μL 1x PBS of 4 ℃ to redisperse the pellet. When not being used, the microvesicles were stored at – 80 ℃.

Microvesicle staining

Stock of microvesicles was allowed to warm up to room temperature, and then 950 μL 1x PBS was used to dilute the suspension. 1 μL CellMask™ Deep Red Plasma membrane Stain was added into the diluted suspension to stain the microvesicles under room temperature. 15 min later, the stained suspension was centrifuged at 4 ℃ 20000 g for 90 min. 950 μL of the supernatant was then removed without disturbing the pellet, and another 950 μL of fresh PBS was added to redisperse the pellet. The centrifugation-redispersion step was repeated twice so as to remove the free CellMask™ Deep Red molecules from the PBS buffer.

Microvesicle characterization using fluorescence microscope:

Stained microvesicles were visible under fluorescence microscope (Leica microsystem DM5500B, microscope with a motorized, programmable stage using a CoolSnap HQ camera controlled by Metamorph 7.6).

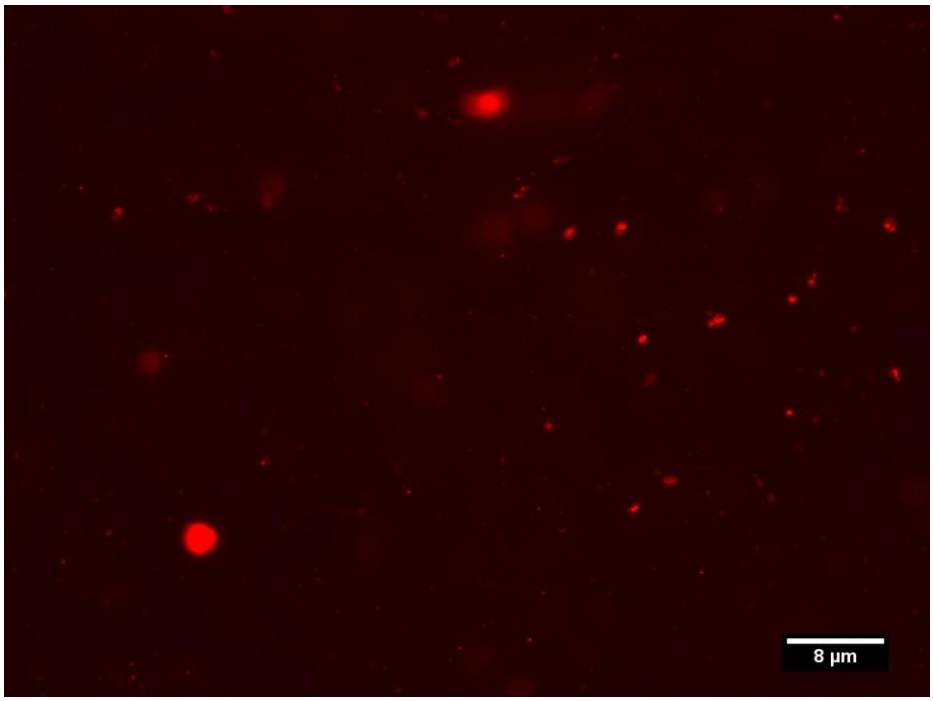

Figure S2: fluorescence micrograph of CellMask™ Deep Red stained microvesicle suspension, Related to Figure 7.

Microvesicle characterization using nanoparticle tracking analysis (NTA):

NTA experiment of prepared microvesicles was performed using NanoSight NS300 instrument. The analysis was performed under 22 ℃, using 532nm laser beam as light source. The instrument was calibrated using the standard nanoparticle dispersions provided by the manufacturer before test.

For the test, stock of microvesicles was allowed to warm up to room temperature, and then 1x PBS was used to dilute the suspension to 1 mL. The suspension was then vortexed to reach an even distribution of microvesicles inside the dilution.

The NTA experiment was performed by 5 video recordings of 30s of the microvesicle dispersion flowing through the sample chamber at the syringe pump speed of 70 (AU).

The videos were simultaneously analyzed by software NTA 3.2 Dev Build 3.2.16, where the microvesicle concentration and size distribution per frame of picture were recorded.

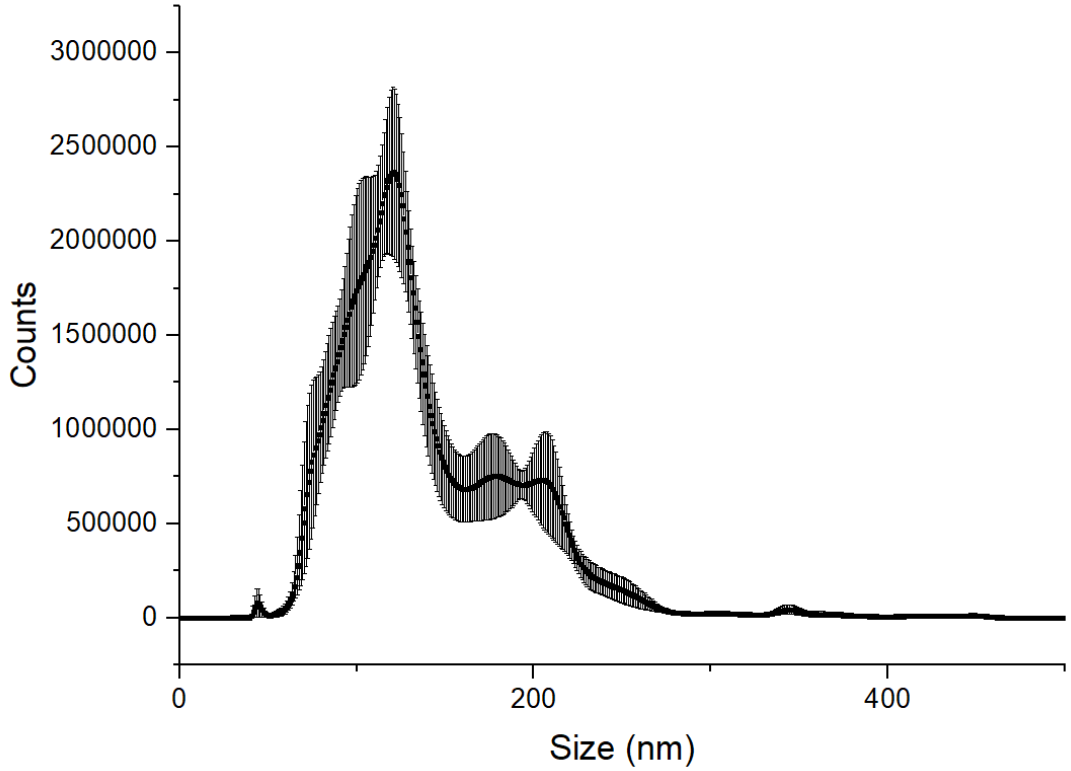

Figure S3. microvesicle size distribution according to NTA analysis, Related to Figure 7.

Microvesicle capture

For all materials, the same procedure was used to capture the microvesicles: The stock microvesicle (stained with CellMask™ Deep Red for FL microscopy and nonstained for Cryo-scanning electron microscopy) dispersion was diluted to 2 mL with 1 × PBS. 250 µL of the dispersion was added onto a functionalized 1 cm^2 PET square and was incubated under room temperature for 15 min. The PET squares were then washed with milli-Q water to remove any free vesicles adhered to the surface.

Observation of captured microvesicles using FL microscope

After the capturing process, fluorescence microscopy (Leica microsystem DM5500B, microscope with a motorized, programmable stage using a CoolSnap HQ camera controlled by Metamorph 7.6) of PET sheets was used to evaluate the capture ability of PET functionalized with different complexes.

Observation of captured microvesicles using Cryo-scanning electron microscopy (Cryo-SEM)

After the capturing process, PET sheets were mounted on freezing stub for the preparation chamber Quorum PP3000T specimen shuttle. The whole was plunged in slush nitrogen paste for cryo-fixation. After quick transfer under vacuum in the preparation chamber the samples were sublimed at -95 ℃ during 30 min and then coated by platinum sputtering. They were at last transferred in the cryo-SEM Quanta 250 FEG chamber and kept at -140 ℃ for observation at an accelerating voltage of 10kV.

NMR & MS spectra of synthesized compounds:

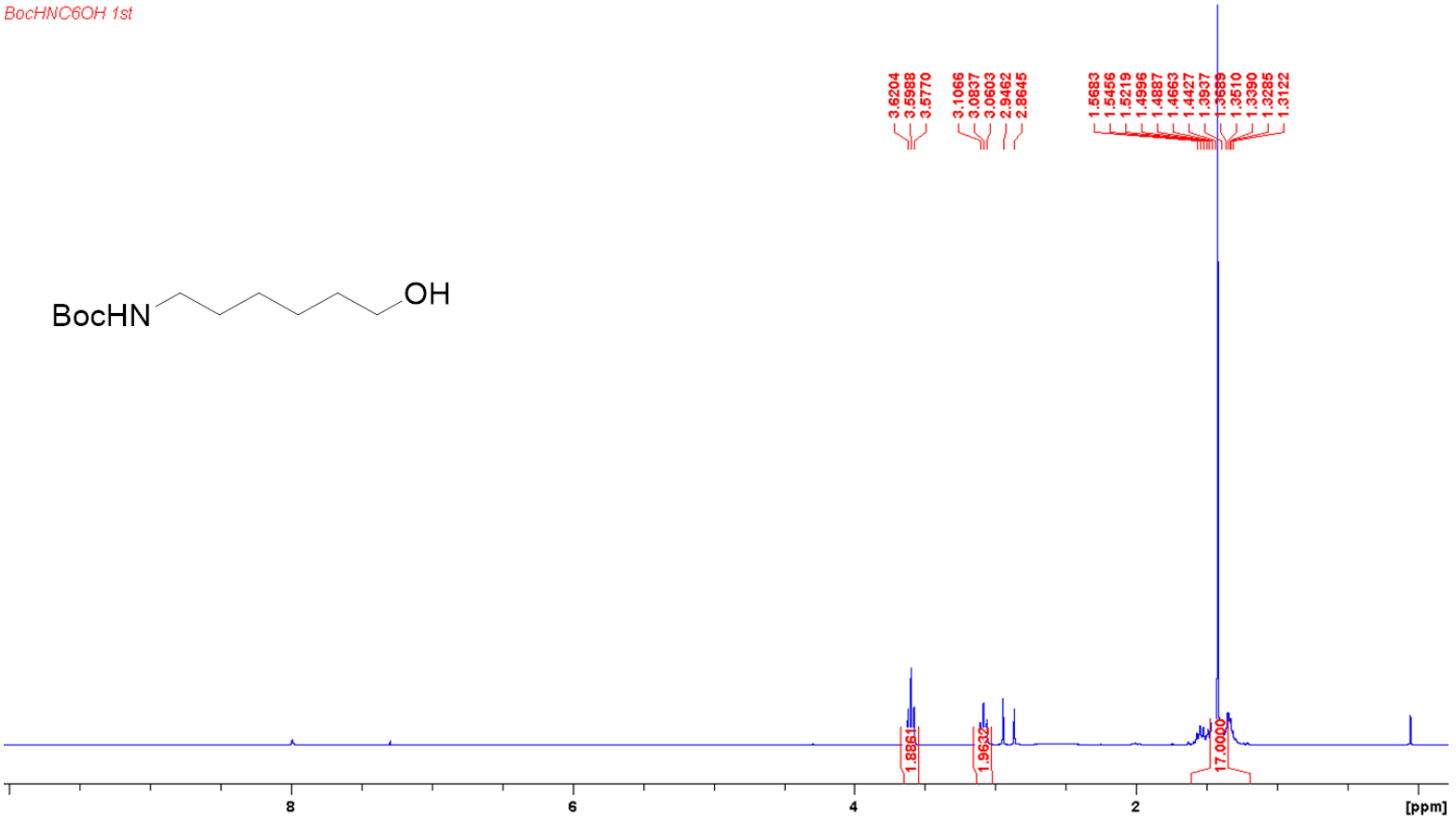

Figure S4. ^{1}H NMR spectrum of Tert-butyl (6-hydroxyhexyl)carbamate. Related to Scheme 2.

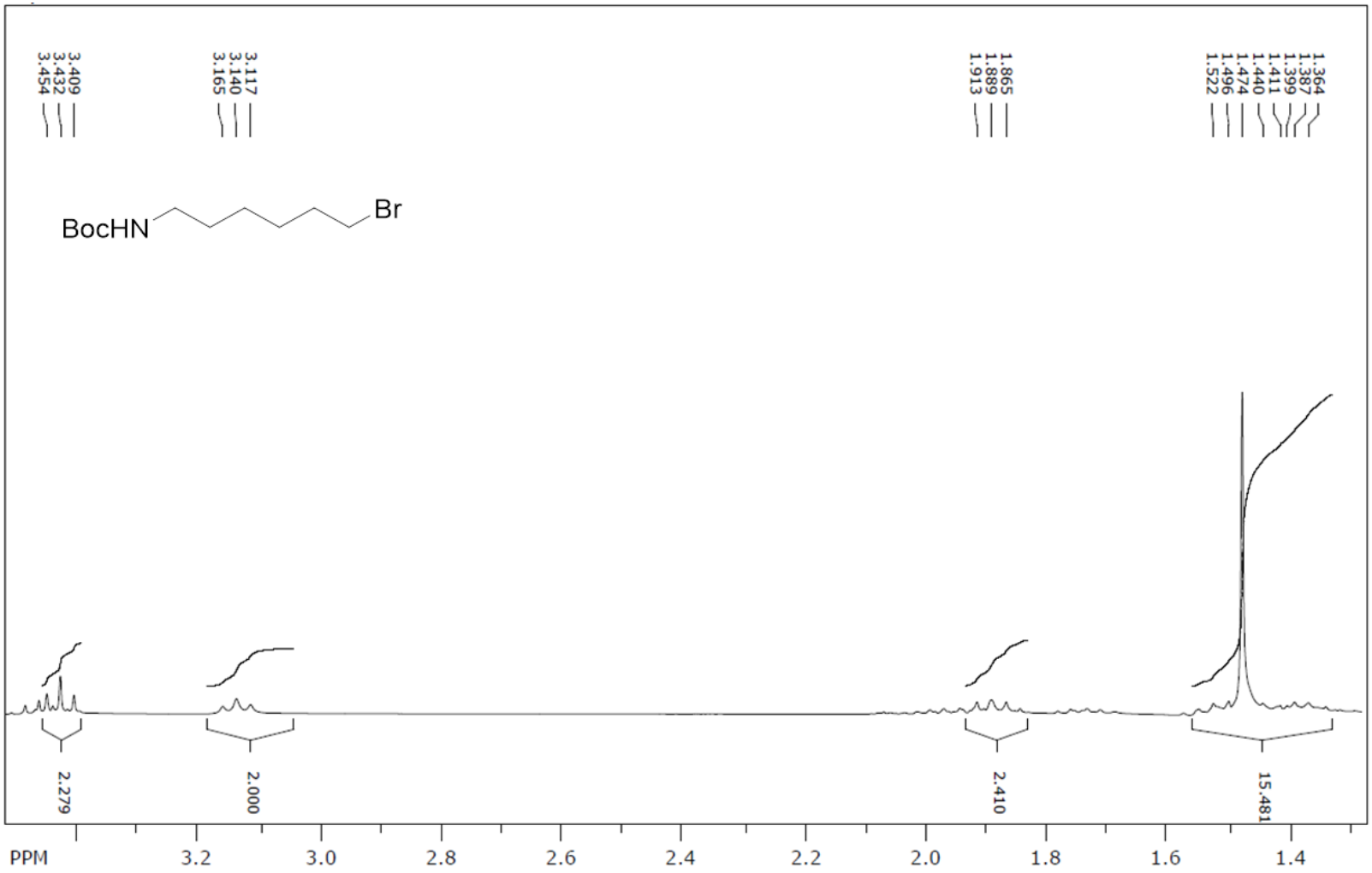

Figure S5. ^{1}H NMR spectrum of Tert-butyl (6-bromohexyl)carbamate, Related to Scheme 2.

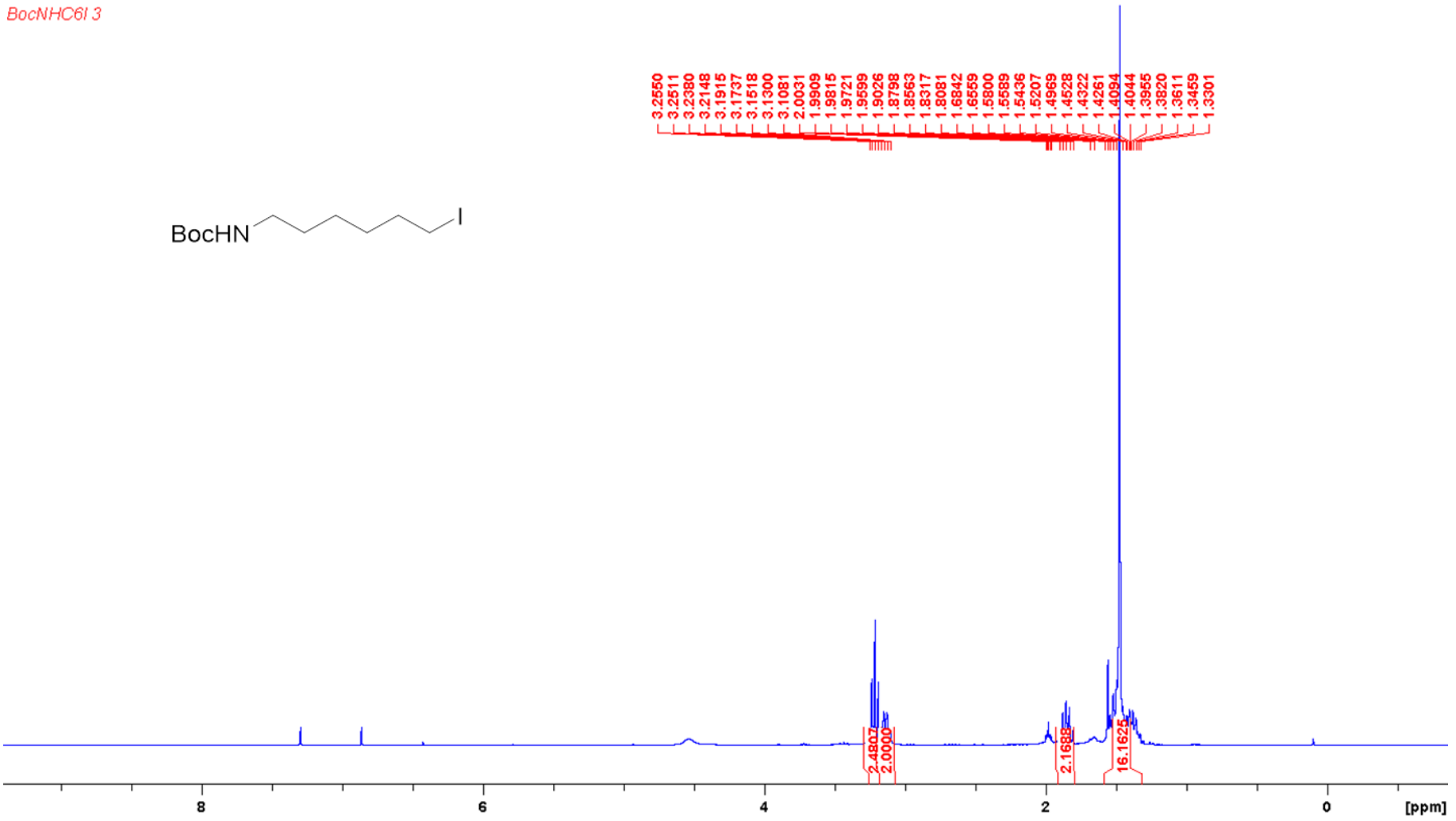

Figure S6. ^{1}H NMR spectrum of tert-butyl (6-iodohexyl)carbamate, Related to Scheme 2.

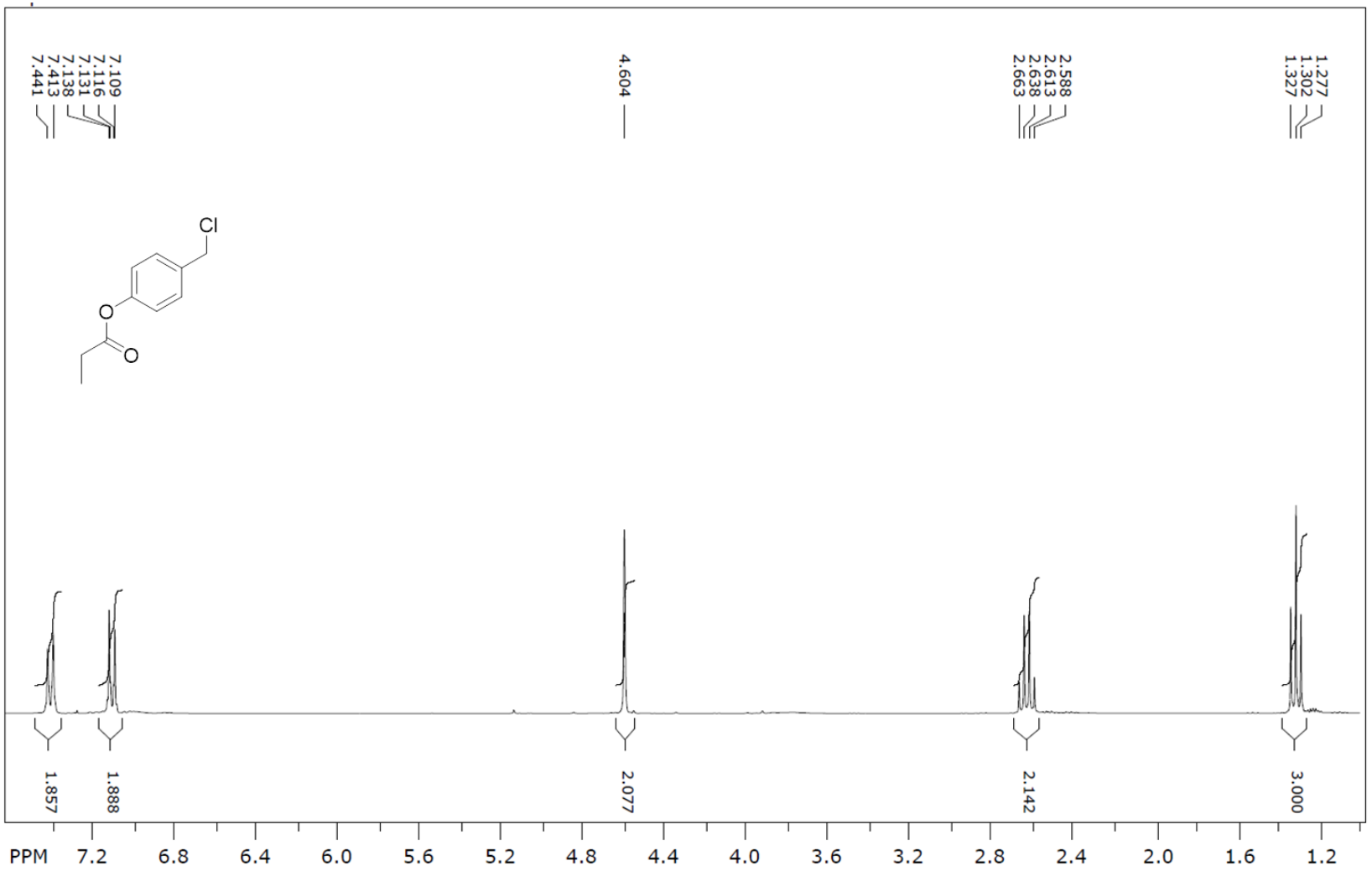

Figure S7. ^{1}H NMR spectrum of 4-(chloromethyl)phenyl propionate, Related to Scheme 2.

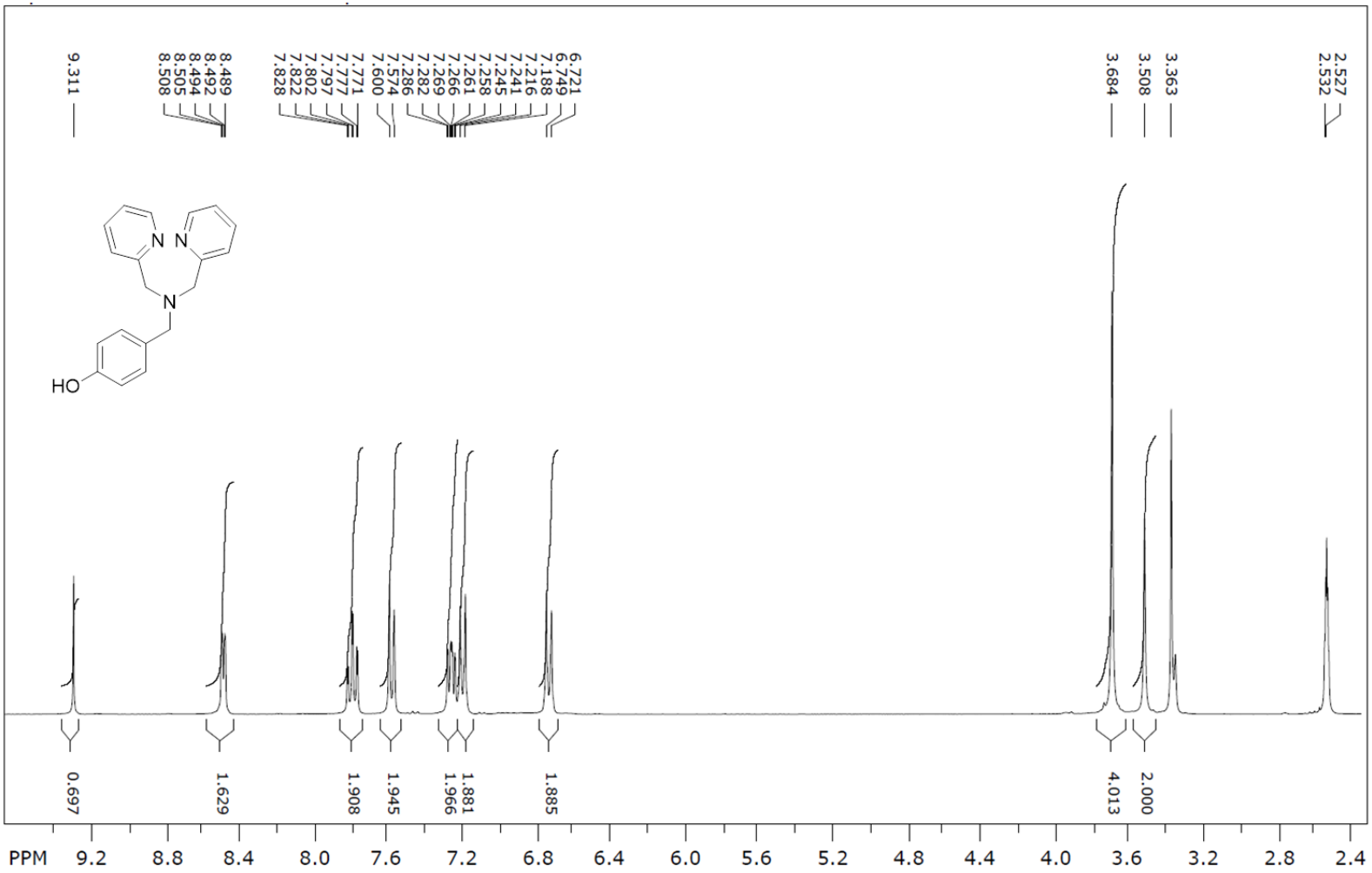

Figure S8. ^{1}H NMR spectrum of 1DPAOH, Related to Scheme 2.

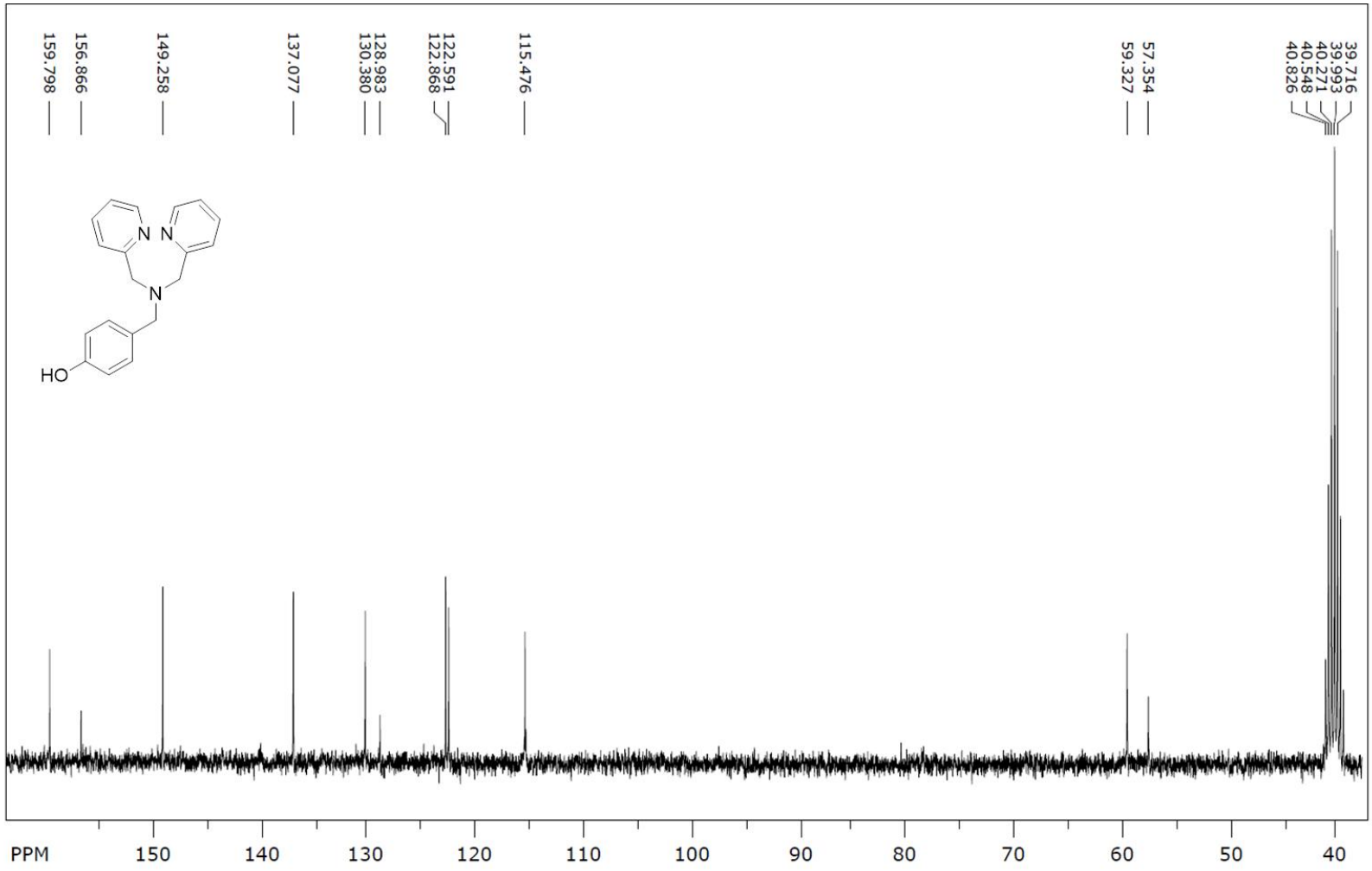

Figure S9. ^{13}C NMR spectrum of 1DPAOH, Related to Scheme 2.

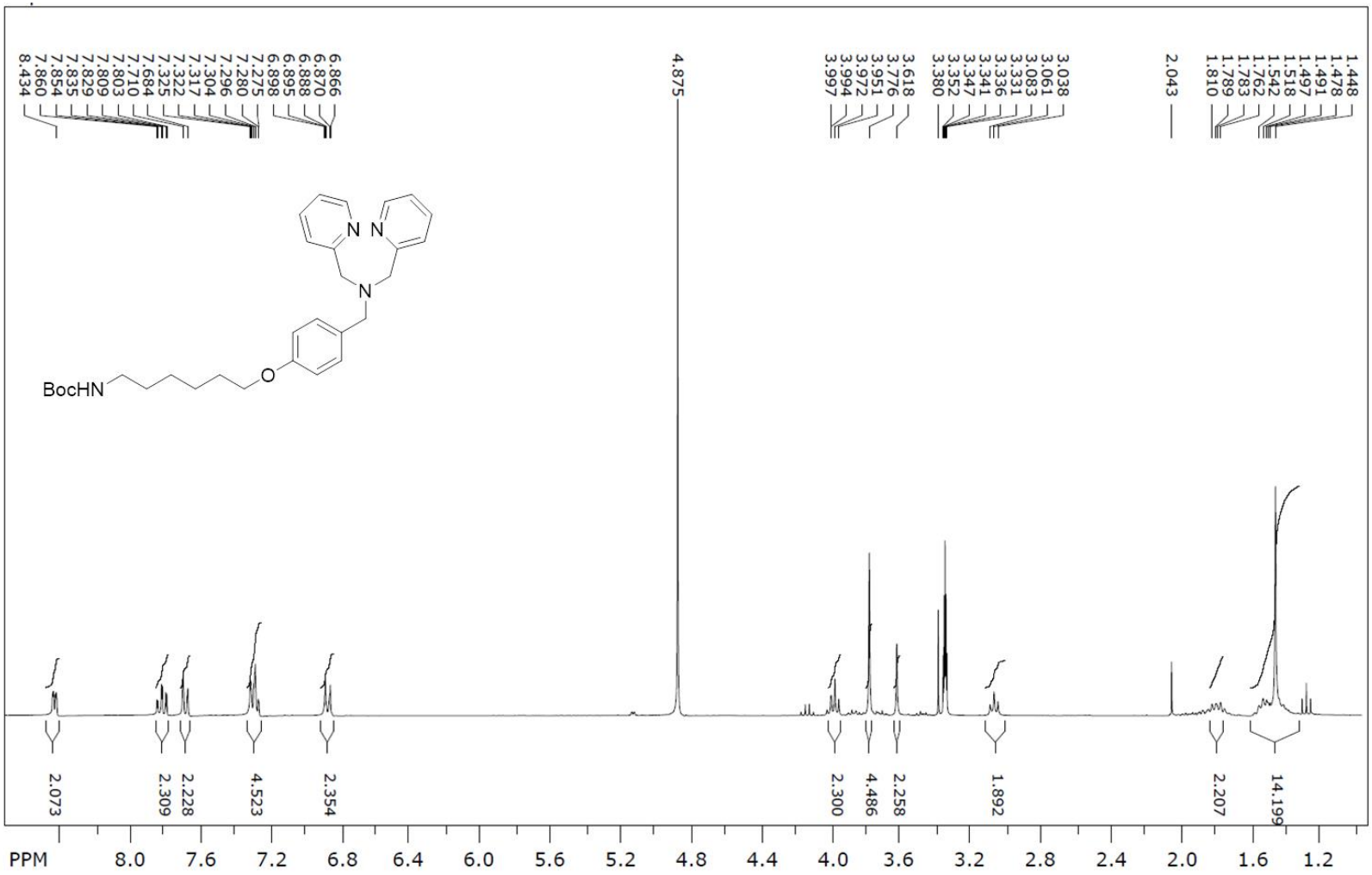

Figure S10. ^{1}H NMR spectrum of Ligand 1-Boc, Related to Scheme 2.

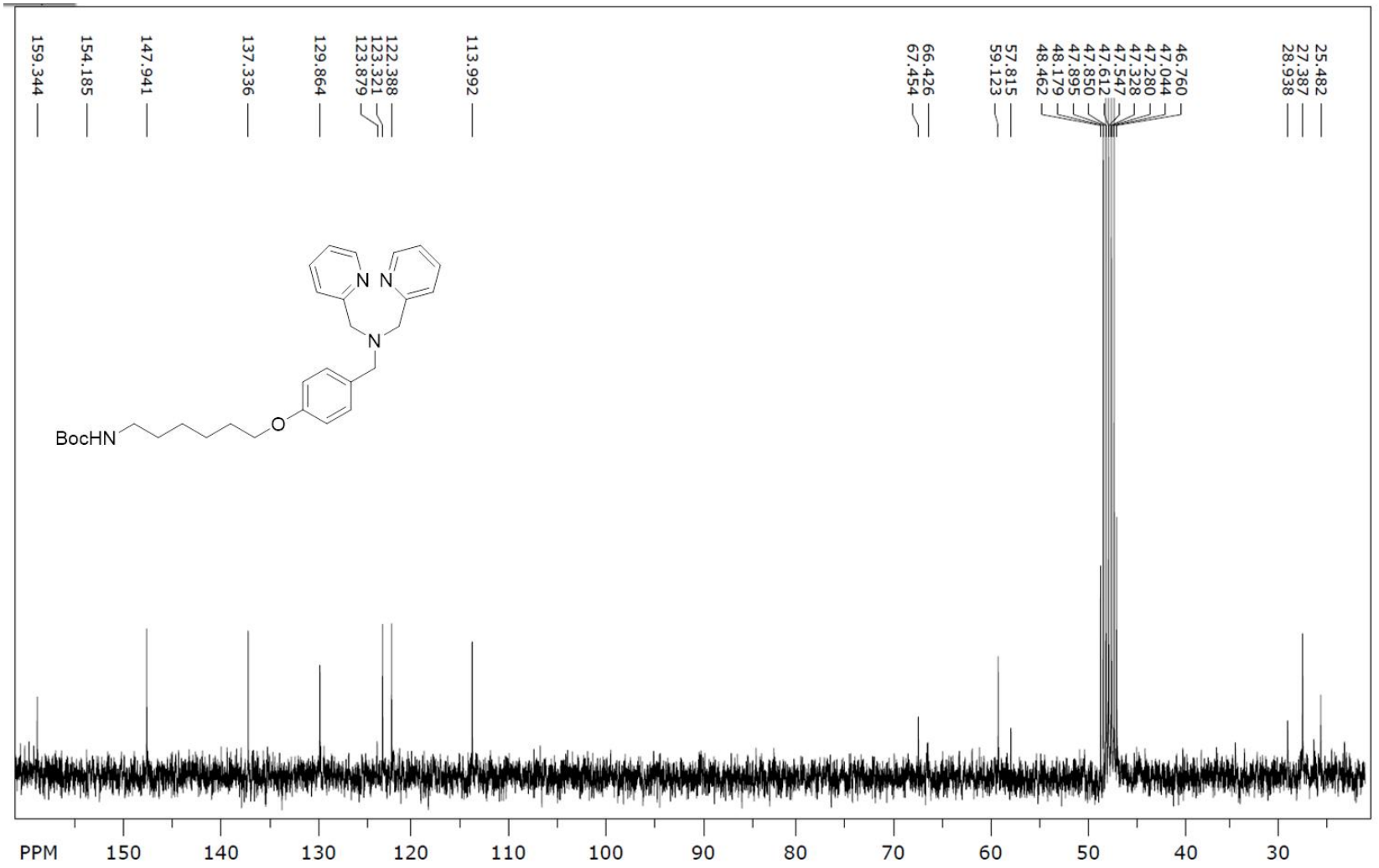

Figure S11. ^{13}C NMR spectrum of Ligand 1-Boc, Related to Scheme 2.

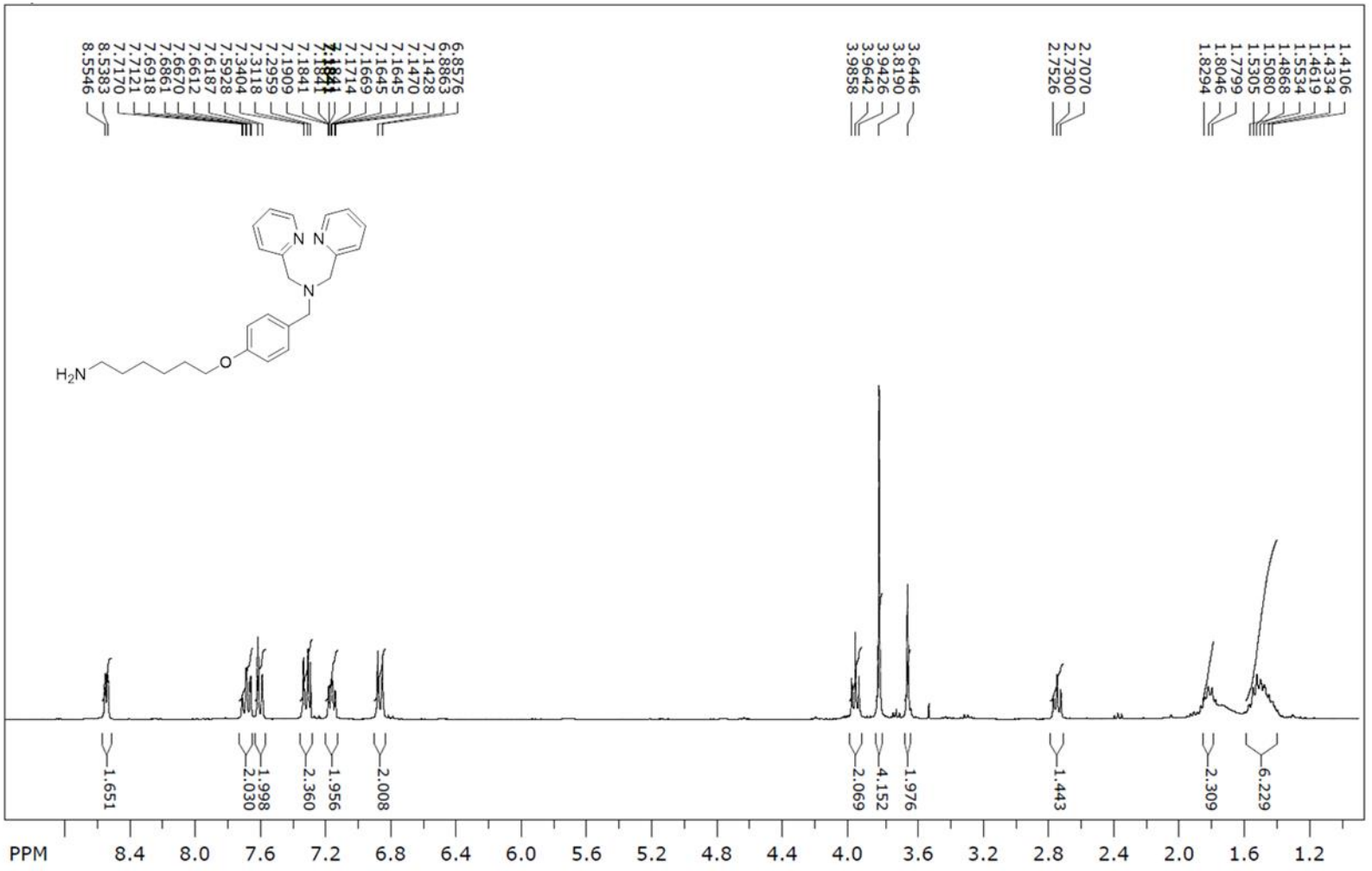

Figure S12. ^{1}H NMR spectrum of Ligand 1-$NH_{2,}$ Related to Scheme 2.

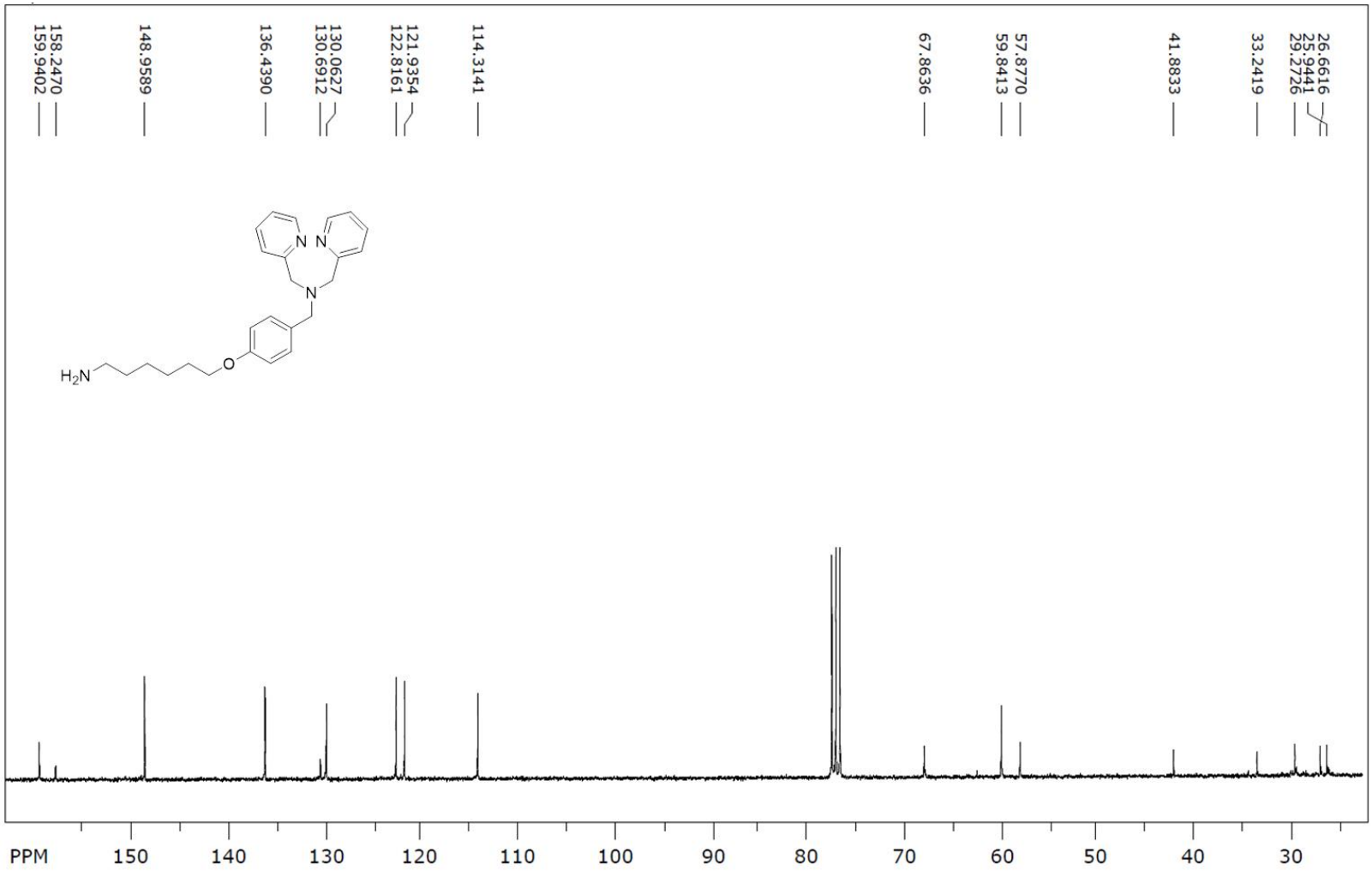

Figure S13. ^{13}C NMR spectrum of Ligand 1-NH_2, Related to Scheme 2.

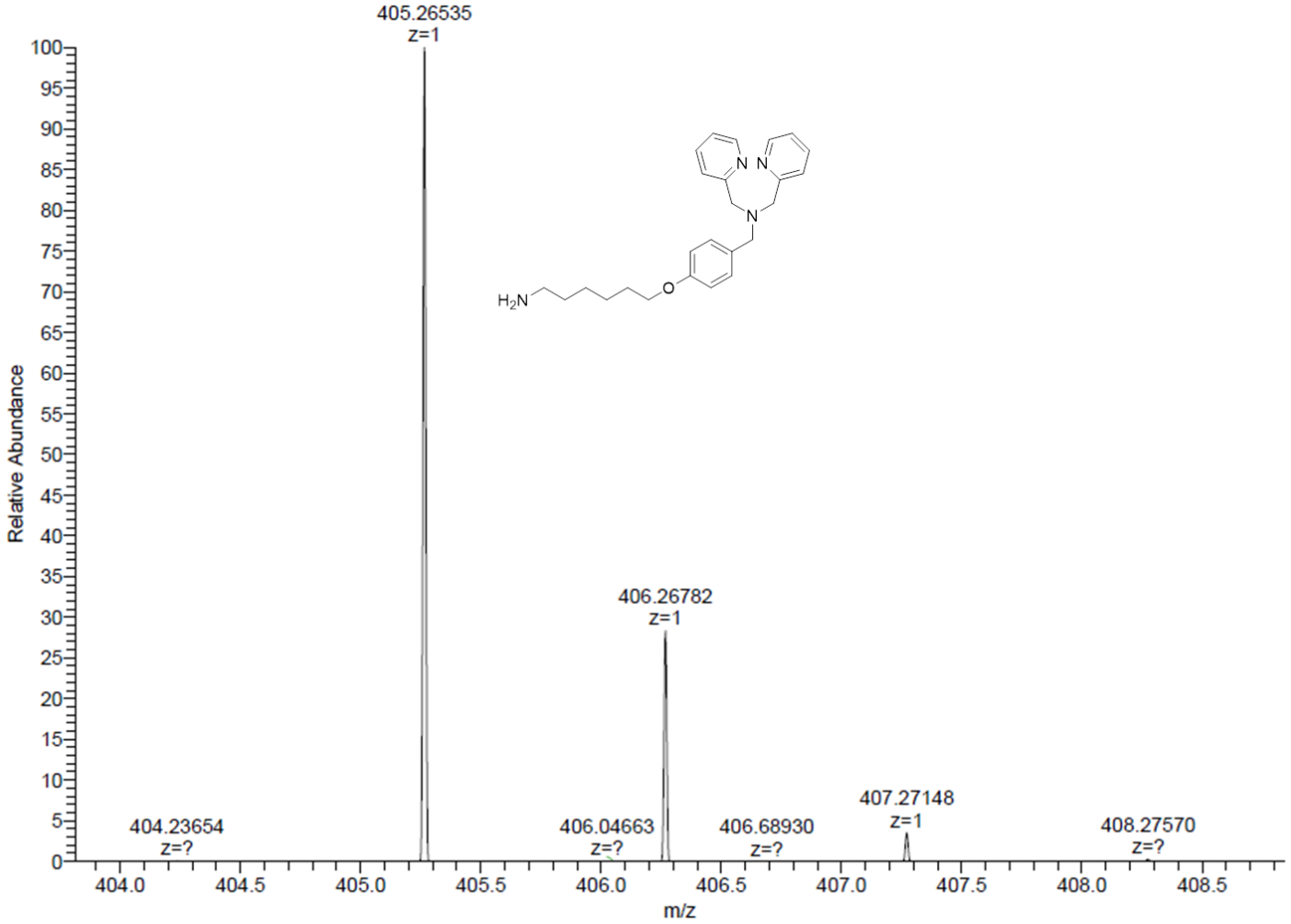

Figure S14. ESI-MS spectrum of Ligand 1-NH_2, Related to Scheme 2.

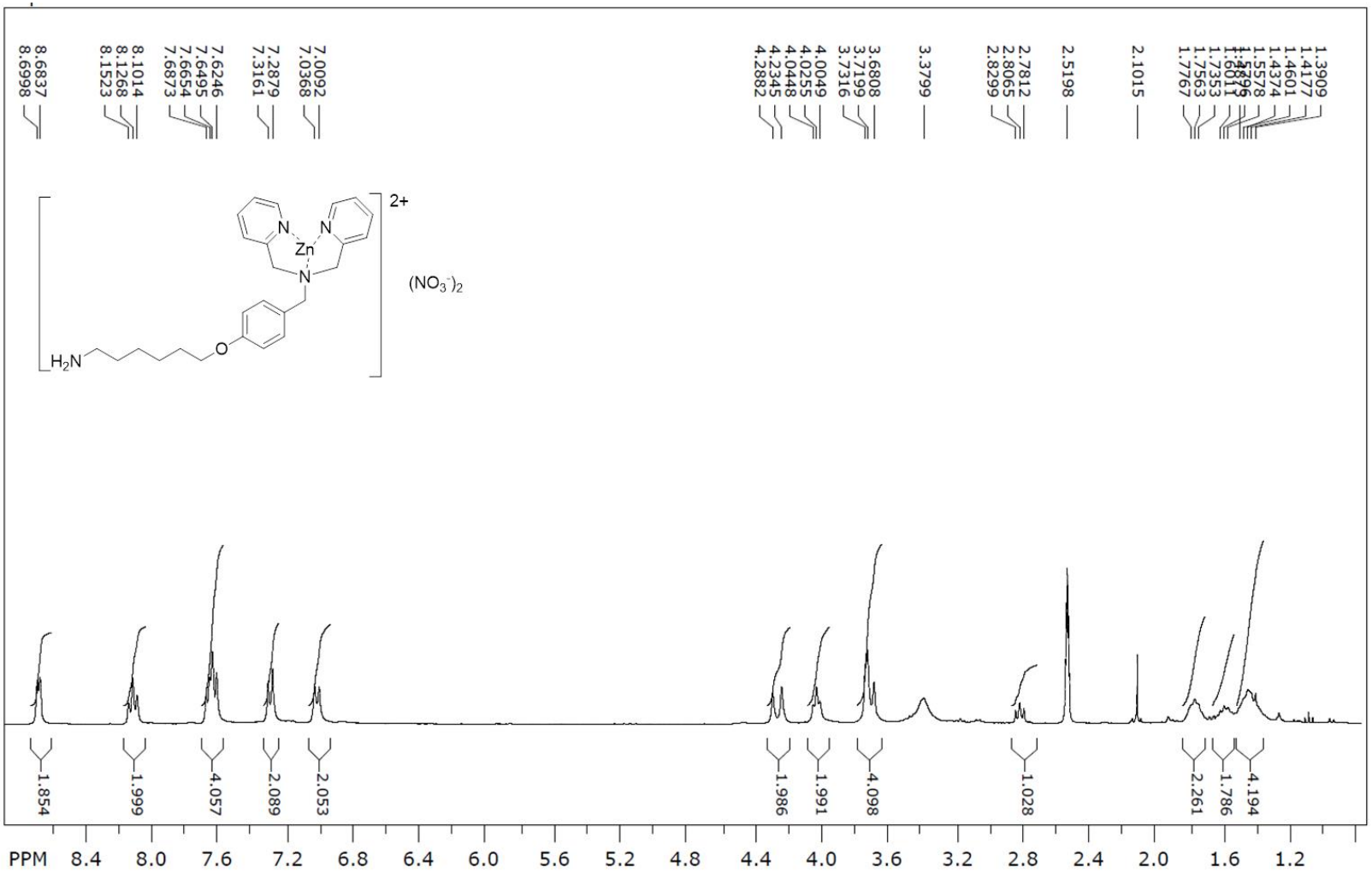

Figure S15. ^{1}H NMR spectrum of C1, Related to Scheme 2.

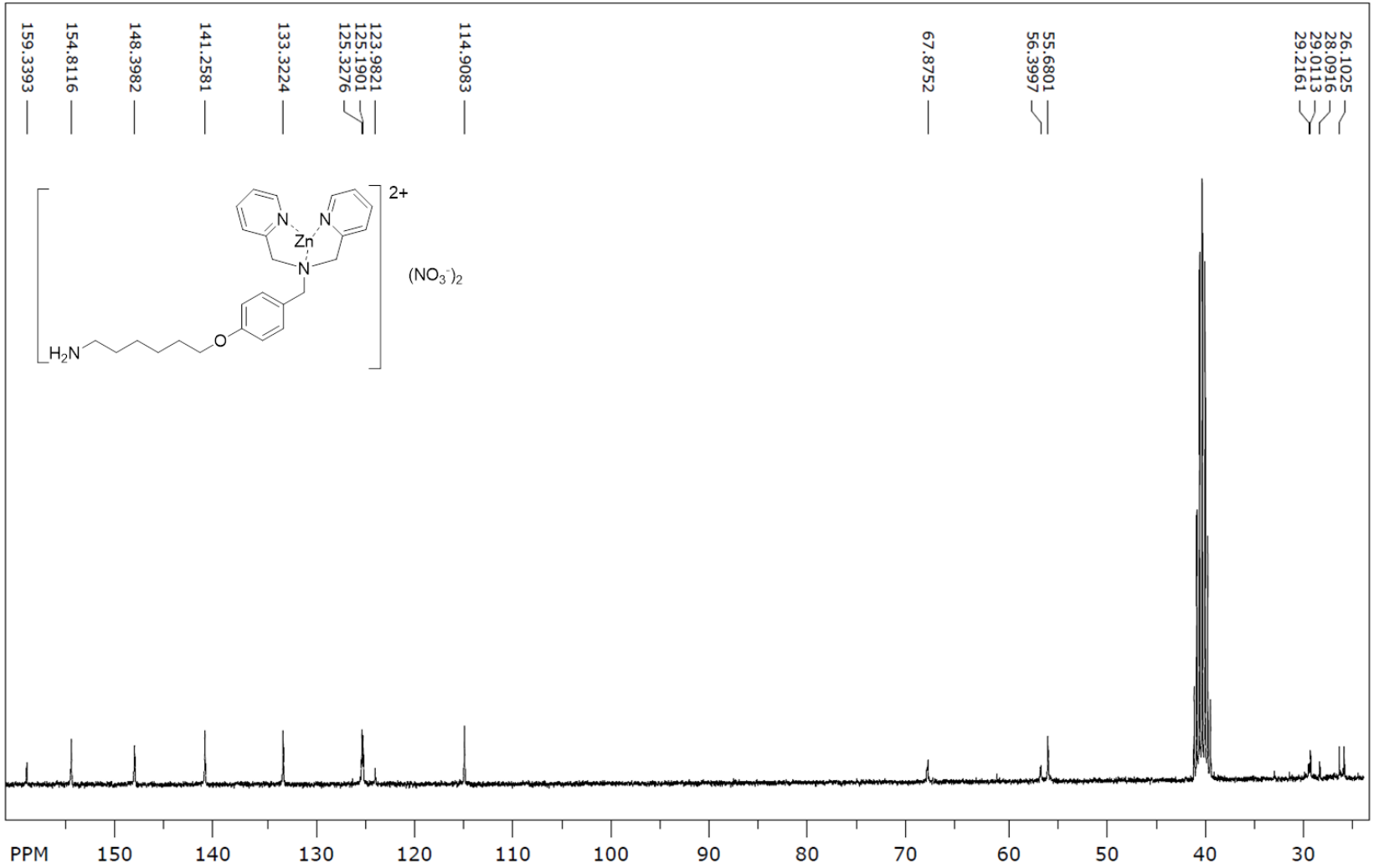

Figure S16. ^{13}C NMR spectrum of C1, Related to Scheme 2.

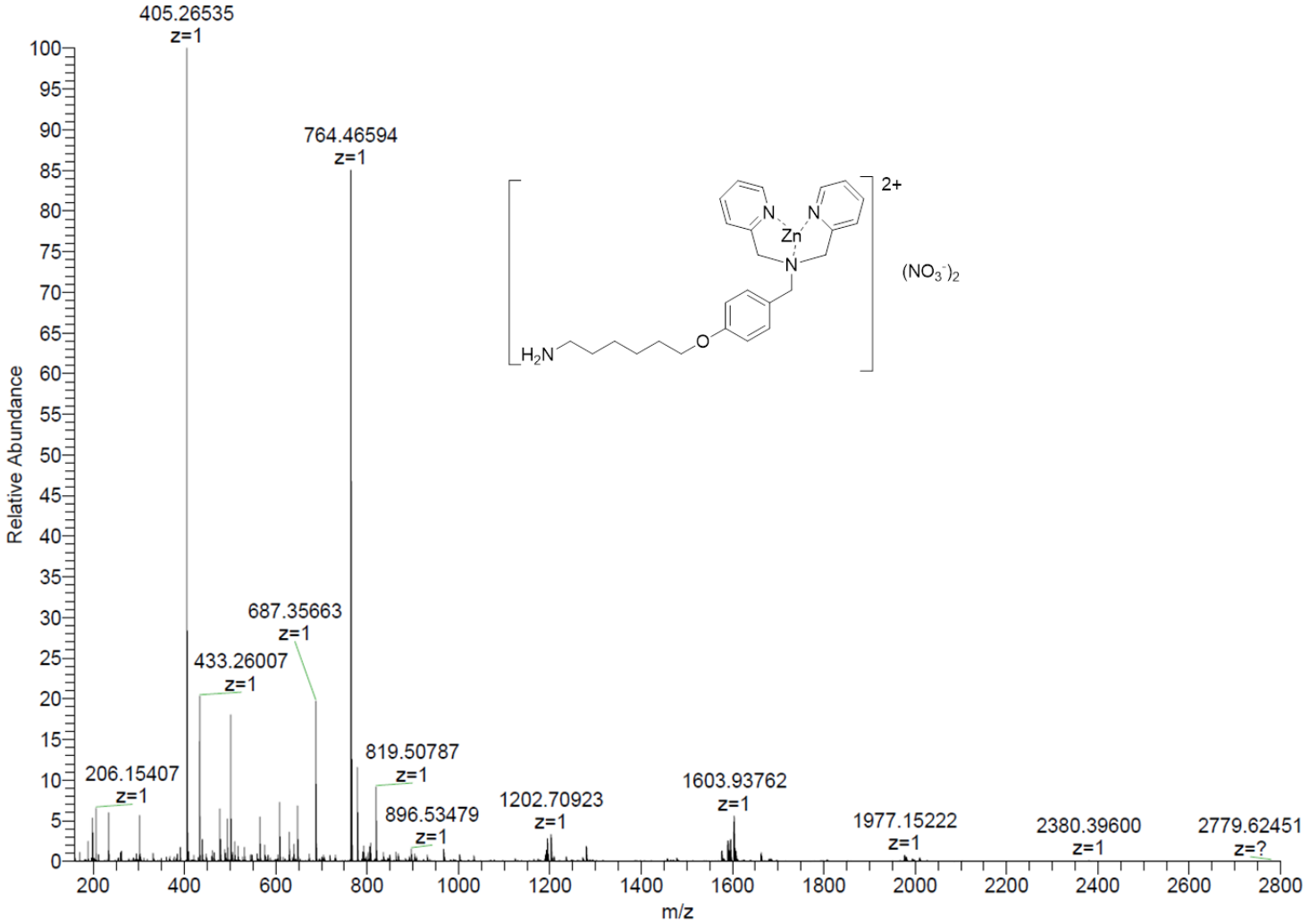

Figure S17. ESI-MS spectrum of C1, Related to Scheme 2.

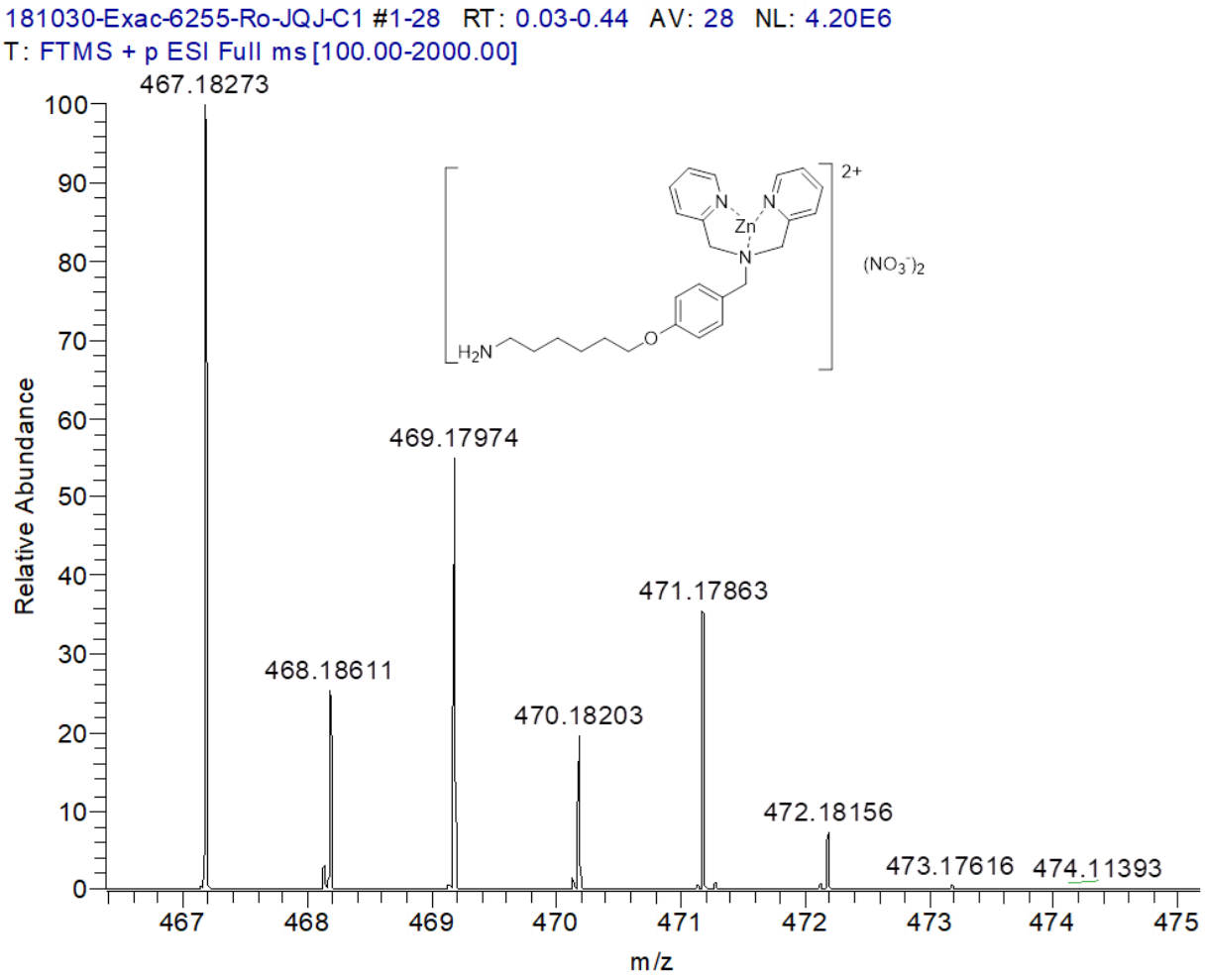

Figure S18. ESI-MS spectrum of C1, Related to Scheme 2.

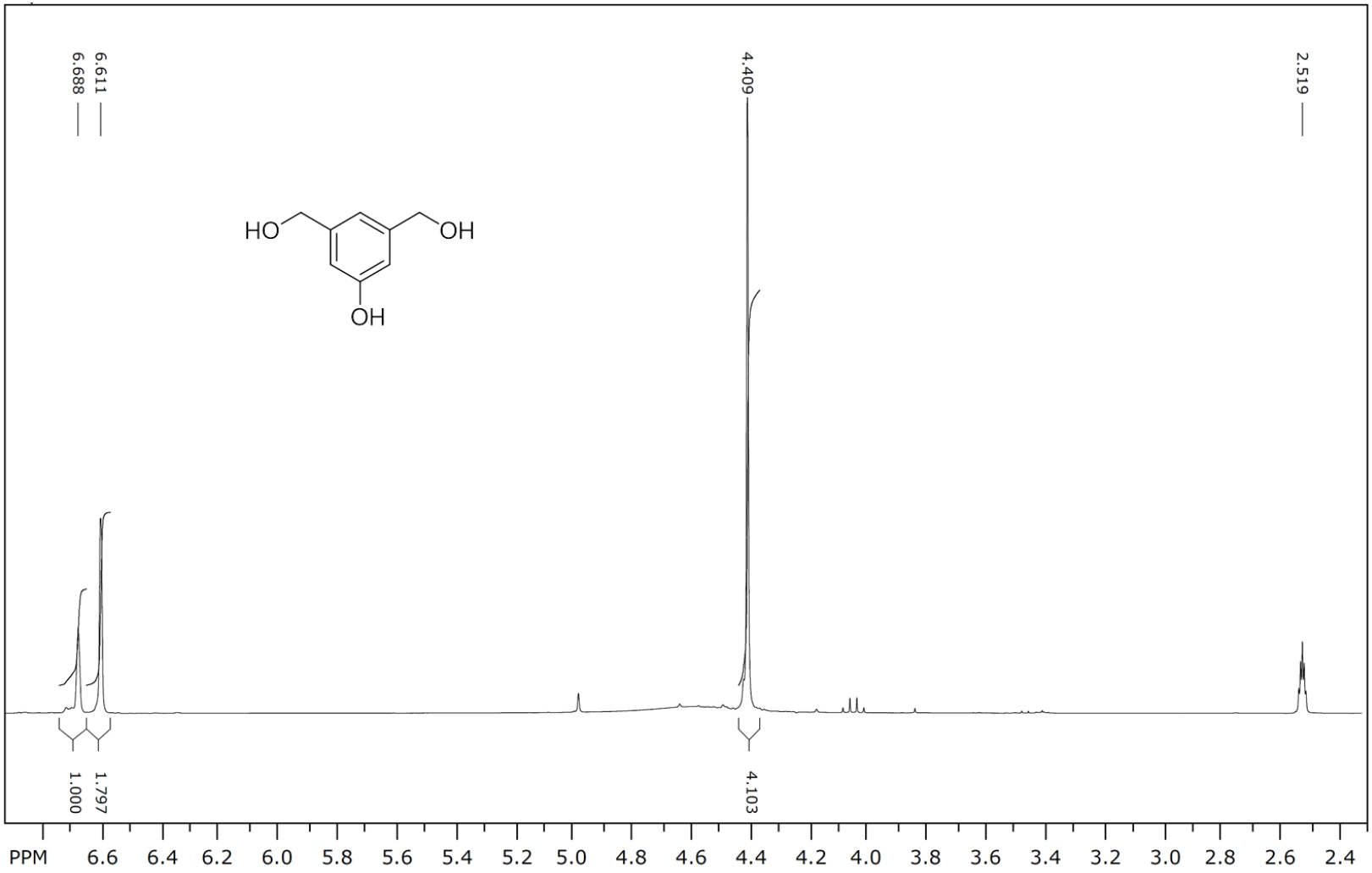

Figure S19. ^{1}H NMR spectrum of (5-hydroxy-1,3-phenylene)dimethanol, Related to Scheme 2.

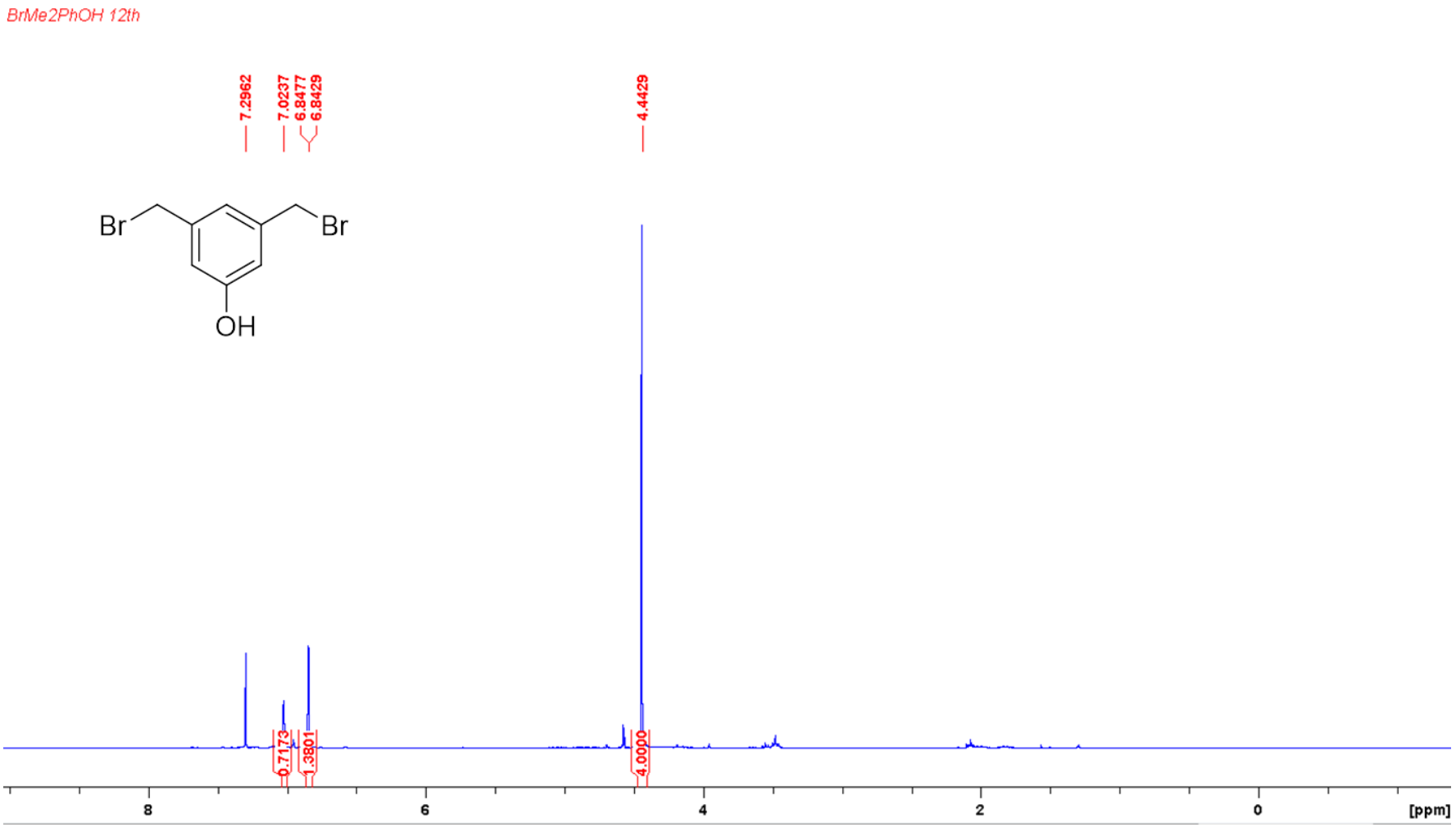

Figure S20. ^{1}H NMR spectrum of 3,5-bis(bromomethyl)phenol, Related to Scheme 2.

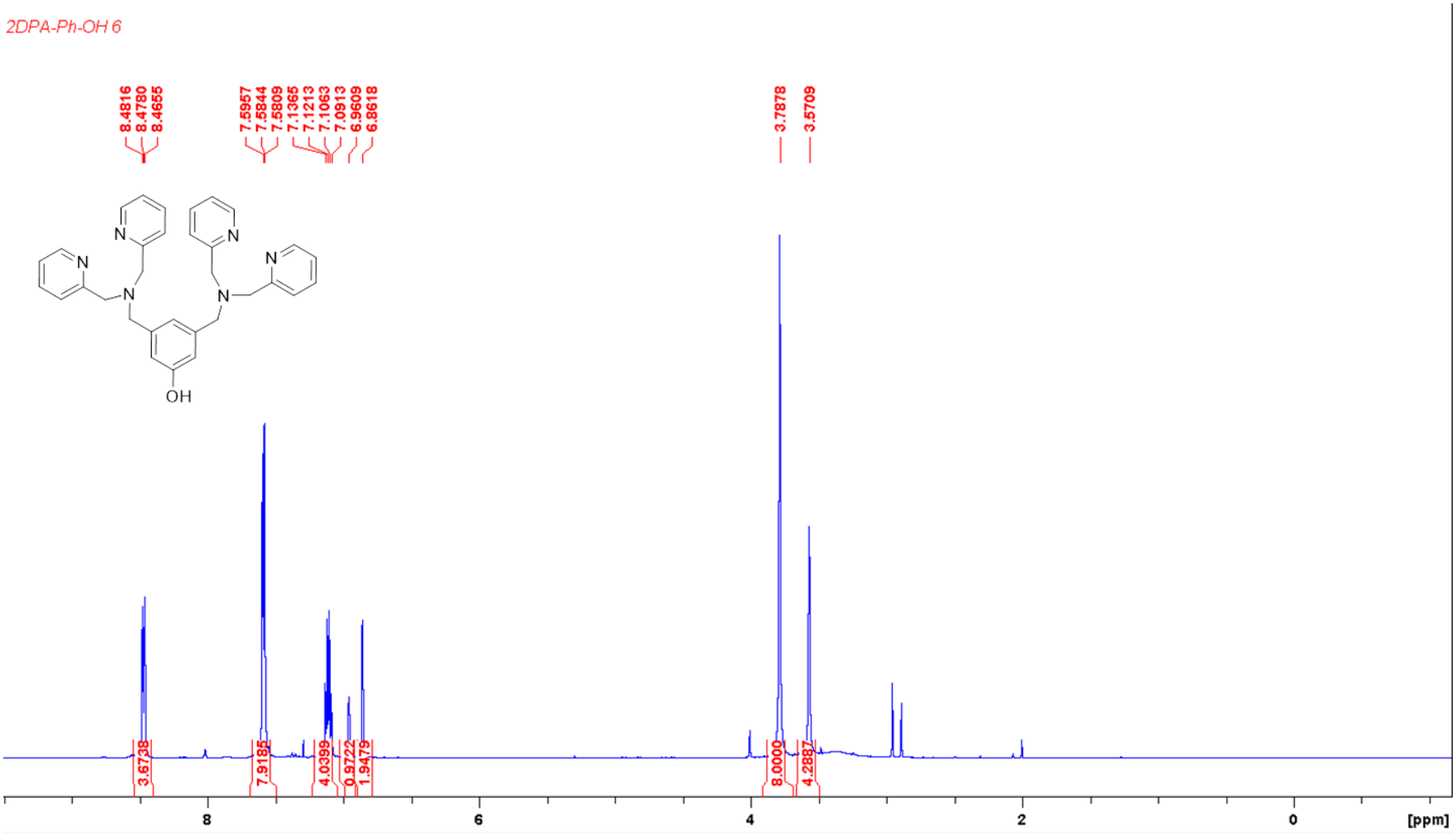

Figure S21. ^{1}H NMR spectrum of 2DPAOH , Related to Scheme 2.

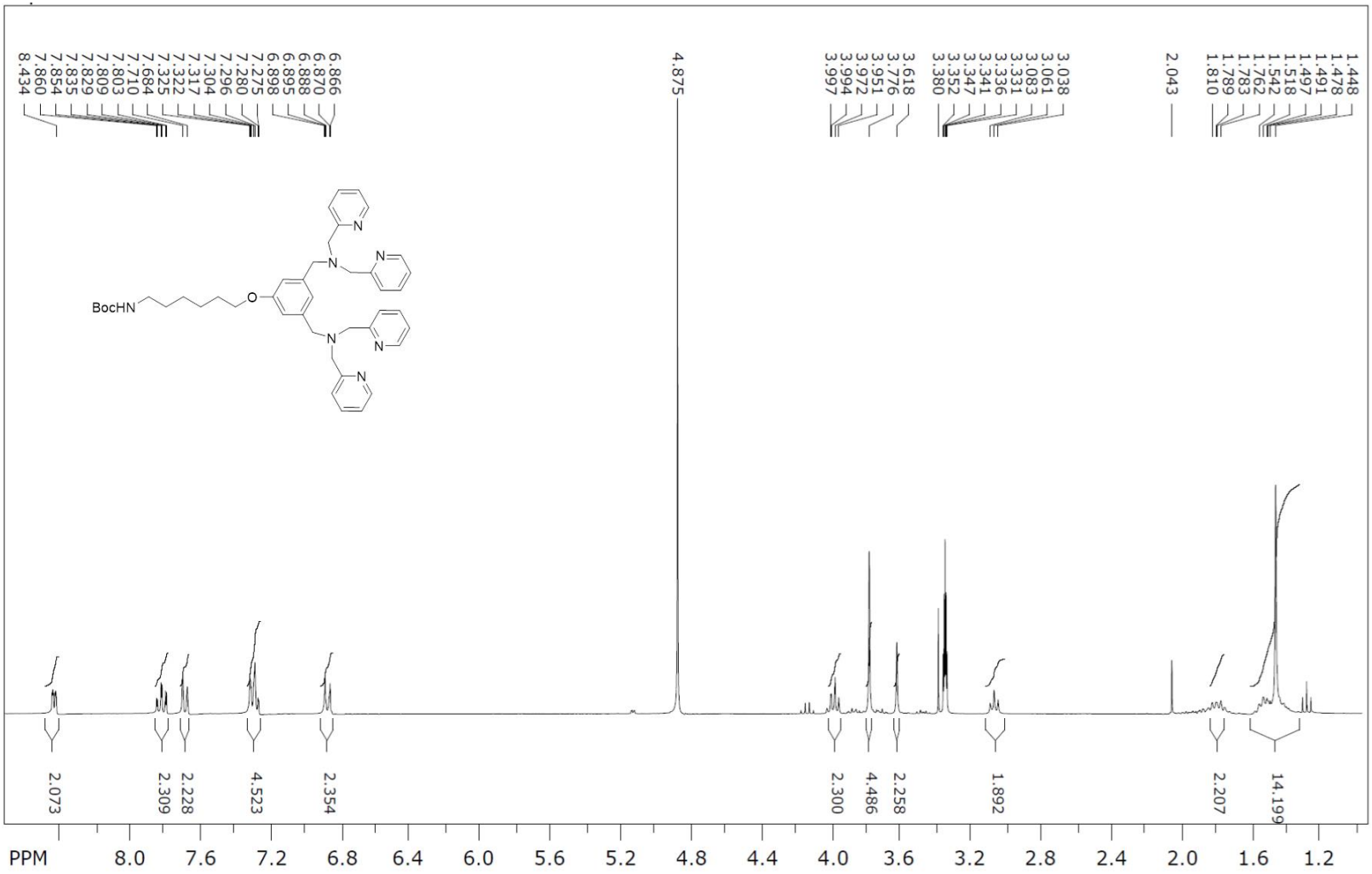

Figure S22. ^{1}H NMR spectrum of Ligand 2-Boc, Related to Scheme 2.

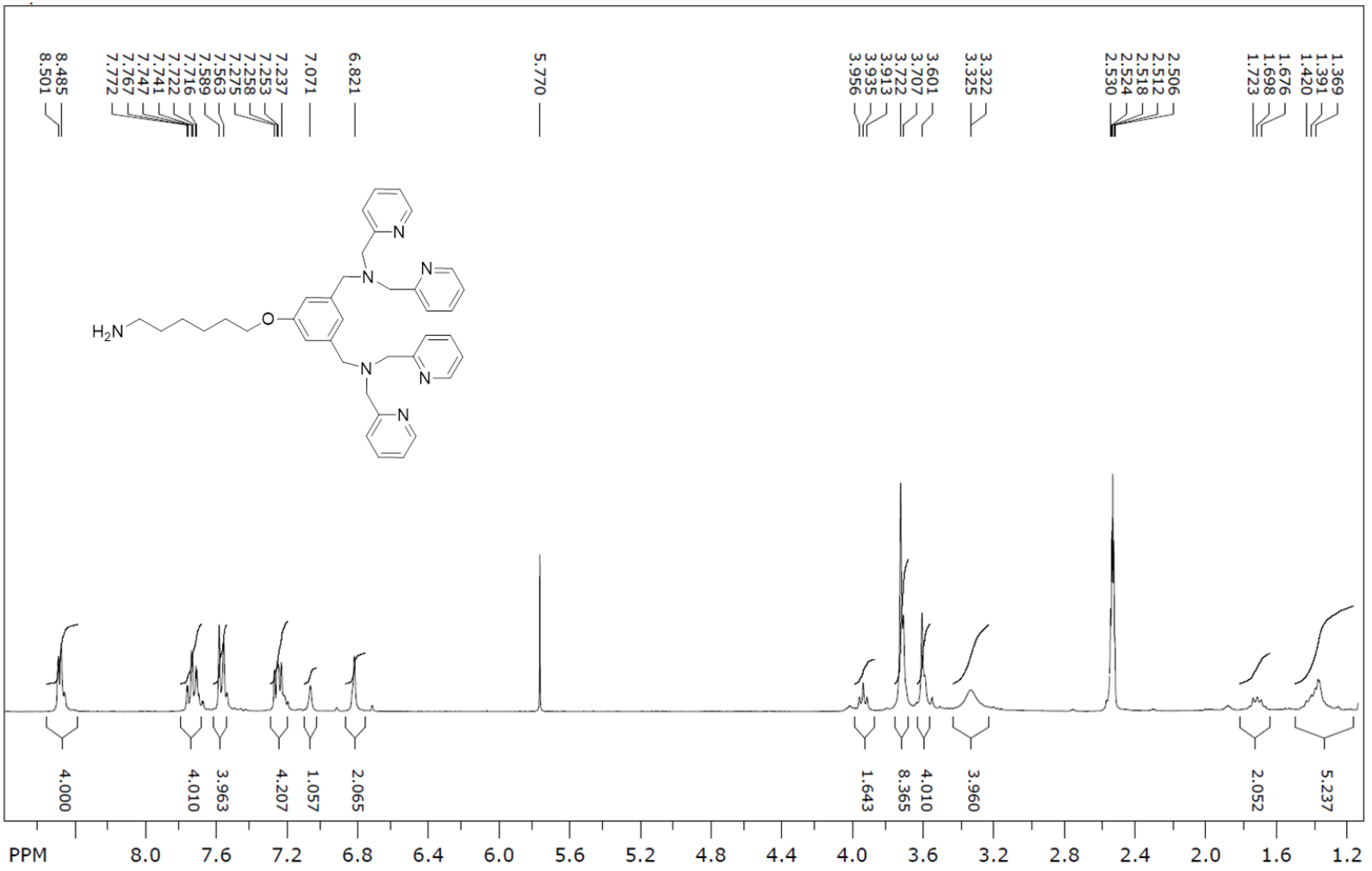

Figure S23. ^{1}H NMR spectrum of Ligand 2-$NH_{2,}$ Related to Scheme 2.

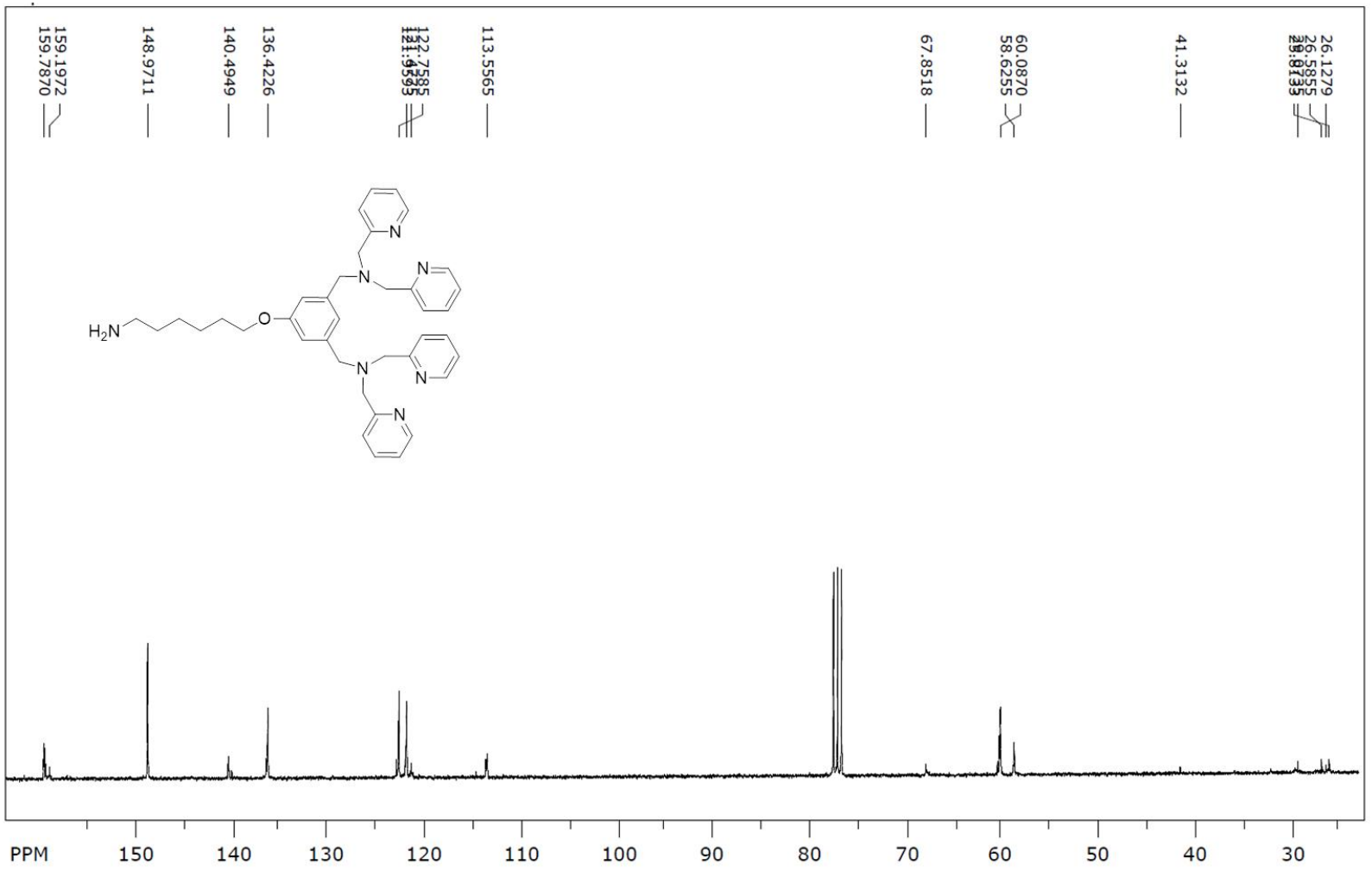

Figure S24. ^{13}C NMR spectrum of Ligand 2-NH_2, Related to Scheme 2.

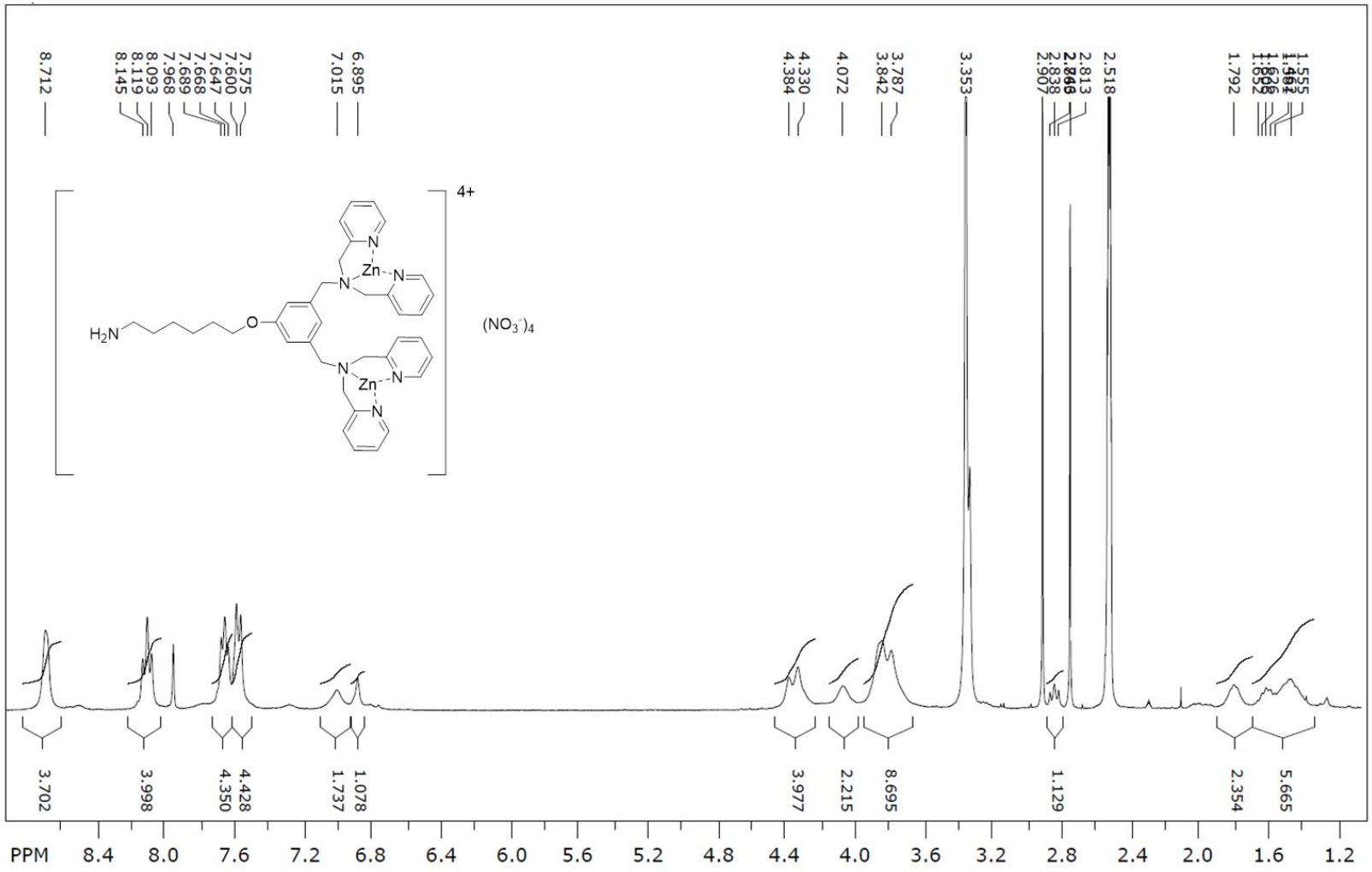

Figure S25. ^{1}H NMR spectrum of C2, Related to Scheme 2.

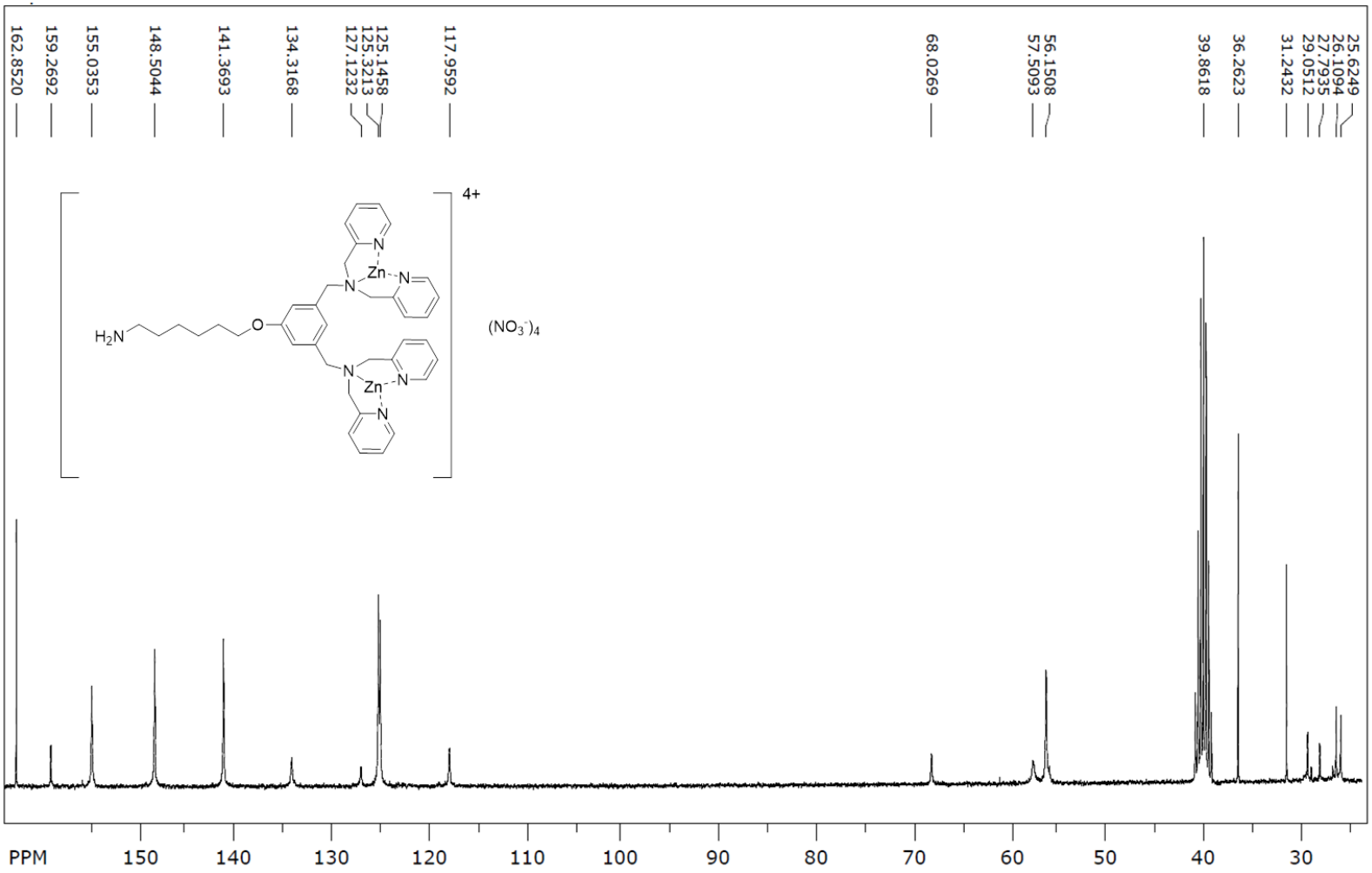

Figure S26. ^{13}C NMR spectrum of C2, Related to Scheme 2.

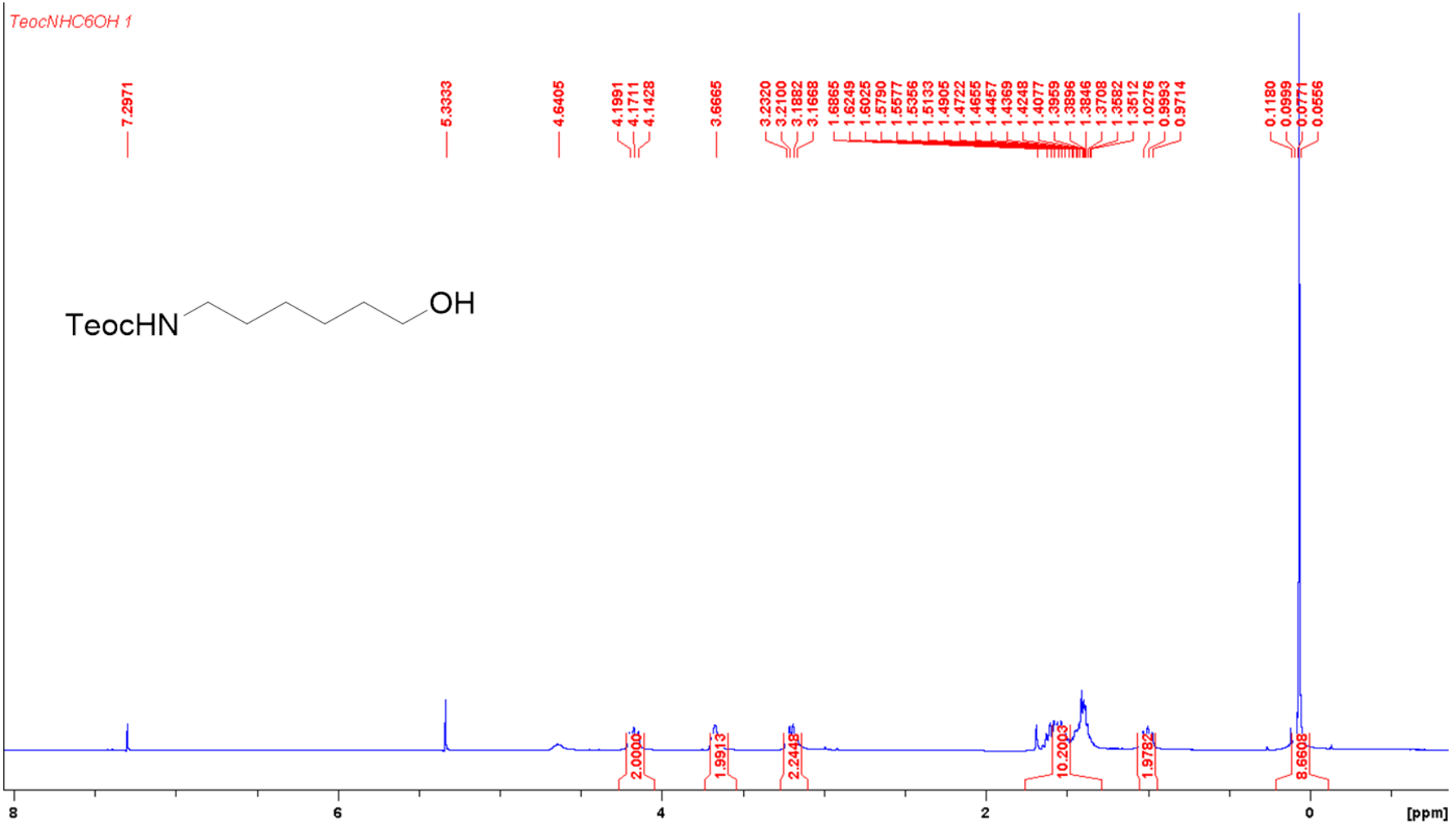

Figure S27. ^{1}H NMR spectrum of 2-(trimethylsilyl)ethyl (6-hydroxyhexyl)carbamate, Related to Scheme 2.

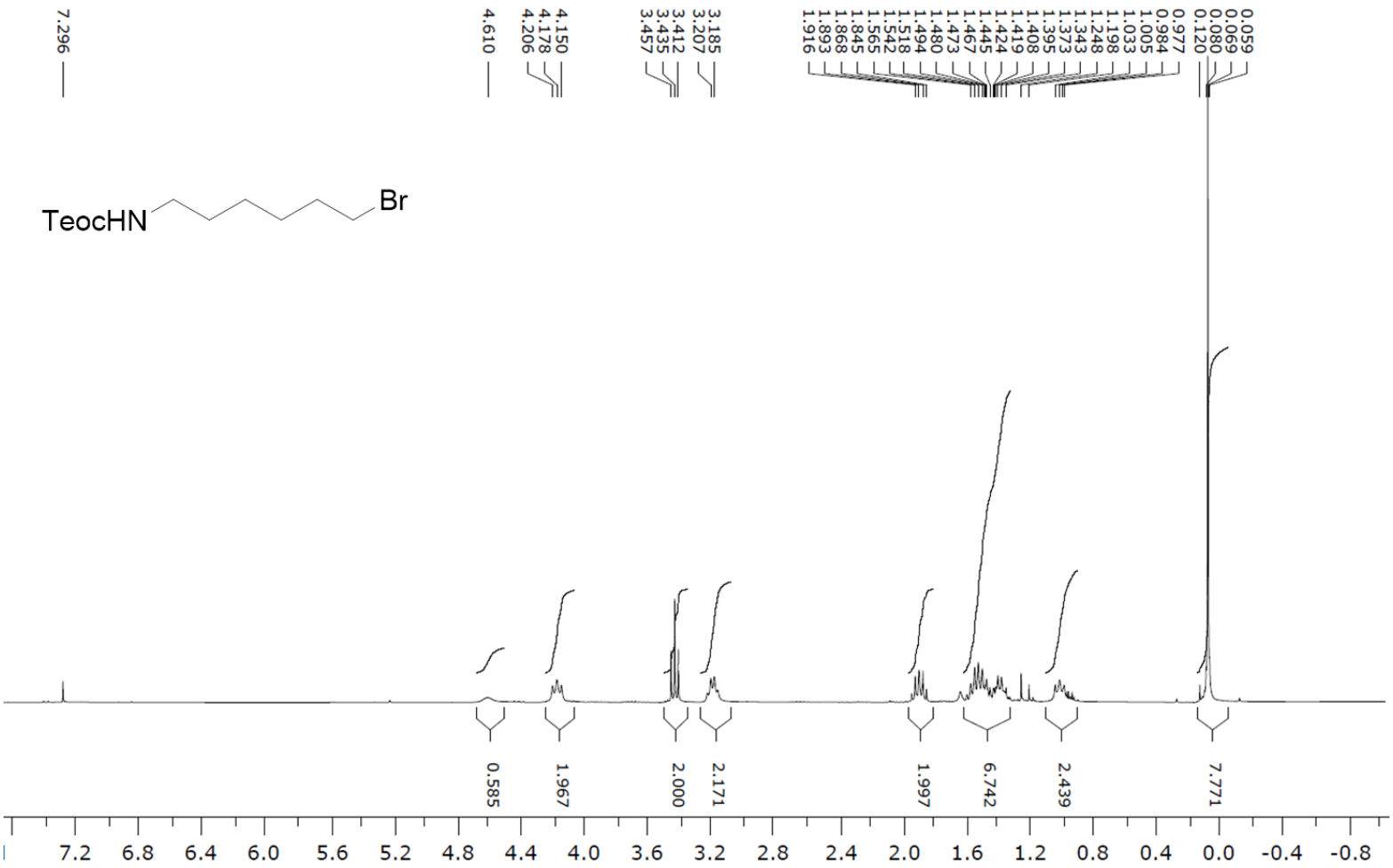

Figure S28. ^{1}H NMR spectrum of 2-(trimethylsilyl)ethyl (6-bromoxyhexyl)carbamate Related to Scheme 2.

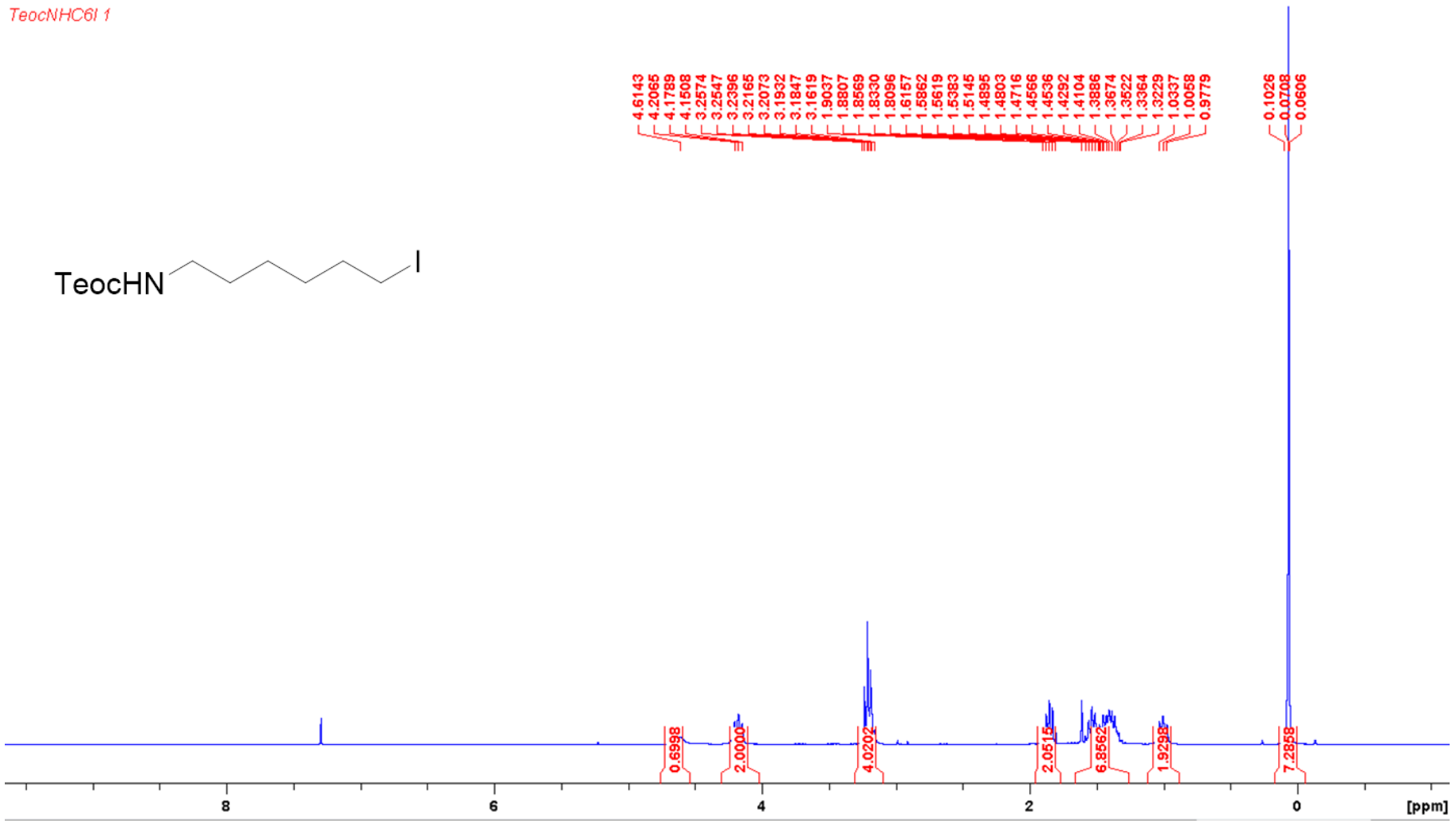

Figure S29. ^{1}H NMR spectrum of 2-(trimethylsilyl)ethyl (6-iodohexyl)carbamate Related to Scheme 2.

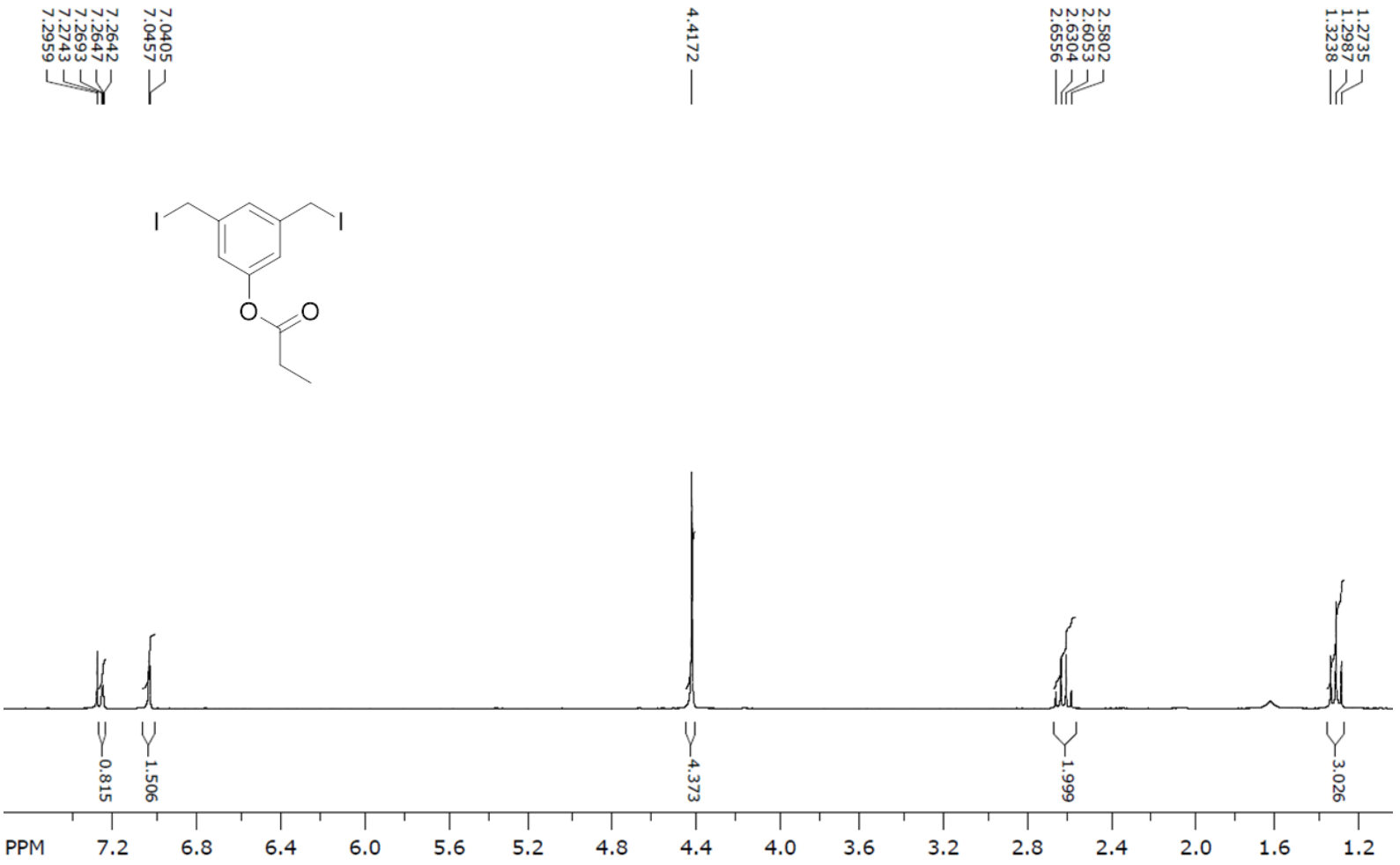

Figure S30. ^{1}H NMR spectrum of 3,5-bis(iodomethyl)phenyl propionate Related to Scheme 2.

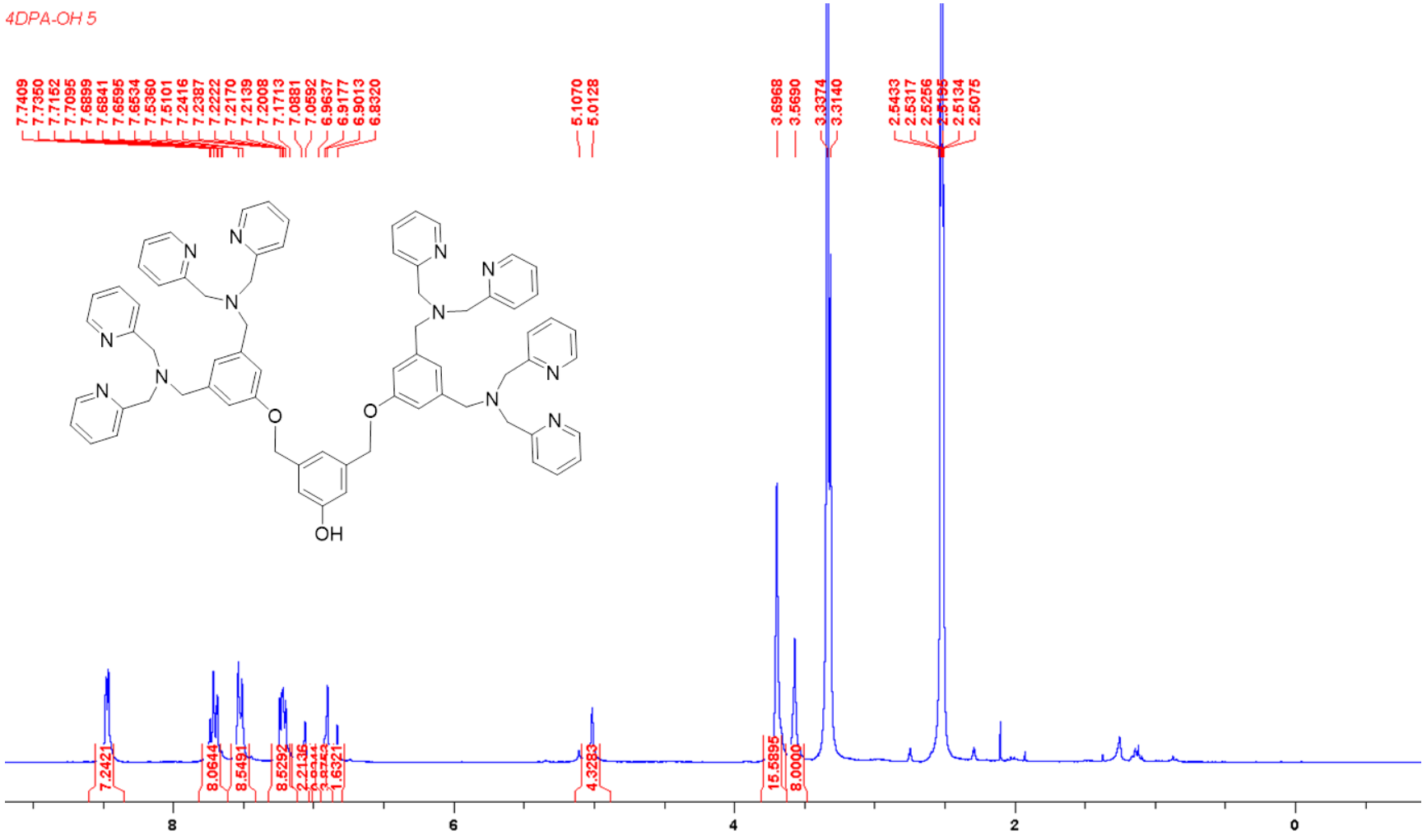

Figure S31. ^{1}H NMR spectrum of 4DPAOH Related to Scheme 2.

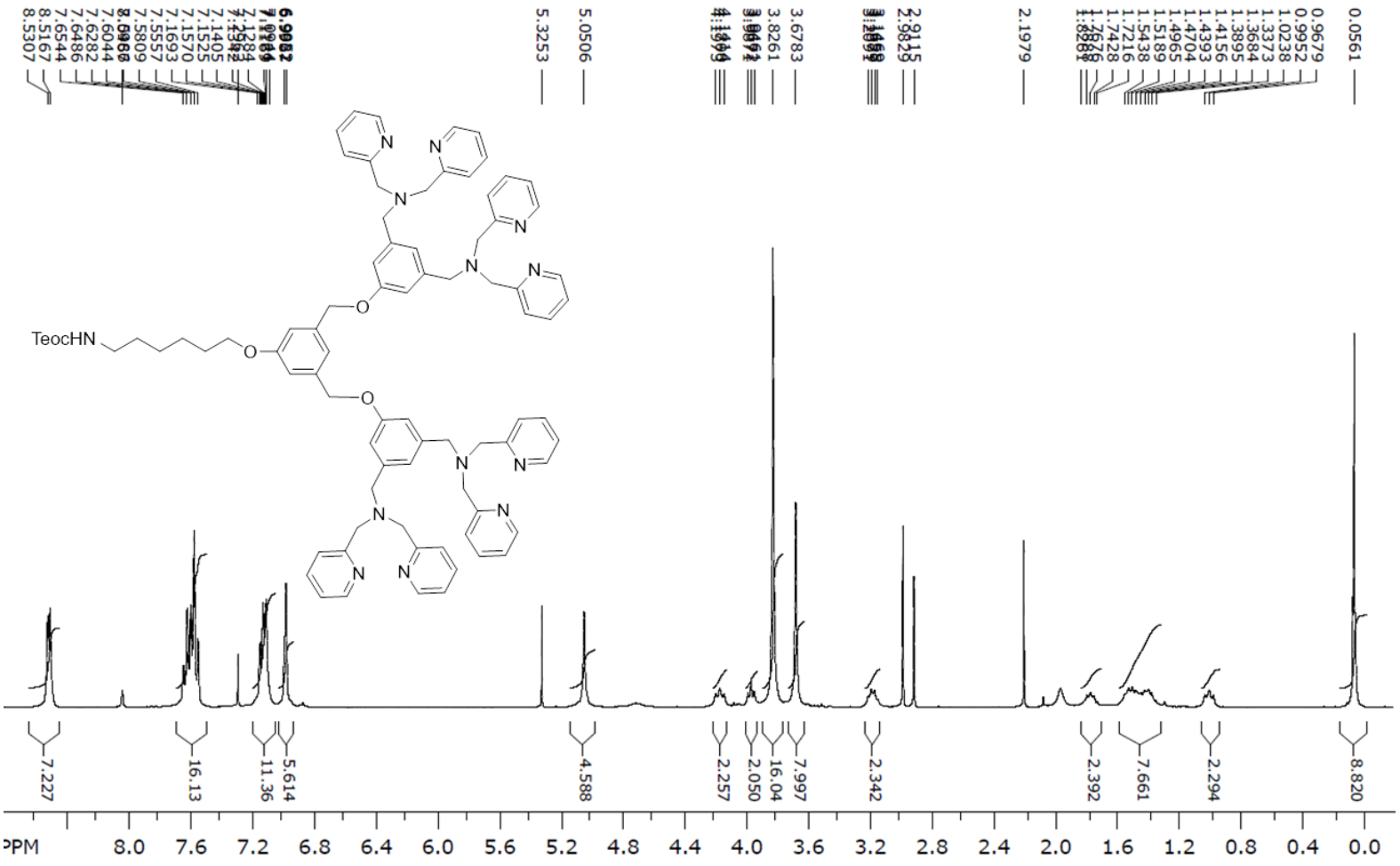

Figure S32. ^{1}H NMR spectrum of Ligand 4-Teoc Related to Scheme 2.

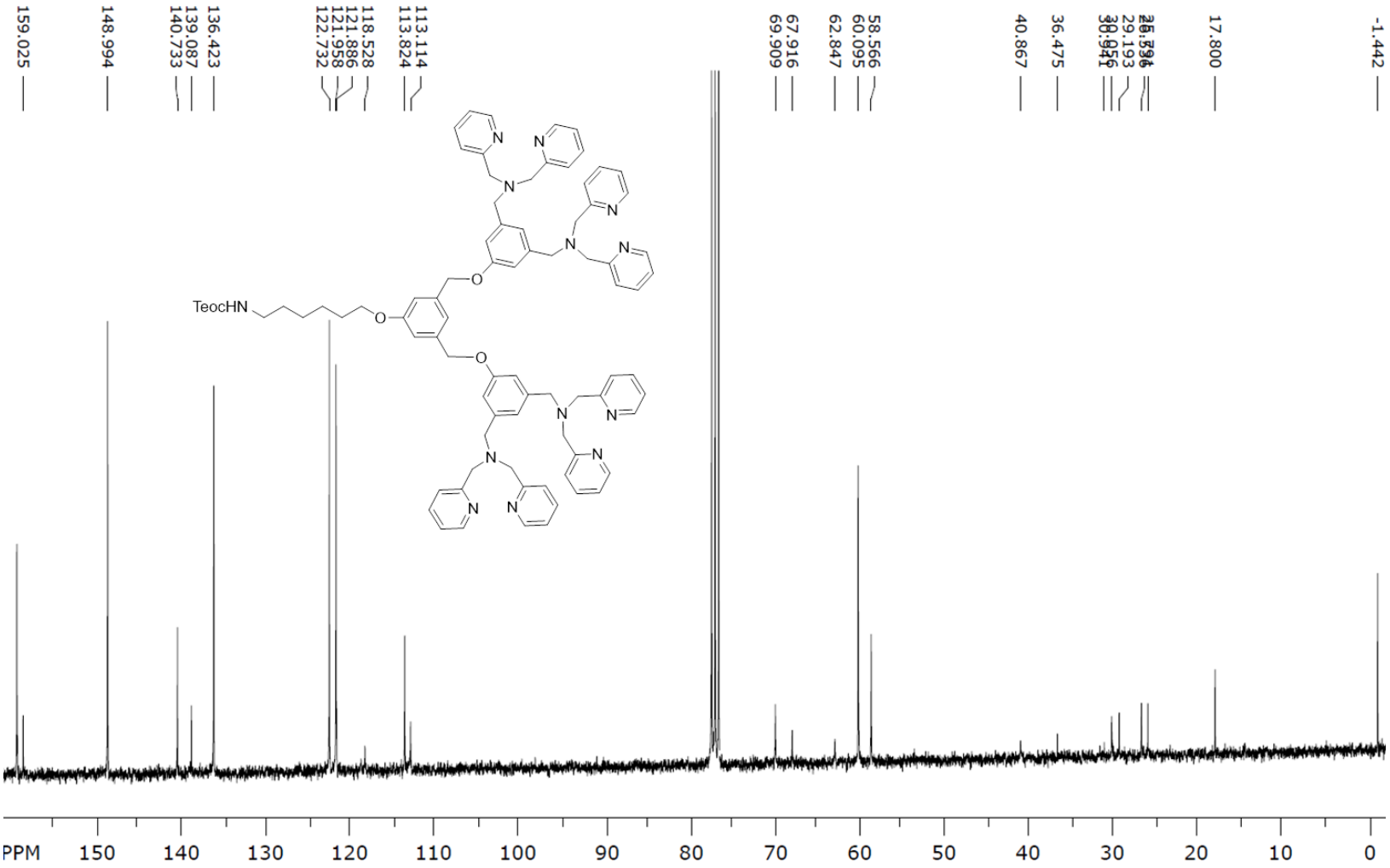

Figure S33. ^{13}C NMR spectrum of Ligand 4-Teoc Related to Scheme 2.

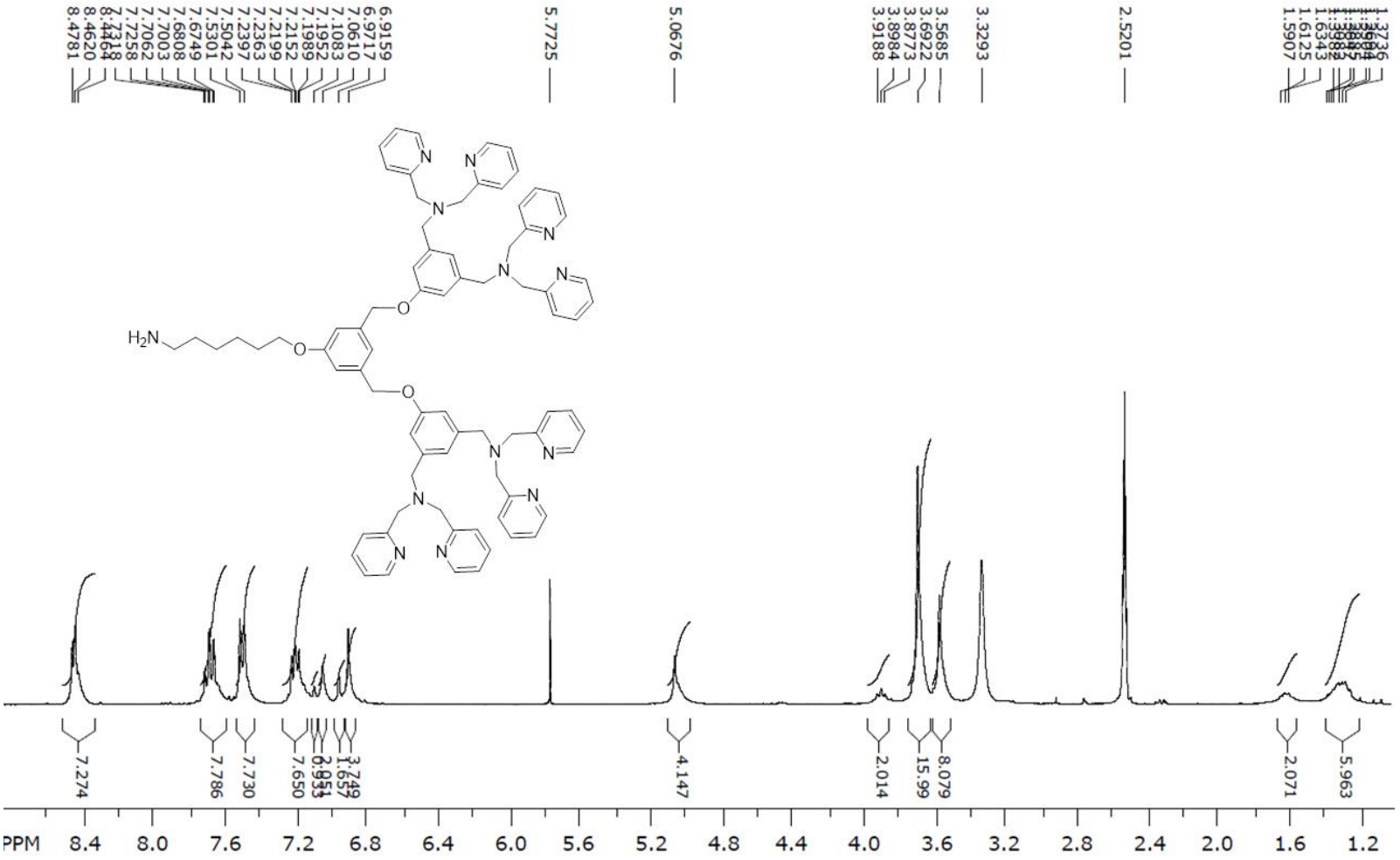

Figure S34. ^{1}H NMR spectrum of Ligand 4-$NH_{2,}$ Related to Scheme 2.

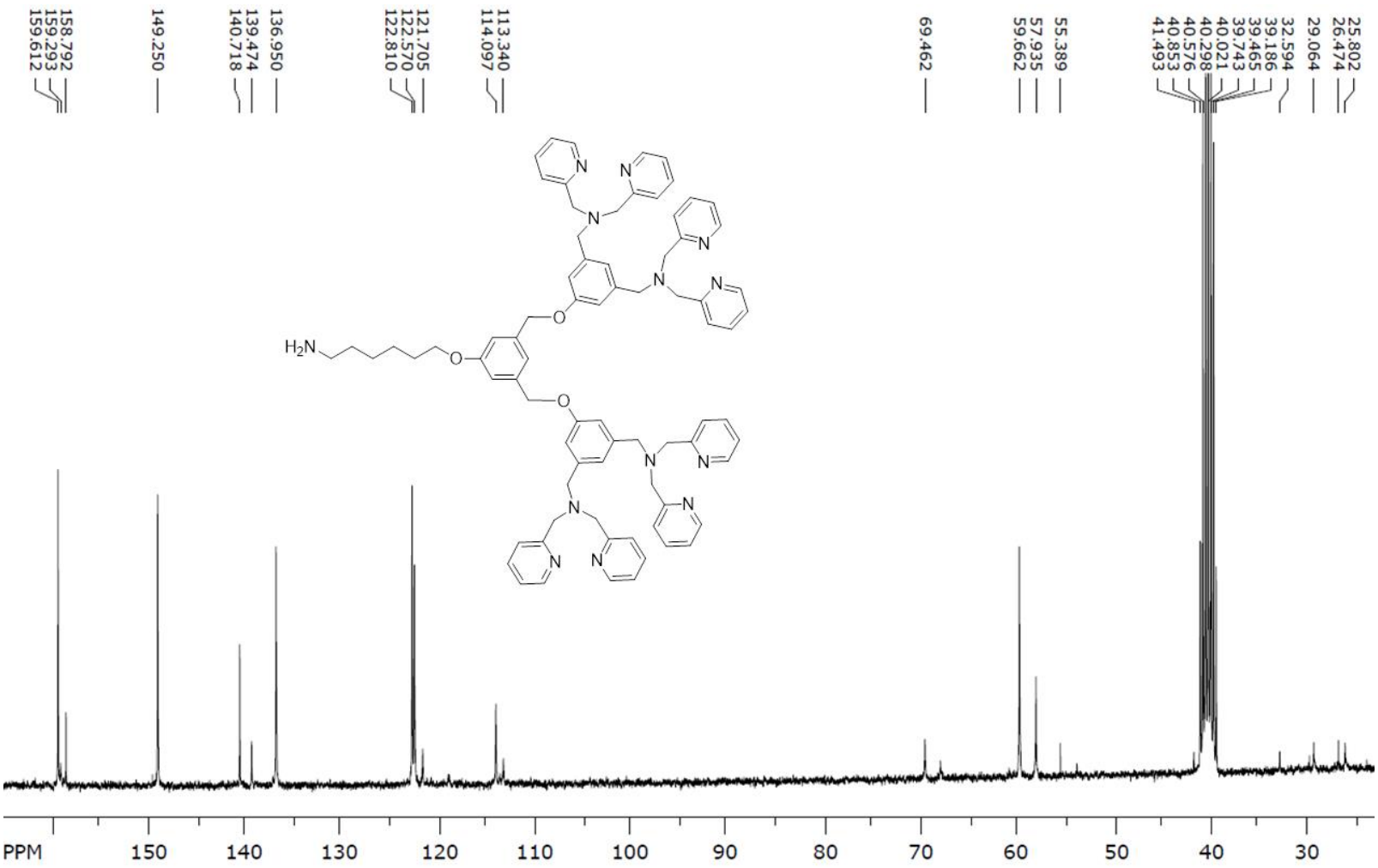

Figure S35. ^{13}C NMR spectrum of Ligand 4-NH_2, Related to Scheme 2.

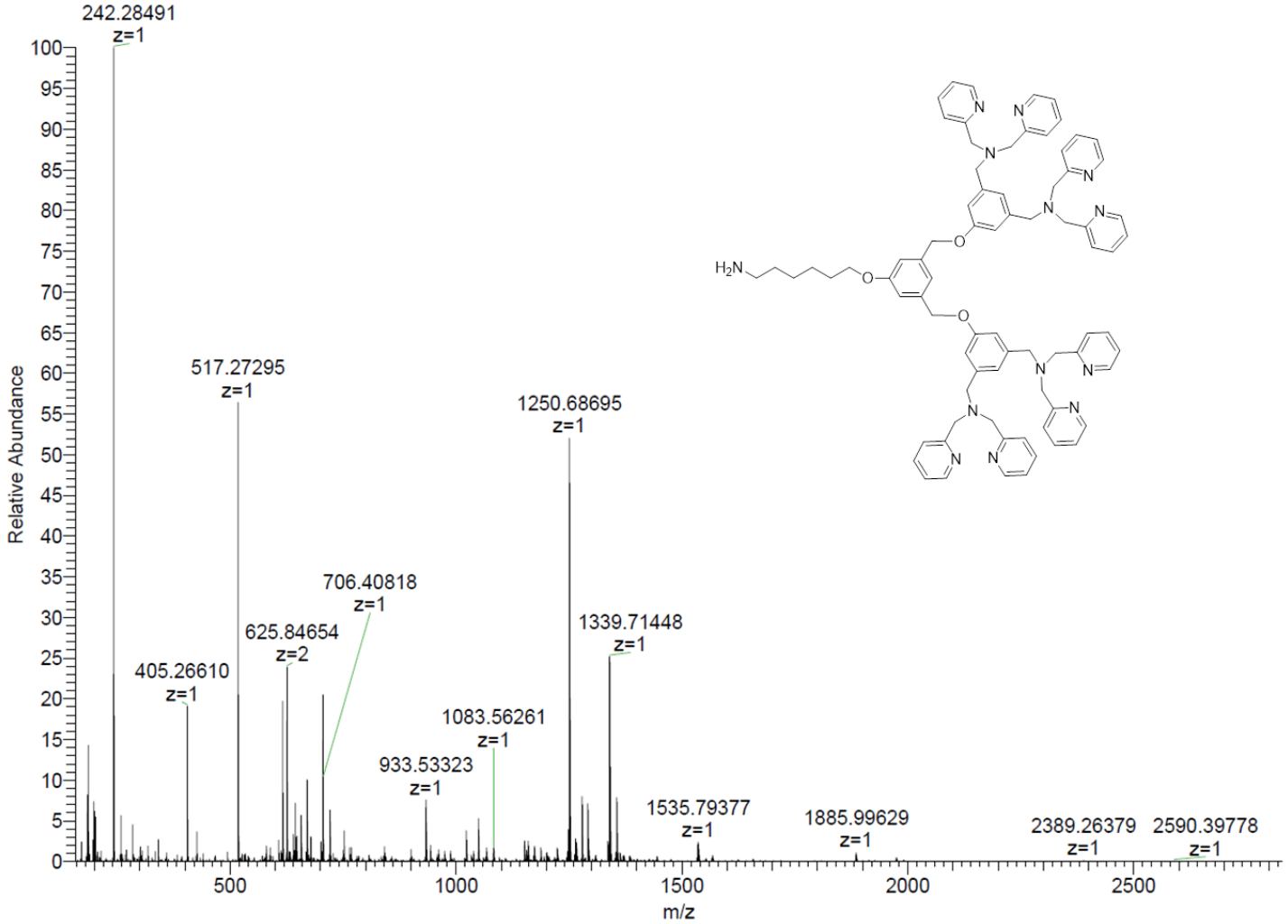

Figure S36. ESI-MS spectrum of Ligand 4-NH_2, Related to Scheme 2.

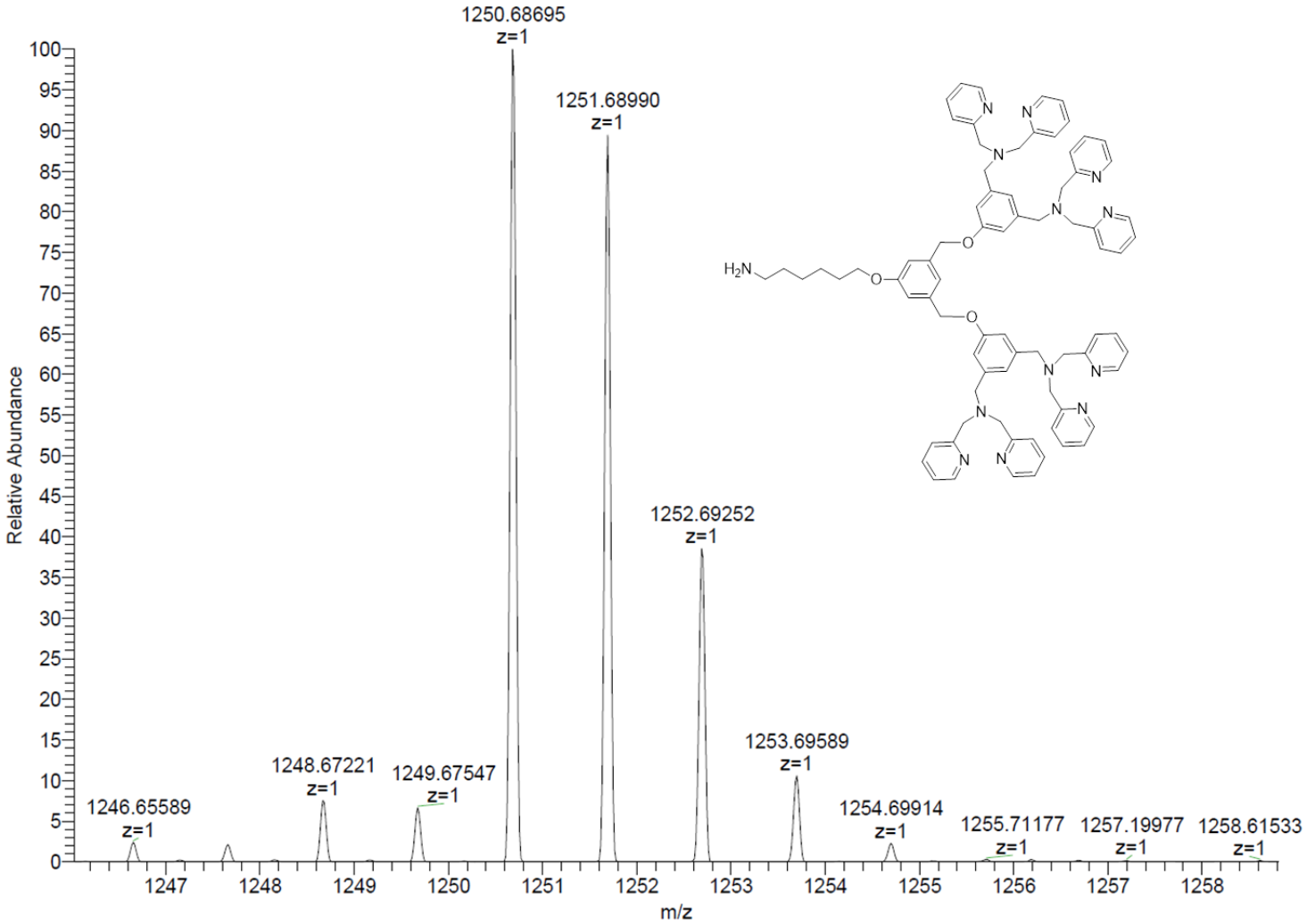

Figure S37. ESI-MS spectrum of Ligand 4-NH_2, Related to Scheme 2.

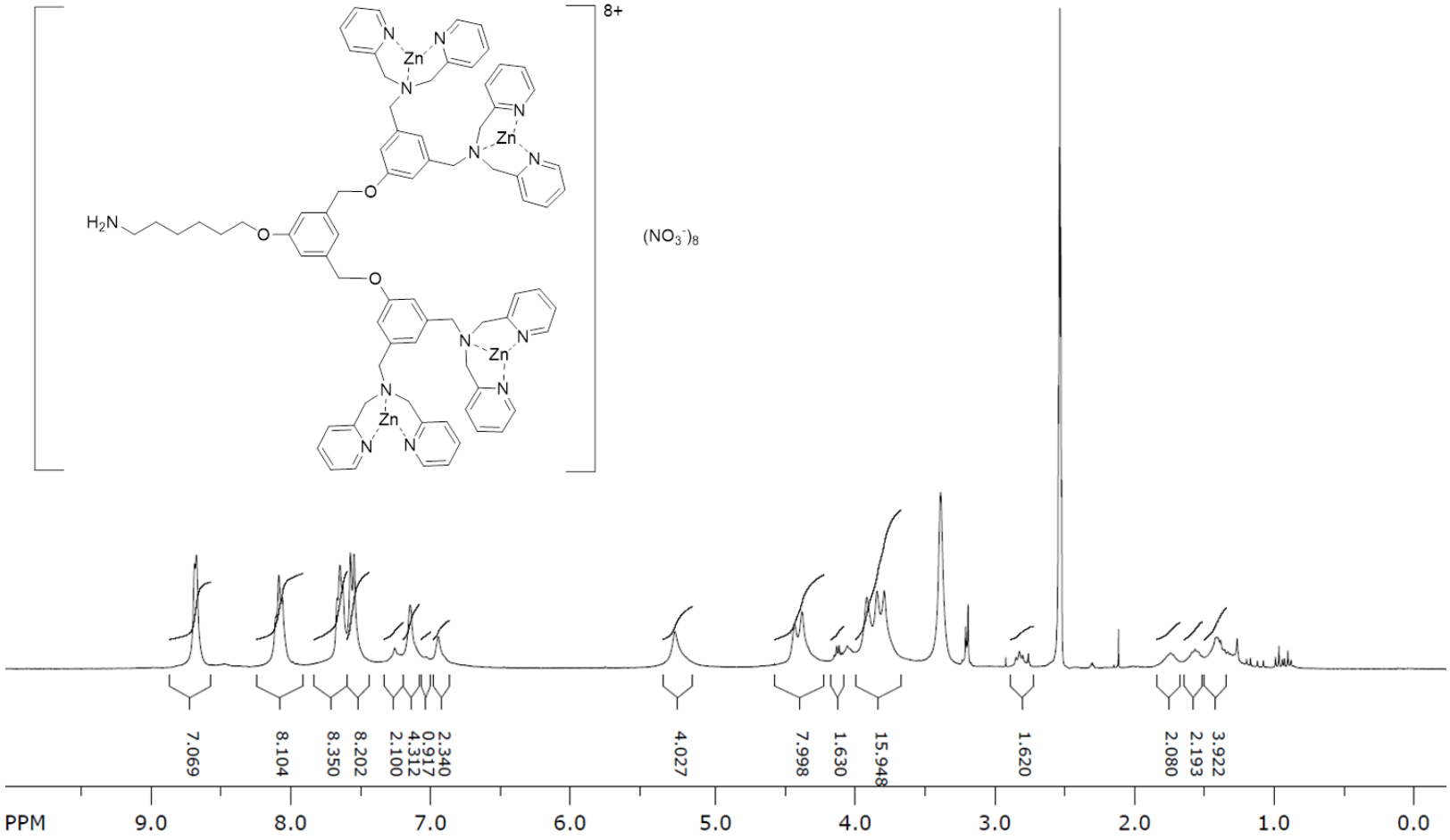

27) Figure S38. ^{1}H NMR spectrum of C4, Related to Scheme 2.

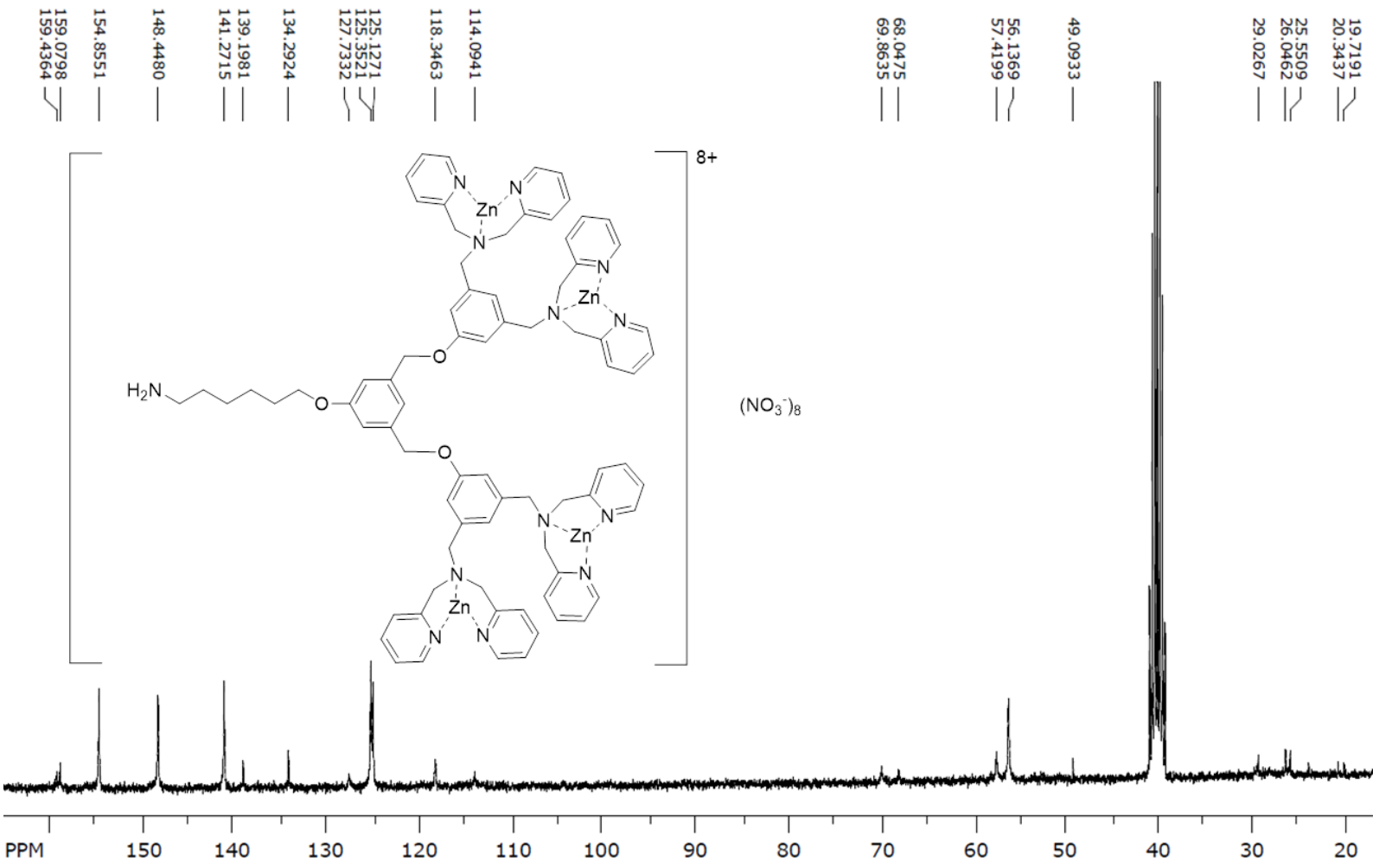

28) Figure S39. ^{13}C NMR spectrum of C4, Related to Scheme 2.

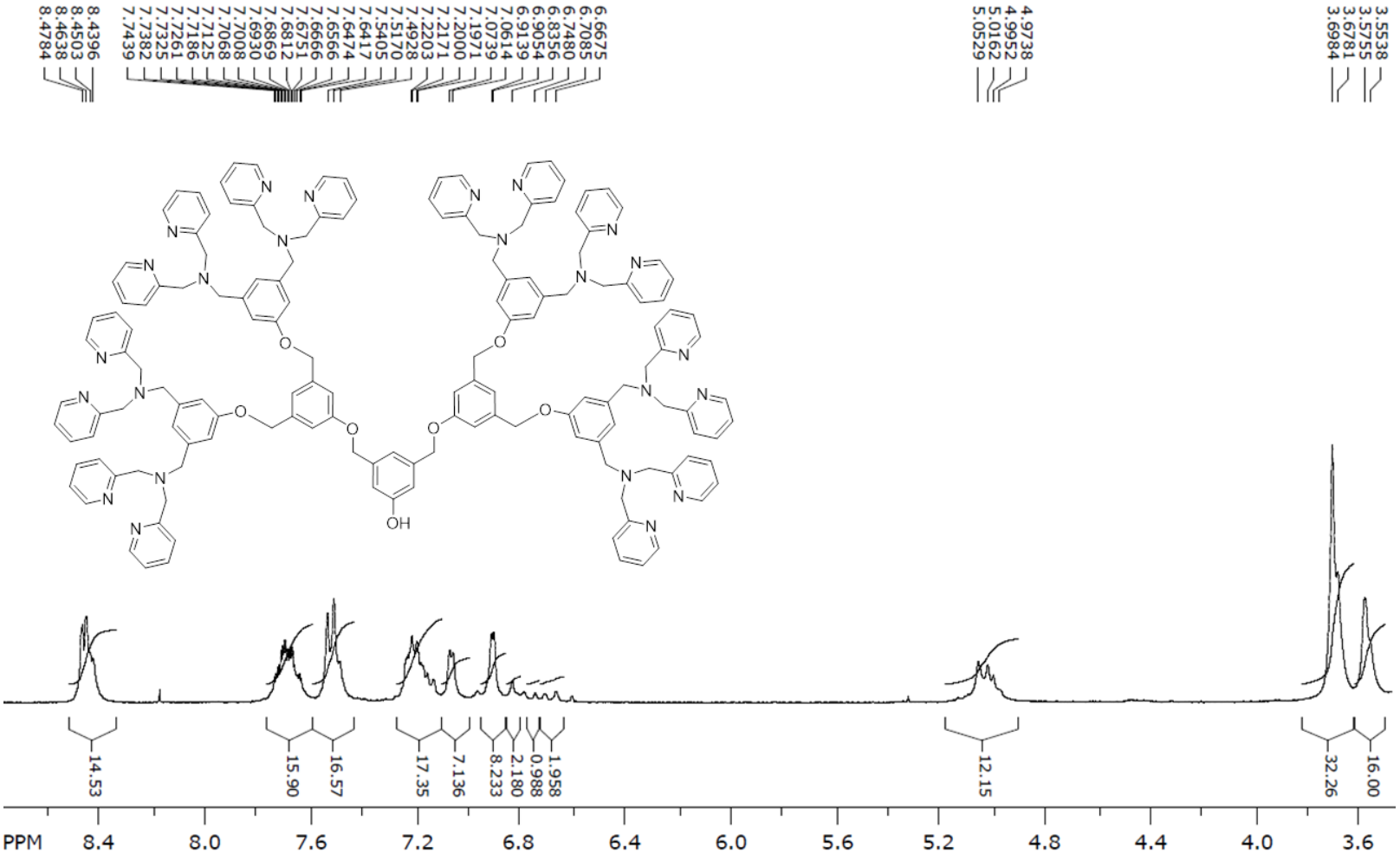

Figure S40. ^{1}H NMR spectrum of 8DPAOH , Related to Scheme 2.

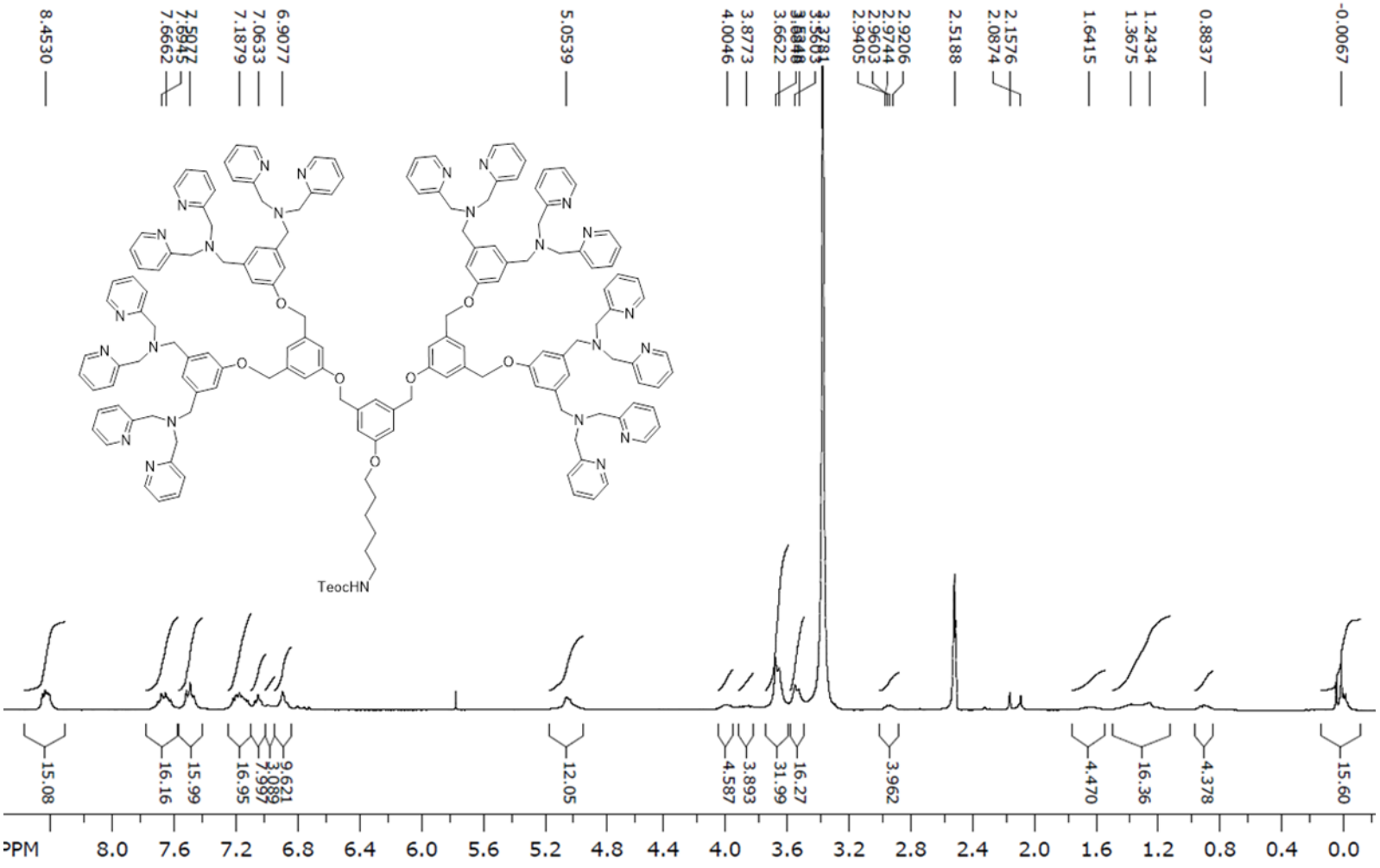

Figure S41. ^{1}H NMR spectrum of Ligand 8-Teoc, Related to Scheme 2.

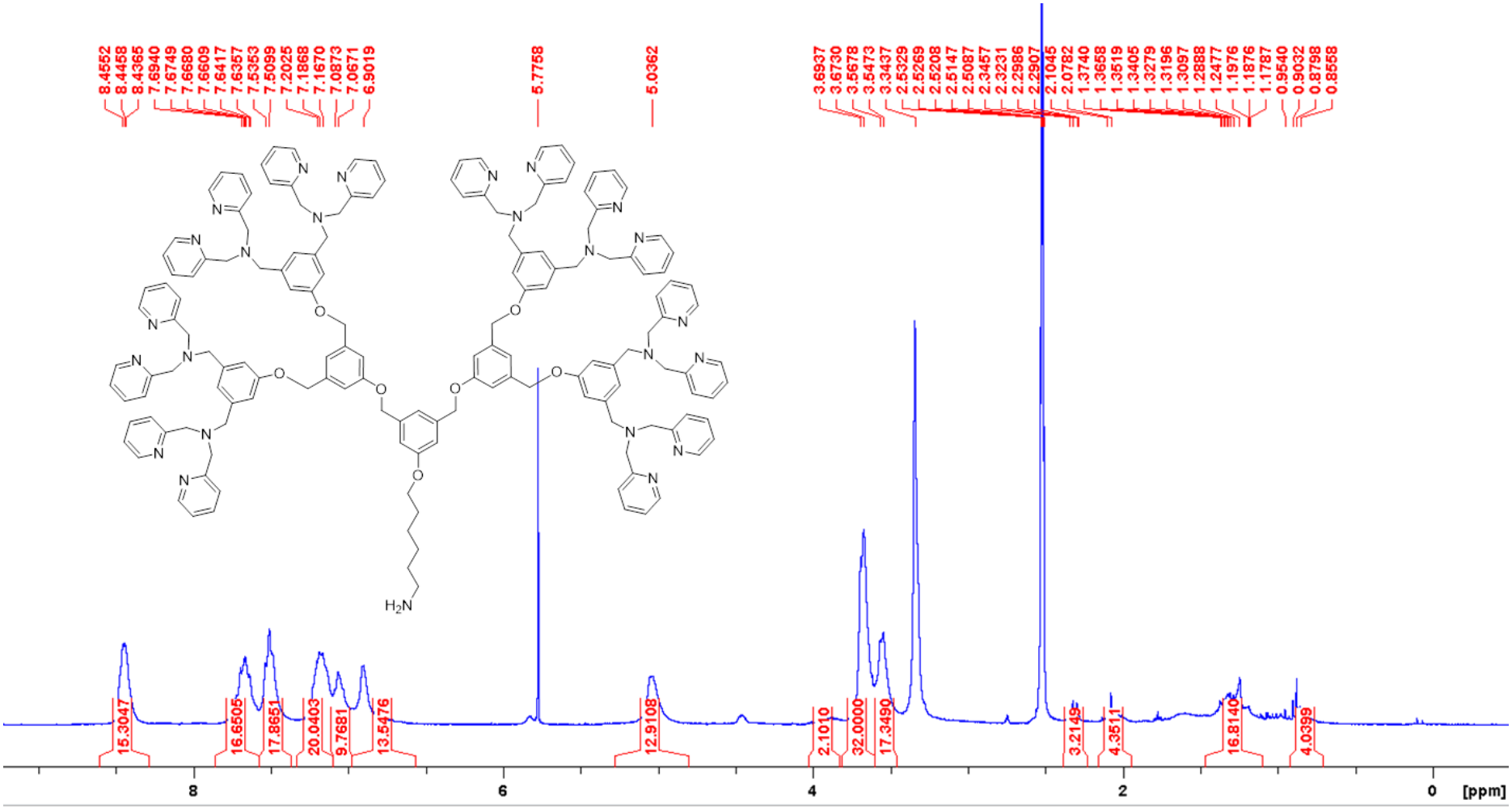

Figure S42. ^{1}H NMR spectrum of Ligand 8-NH_2, Related to Scheme 2.

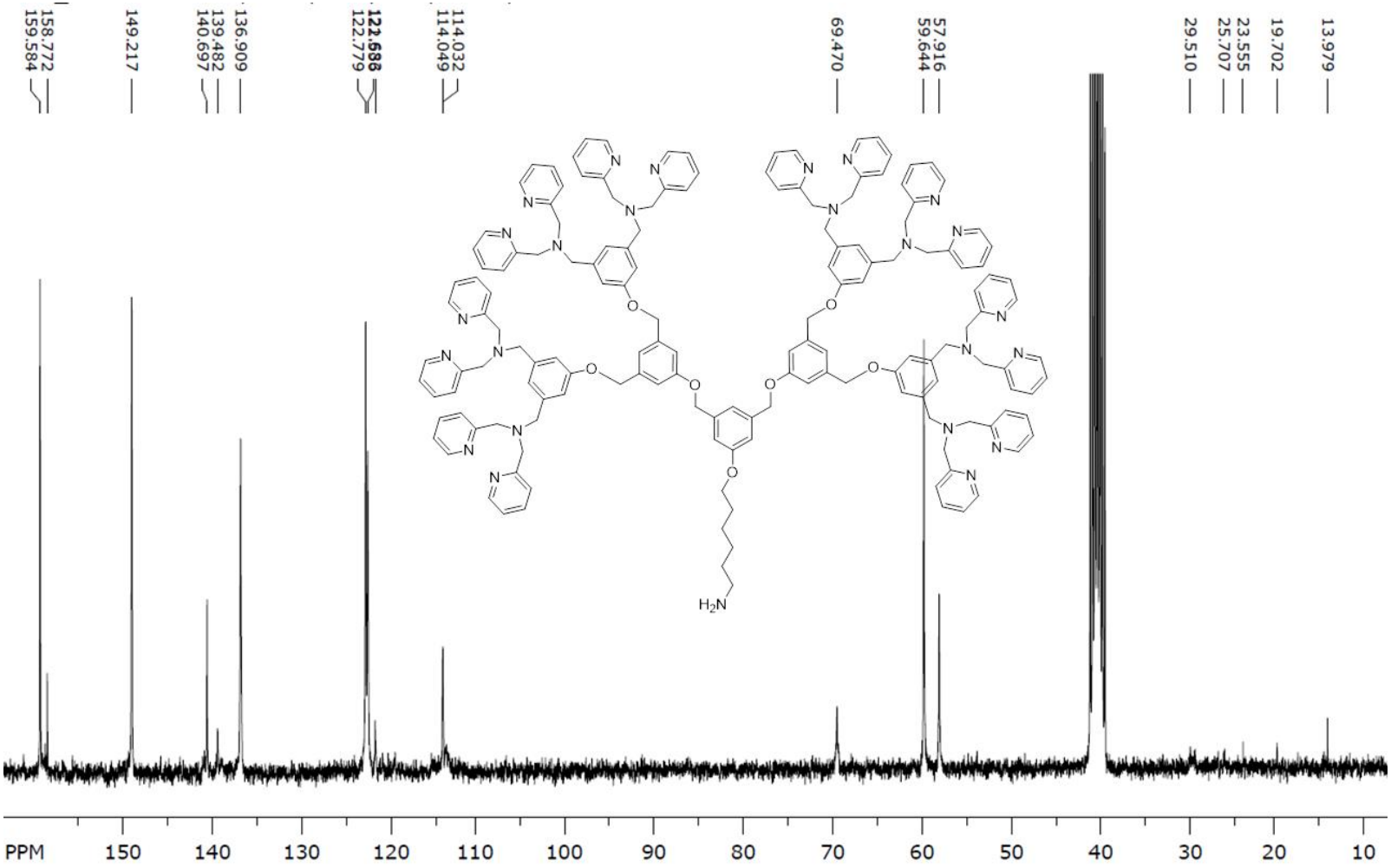

Figure S43. ^{13}C NMR spectrum of Ligand 8-NH_2, Related to Scheme 2.

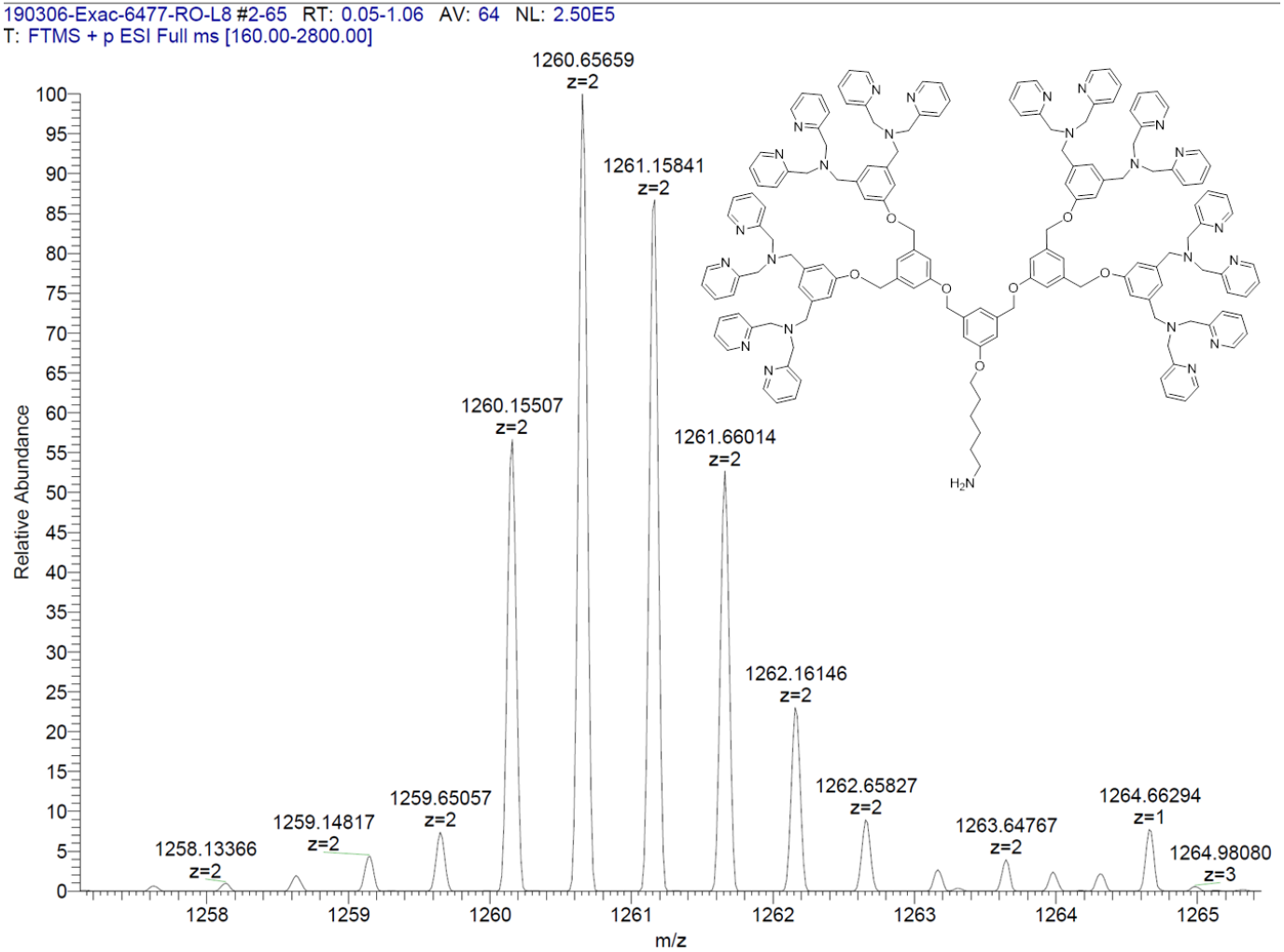

Figure S44. ESI-MS spectrum of Ligand 8- NH_2, Related to Scheme 2.

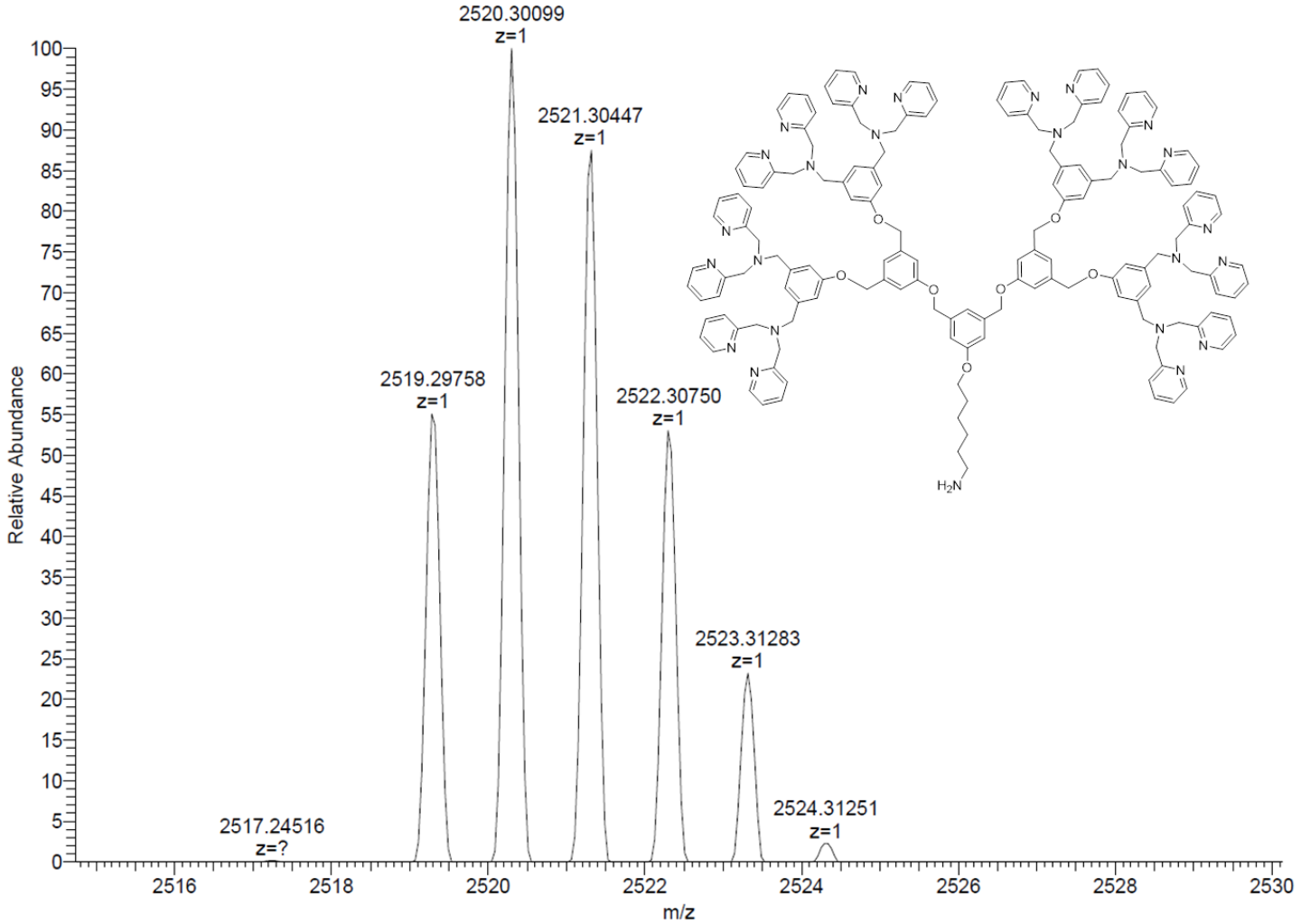

Figure S45. ESI-MS spectrum of Ligand 8- NH_2, Related to Scheme 2.

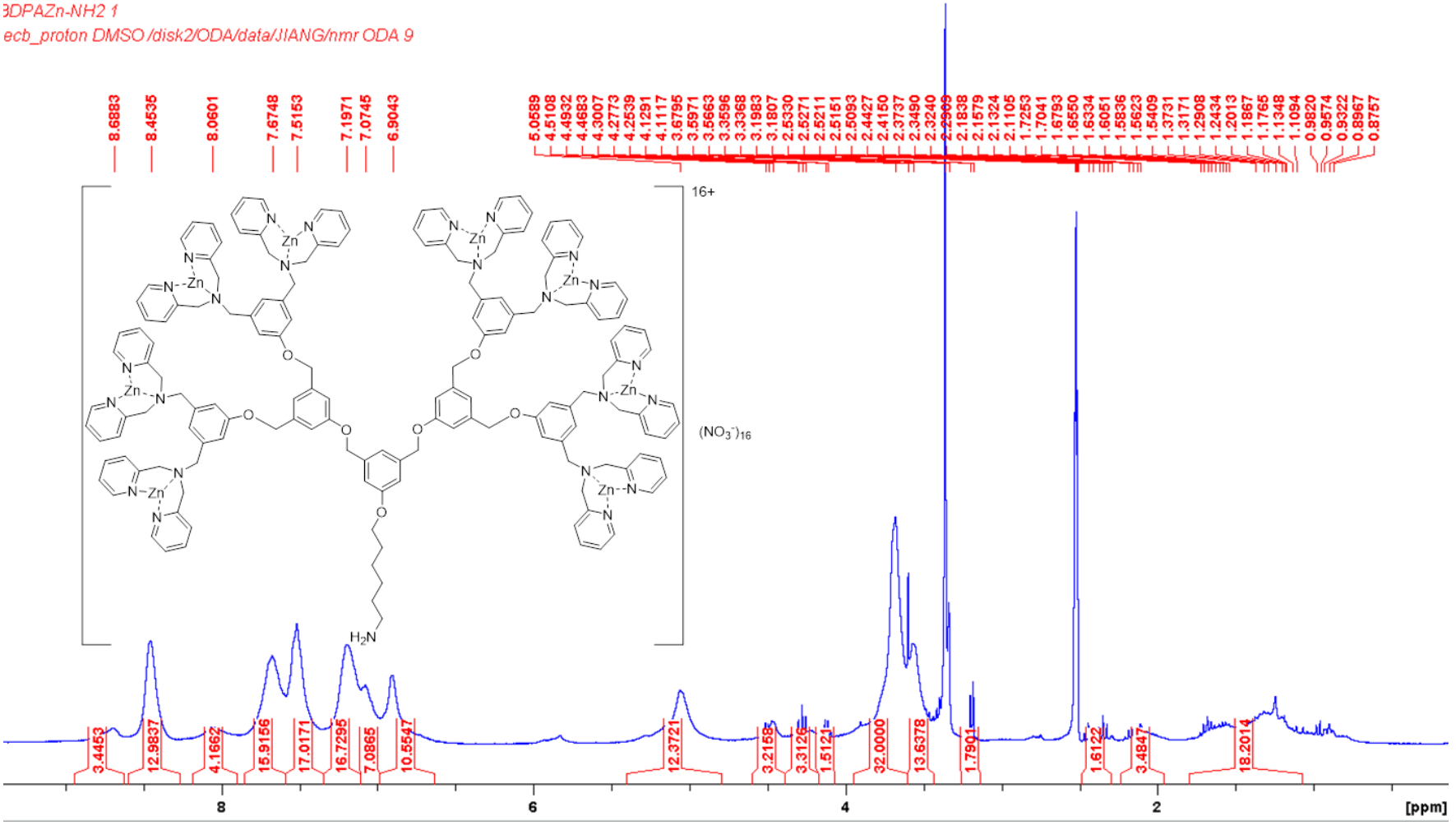

Figure S46.C8, ^{1}H NMR spectrum of Related to Scheme 2.

References:

Xiang, Y., Moulin, E., Buhler, E., Maaloum, M., Fuks, G., and Giuseppone, N. (2015). Hydrogen-Bonded Multifunctional Supramolecular Copolymers in Water. Langmuir. *31*, 7738-7748.

Segretti, M. C., Vallerini, G. P., Brochier, C., Langley, B., Wang, L., Hancock, W. W., and Kozikowski, A. P. (2015). Thiol-Based Potent and Selective HDAC6 Inhibitors Promote Tubulin Acetylation and T-Regulatory Cell Suppressive Function. ACS Med Chem Lett. *6*, 1156-1161.

Johansson, A., Abrahamsson, M., Magnuson, A., Huang, P., Martensson, J., Styring, S., Hammarstrom, L., Sun, L., and Akermark, B. (2003). Synthesis and photophysics of one mononuclear Mn(III) and one dinuclear Mn(III,III) complex covalently linked to a ruthenium(II) tris(bipyridyl) complex. Inorg Chem. *42*, 7502-7511.

Turkyilmaz, S., Rice, D. R., Palumbo, R., and Smith, B. D. (2014). Selective recognition of anionic cell membranes using targeted liposomes coated with zinc(ii)-bis(dipicolylamine) affinity units. Org Biomol Chem. *12*, 5645-5655.

Jain, A. K., Reddy, V. V., Paul, A., K, M., and Bhattacharya, S. (2009). Synthesis and evaluation of a novel class of G-quadruplex-stabilizing small molecules based on the 1,3-phenylene-bis(piperazinyl benzimidazole) system. Biochemistry. *48*, 10693-10704.